Analyzing the Impact of Dynamic Cornering Motion on Race Car Aerodynamics

ME55035: ME-EFPT Msc Thesis

Hrishikheshan Ghiridharan

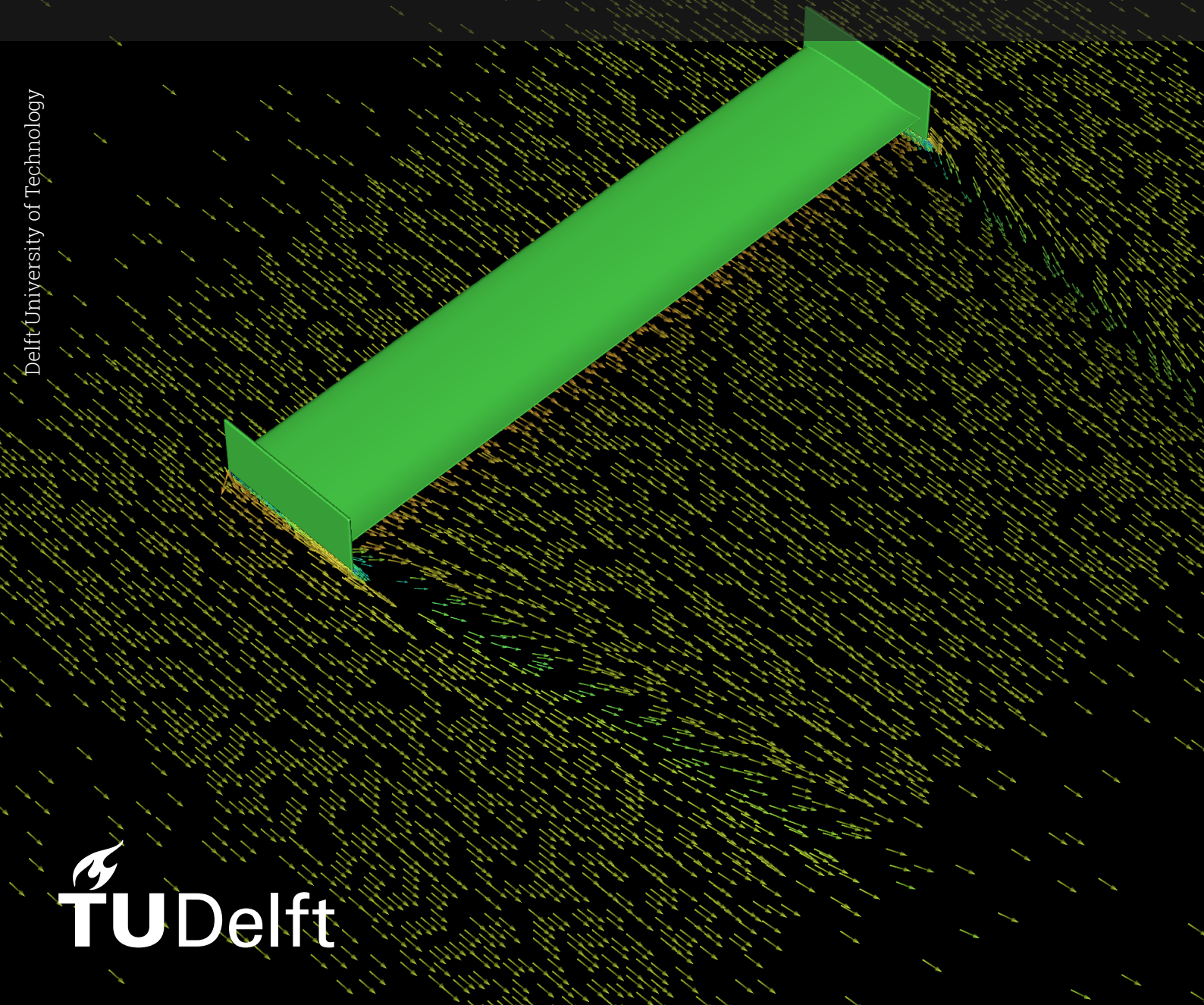

Delft University of Technology

TU Delft

Analyzing the Impact of Dynamic Cornering Motion on Race Car Aerodynamics

by

Hrishikheshan Ghiridharan
Student Number: 5919452

in partial fulfillment of the requirements of the degree
Master of Science
in Mechanical Engineering
at the Department of Process and Energy
of the Mechanical Engineering Faculty of Delft University of Technology.
To be defended publicly on Monday, August 25, 2025 at 2:00 PM

Supervisor:	Dr.ir. M.J.B.M Pourquie
Thesis Committee:	Dr.ir. W.J. Baars BSc
Co - Supervisor's:	Ing. Edwin Overmars & Ir. Shanwei Zhou
Faculty:	Faculty of Mechanical Engineering, TU Delft

TU Delft

Acknowledgements

This thesis marks the conclusion of my graduation project for the Master's program in Mechanical Engineering, specializing in Energy Flow and Process Technology, at Delft University of Technology. It represents the completion of an extensive analysis on the front wing of a Formula 1 car under dynamic cornering conditions. This achievement was not possible without the unwavering support of many people who stood by me through the highs and lows of this journey.

First and foremost, I would like to express my sincere gratitude to my supervisor, Dr. M.K.B.M. Pourquie, for his invaluable guidance and support throughout the project. His expertise in CFD simulations was instrumental in shaping my research and enabling me to achieve my intended goals.

I am deeply thankful to Ing. Edwin Overmars and Ir. Shanwei Zhou for their insights into the aerodynamics of Formula 1 cars and for guiding me in setting up simulations. Their input not only strengthened my understanding but also provided methods that can be applied in future experimental research to compare CFD results with physical data.I would also like to express my appreciation to Dr.ir. W.J. Baars for kindly joining my graduation committee and contributing his expertise to my evaluation process.

My heartfelt thanks go to my family and friends for their unwavering support. I am forever indebted to my parents for their care, belief in me, and encouragement throughout my academic journey. My brother has been one of my greatest mentors, guiding me in the right direction since childhood. I am equally thankful to my friends, both here in the Netherlands and back in India for always being there when I needed them.

Finally, I am grateful to Delft University of Technology. Over the past two years, I have navigated challenges and setbacks that have shaped me into a more resilient individual and a better engineer. I also wish to thank all the mentors and friends who made this journey meaningful and rewarding.

Hrishikheshan Ghiridharan

Delft, August 2025

Abstract

A Formula 1 car experiences dynamic aerodynamic conditions throughout a race, particularly during phases of acceleration, deceleration, and cornering. With the reintroduction of ground effect by Fédération Internationale de l'Automobile, FIA regulations in 2022, the aerodynamic sensitivity of the underfloor and front wing regions has become increasingly important. However, transient effects under such dynamic conditions are difficult to replicate in traditional wind tunnels or steady Computational Fluid Dynamics, CFD environments. This study numerically investigates the transient aerodynamic behavior of a front wing operating under ground effect, using a scaled model of the Tyrrell 026 Formula 1 front wing.

The research focuses on capturing transient aerodynamic behavior during straight-line motion, normal cornering, and yawed cornering configurations under both accelerating and decelerating conditions. 3D Reynolds Averaged Navier–Stokes (RANS) simulations using the SST k–ω turbulence model are conducted in ANSYS Fluent. Detailed comparisons are made between steady state and unsteady results to understand how added mass effects, vortex shedding, and asymmetrical flow patterns influence force and moment coefficients.

Results show significant deviation in aerodynamic forces and moments during transient phases, particularly under cornering with yaw, where asymmetries in flow around the left and right endplates amplify aerodynamic imbalance. The study quantifies these effects using non-dimensional analysis and time-resolved post-processing, revealing critical dependencies between transient flow structures and aerodynamic response. These insights provide a foundation for improving the simulation fidelity of dynamic flow conditions and optimizing front wing setup for real-world race conditions.

Keywords: Ground Effect, Transient Aerodynamics, Computational Fluid Dynamics, Turbulence Modeling, Added Mass, Vortex Shedding, T026 Front Wing

Contents

List of Figures

List of Tables

Nomenclature

Abbreviations

Abbreviation	Definition
2D	Two Dimensional
3D	Three Dimensional
acc.	Acceleration
ALE	Arbitrary Lagrangian Eulerian
AOI	Angle of Incidence
B.L.	Boundary Layer
BW	Bottom Wall
CFD	Computational Fluid Dynamics
CFL	Courant Friedrichs Lewy
dec.	Deceleration
DNS	Direct Numerical Simulation
F1	Formula 1
FIA	Fédération Internationale de l'Automobile
FVM	Finite Volume Method
GPS	Global Positioning System
I	Inlet
ins	Instantaneous
LE	Leading Edge
LEIS	Left Endplate Inner Surface
LEOS	Left Endplate Outer Surface
LEP	Left EndPlate
LES	Large Eddy Simulation
mag	Magnitude
MRF	Moving Reference Frame
NS	Navier Stokes Equation
O	Outlet
NPL	National Physics Laboratory
PIV	Particle Image Velocimetry
RANS	Reynolds Averaged Navier Stokes
REIS	Right Endplate Inner Surface
REOS	Right Endplate Outer Surface
REP	Right EndPlate
SG Filter	Savitzky-Golay Filter
SST	Shear Stress Transport
std	Steady State
T026	Tyrrell 026
TE	Trailing Edge
TW	Top Wall

Symbols

Symbol	Definition	Unit
a	Acceleration / Deceleration	[m/s^2]
$\vec{a_c}$	Centripetal Accleration	[m/s^2]
$\vec{a_{cor}}$	Corolis Acceleration	[m/s^2]
A	Reference Area	[m^2]
c	Chord Length	[m]
c_s	Speed of Sound	[m/s]
C^*	Aerodynamic Center of the Airfoil	
C_D	Coefficient of Drag Force	[-]
C_f	Skin Friction Coefficient	[-]
C_F	Coefficient of Force	[-]
C_L	Coefficient of Lift Force	[-]
C_M	Coefficient of Moment	[-]
C_P	Coefficient of Pressure	[-]
C_S	Coefficient of Side Force	[-]
F	Force	[N]
F_D	Drag Force	[N]
F_L	Lift Force	[N]
F_S	Side Force	[N]
g	Acceleration due to Gravity	[m/s^2]
h	Ground Clearance	[m]
M	Moment	[Nm]
M_ϕ	Rolling Moment	[Nm]
M_ψ	Yawing Moment	[Nm]
M_θ	Pitching Moment	[Nm]
p	Pressure	[Pa]
R	Radius	[m]
s	Span Length of the airfoil	[m]
t	Flow time / Simulation time	[s]
t^*	Normalized flow time	[s]
t_{start}, t_{end}	time at start deceleration and time at end of acceleration	[s]
T_w	Wall Shear Stress	[Pa]
TVR	Turbulent Viscosity Ration	[-]
u, V	Velocity	[m/s]
u_τ	Frictional Velocity	[m/s]
ω	Angular Velocity	[rad/s]
$V(t)$	Instantaneous Velocity	[m/s]
y^+	Non Dimensional wall distance	[-]
α	Angular Accleration	[rad/s^2]
ω	Specific Dissipation Rate	[-]
ρ	Density	[kg/m^3]
θ	Pitch Angle	[rad]
ϕ	Rolling Angle	[rad]
ψ	Yaw Angle	[rad]
μ	Dynamic Viscosity	[Pa s]
μ_t	Eddy Viscosity	[Pa s]
k	Turbulence Kinetic Energy	[m^2/s^2]
ω	Specific Rate of Dissipation	[s^{-1}]
Re	Reynolds Number	[-]
St	Strouhal Number	[-]
Co	Courant Number	[-]
Ma	Mach Number	[-]

Symbol	Definition	Unit
$_{i,j,k}$	Mutually perpendicular cartesian directions	
$\vec{}$	Vector	
$'$	Pertubration	
$\bar{}$	Averaged Value	
$_{\infty}$	Far Field Region	
$_{am}$	Added Mass	

1

Introduction

Aerodynamics is a fundamental physical phenomenon that has been studied and developed extensively since the 17th century. Its principles are applied across various fields, including automotive engineering, aviation, aerospace, energy production, architecture, and even athletics.

In the context of automotive aerodynamics, it plays a crucial role in optimizing vehicle performance. While reducing aerodynamic drag is essential for enhancing fuel efficiency, the discipline extends beyond mere drag minimization. A critical aspect of vehicle aerodynamics, particularly in motorsports, is achieving an optimal balance between downforce and lift. This balance is paramount in racing, where maintaining high cornering speeds while ensuring stability on straights is essential for minimizing lap times. An optimized aerodynamic configuration enables a race car to generate sufficient downforce for improved traction through corners while minimizing drag to achieve competitive straight-line speeds.

1.1. Formula 1

Coming to racing, Formula 1 is a sport where success hinges on achieving the fastest car on the grid. A team's path to victory begins with securing the best possible qualifying position and extends to optimizing performance throughout the race. While various factors influence race outcomes, a car's on-track performance remains a critical determinant of success.

Over the years, the performance gap between teams has narrowed, leading to increasingly competitive races. The 2024 season exemplified this trend, featuring seven different race winners and a championship battle that extended to the final race of the season. Additionally, several lower ranked teams significantly improved their performances, earning valuable points [Francis, 2024]. This intensifying competition highlights the evolving dynamics of the sport, where advancements in car design, aerodynamics, and strategy play pivotal roles in determining race outcomes.

In a Formula 1 car, numerous factors contribute to its performance and lap times, with aerodynamics playing a pivotal role. Studies have shown that aerodynamic improvements can reduce lap times by up to 1%, a seemingly small but critical margin in competitive racing. For instance, during the 2024 Canadian Grand Prix qualifying session, the pole position (P1) and second position (P2) drivers recorded identical lap times [Formula 1, 2024a; Toet, 2013]. This underscores the importance of even minor aerodynamic enhancements in a sport where every millisecond counts. Consequently, our focus will be on understanding the aerodynamic effects in Formula 1.

The aerodynamic performance of a Formula 1 car is influenced by various components, including the front wing, rear wing, floor and diffuser, bodywork, wheels, suspension, and more. Among these, the front wing, rear wing, floor, and diffuser are particularly significant, as they contribute most to overall downforce and drag. Notably, the front wing alone accounts for approximately 28% of the total down force and 20% of the drag force [Shaalan et al., 2024]. This highlights its critical role in the car's performance. Additionally, the front wing is the first component to interact with the oncoming airflow, influencing the downstream aerodynamics of the entire vehicle. This study focuses on the front wing due to its impact and the lack of upstream body interference in the flow.

In modern Formula 1 cars, at a speed of 150 km/h, the generated downforce is approximately equal to the car's own weight. At maximum speed, however, the downforce can reach three to four times the car's weight, significantly influencing overall performance [Mercedes-AMG Petronas Formula One Team, 2021].

Downforce is a critical factor in vehicle performance, as it increases the car's grip by pushing it toward the ground. Higher downforce allows a car to navigate corners at greater speeds, improving handling and reducing lap times. However, simply maximizing downforce is not an optimal solution, as it also increases aerodynamic drag, which reduces top speed on straights.

1.2. Research Motivation

Formula 1 aerodynamics has long been a cornerstone of performance engineering, driving innovations that push the boundaries of vehicle speed and stability. In the pursuit of competitive advantage, teams have historically invested heavily in aerodynamic development. However, the introduction of the budget cap regulation by the Fédération Internationale de l'Automobile (FIA) in 2021 has imposed significant financial constraints on all teams. This regulatory change was designed to level the playing field, with leading teams such as Mercedes reportedly reducing their budgets from approximately 450 million Euros in 2020 to 145 million Euros in 2021 [Kumar, 2022].

Within this constrained financial environment, it has become critical for teams to identify and develop only the most effective aerodynamic components. Failed developments now carry a heavier cost, both in terms of monetary loss and the opportunity cost of constrained future iterations [Barretto, 2020; Warwick, 2024]. As a result, resource allocation has become more strategic, with greater emphasis on simulation and pre-validation.

One of the persistent challenges in Formula 1 aerodynamics lies in bridging the gap between simulation, wind tunnel testing, and on-track performance. Wind tunnels, though essential, cannot perfectly replicate all real-world conditions and are further restricted by regulatory limits on usage time [McLaren Racing, 2022; Smedley, 2019; Veena - Cadence, 2025]. While computational fluid dynamics (CFD) provides a powerful alternative, its predictive accuracy depends heavily on correctly modeling complex and dynamic conditions such as yaw, ground effect, and transient flows.

A particularly underexplored area is cornering aerodynamics. Unlike straight-line conditions, cornering involves dynamic changes in flow due to steering input, acceleration, and deceleration. Wind tunnels are effective for straight-line aerodynamic testing but cannot accurately recreate the transient and three-dimensional flow structures encountered during cornering. This gap is significant given that race performance relies not only on straight-line speed but also on high-speed and low-speed cornering behavior.

The main motivation for this research arises from these challenges and focuses on the following points:

- The chosen component for analysis is the front wing, as it is a critical source of downforce and plays a dominant role in shaping the downstream aerodynamic flow structure around the car.
- From a research standpoint, the front wing is an ideal starting point since it operates in relatively clean, laminar inflow conditions, enabling a more controlled and interpretable analysis.
- This study specifically investigates flow behavior during cornering maneuvers, particularly during acceleration and deceleration phases.
  - There exists a notable lack of understanding regarding the unsteady aerodynamic forces acting on the front wing during such transient cornering conditions.
  - Conversely, straight-line aerodynamic behavior has been well studied both experimentally and computationally, providing a solid foundation upon which this cornering-focused investigation can be built.

1.3. Research Objectives

The primary objective of this research is to investigate the aerodynamic differences between straight-line and cornering flows for a Tyrrell 026 front wing operating under ground effect conditions. The study begins with understanding the baseline flow behavior under steady straight-line conditions and then progressively introduces cornering dynamics. The focus is subsequently extended to examine the effects of acceleration and deceleration on the front wing during both straight-line and cornering scenarios, across varying acceleration magnitudes.

To achieve this, CFD simulations are carried out using *Ansys Fluent*. Initially, 2D simulations are conducted to develop an effective mesh strategy and assess resolution requirements. The insights gained from this step are used to construct and validate a 3D simulation framework. The full analysis, including transient dynamics such as acceleration and deceleration during cornering, is performed using three-dimensional RANS-based simulations.

The results enable a comparison between steady-state and unsteady (accelerating or decelerating) flow conditions, allowing for a deeper understanding of the physical mechanisms responsible for these differences. This includes an analysis of the added mass effect to explain the aerodynamic force variations during transient conditions.

Additionally, the study investigates vortex generation and dissipation processes in the wake of the front wing. Special attention is given to understanding how acceleration influences flow topology, and to quantifying vortex shedding behavior under different transient conditions.

This research ultimately aims to bridge the knowledge gap in unsteady cornering aerodynamics and provide insights that could contribute to improved aerodynamic design and simulation fidelity in motorsports.

1.4. Background

1.4.1. History of Airfoil in Formula 1 Cars

Aerodynamics in cars initially focused solely on bodywork until the mid-1960s when Chaparral introduced the Chaparral 2F, the first car equipped with a rear wing, which competed in the World Sportscar Championship [Wikipedia, 2025]. Inspired by this innovation, the Lotus team added similar wings to their Lotus 49 Formula 1 car in 1968, resulting in improved performance [Bonhams, 2024].

As aerodynamic research and development progressed, front wings evolved from simple single-element airfoils to more complex multi-element designs. These advancements allowed front wings to become more effective in meeting the specific aerodynamic requirements of the car and the respective track. For example, Figure 1.1 compares the front wing of a 1970 Formula 1 car to that of a 2024 Formula 1 car, illustrating how the design has adapted and become more sophisticated over time.

(a) **(b)**

Figure 1.1: Development of Front Wings in Formula 1, F1 (a) Ferrari 312B (1970) - One of the earliest F1 cars to feature a front wing [Autodromo, 2024] (b) Ferrari SF-24 (2024) - A modern example showcasing the latest advancements in front wing design [Noble, 2023]

1.4.2. Current Generation of F1 cars

The current era of Formula 1 follows a ground-effect-dominated aerodynamic philosophy, reintroduced after being deemed unsafe in 1982 [Formula 1, 2024c]. The return of ground effect aimed to create more balanced and competitive racing, ensuring that multiple teams have a chance to win races and compete for the championship, rather than dominance by just one or two teams.

Ground effect works by increasing airflow velocity beneath the inverted airfoil, generating a low-pressure zone, as illustrated in Figure 1.2. This aerodynamic phenomenon helps increase grip by pulling the car closer to the ground, enhancing cornering performance and making overtaking easier.

Additionally, the reintroduction of ground effect has simplified the car's wings and reduced complex aerodynamic elements, minimizing turbulent airflow. This has particularly benefited cars following closely behind others, as reduced turbulence results in less stability loss and lower engine and tire overheating [GroundEffect, 2024]. Given the dominance of ground effect, understanding the aerodynamics of the front wing has become more crucial than ever, as it plays a significant role in managing airflow around the car.

1.4.3. Aerodynamics of Front Wings

The front wing of a Formula 1 car incorporates an inverted airfoil profile designed to generate downforce, in contrast to conventional airfoils used in aviation that produce lift [Aultman, 2017]. This is achieved by creating a region of higher pressure above the wing and lower pressure beneath it, thereby forcing the car downward and enhancing grip and stability during high-speed maneuvers. Figure 1.2 shows the Tyrell 026 front wing and its airfoil geometry, which is employed in this study. The low-pressure region beneath the airfoil is the principal contributor to downforce generation. Given its significant role in influencing vehicle dynamics, particularly during cornering and braking, the front wing is a critical component in optimizing lap times and overall aerodynamic performance.

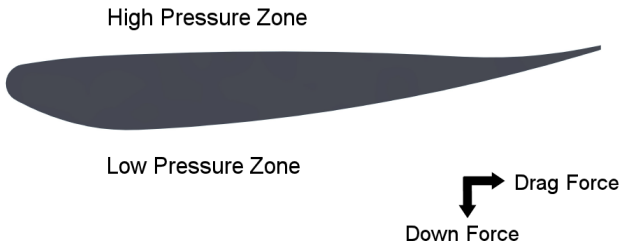

Figure 1.2: 2D front wing profile of the Tyrrell 026 Formula 1 car, illustrating the high-pressure and low-pressure regions, along with the directions of the resultant drag force and downforce

In general, air flows from high-pressure to low-pressure regions. In the case of an airfoil, the least resistance occurs at the airfoil tips along the spanwise direction. This results in spillage around the tips, forming a vortex, which is essentially a rotating mass of air, as illustrated in Figure 1.3a. For an inverted airfoil with an endplate at its tip, two distinct vortices are generated: the primary and secondary vortices. The primary vortex forms on the suction side due to the pressure difference between both sides of the airfoil. Meanwhile, the secondary vortex originates on the pressure side as a result of increased pressure acting on the endplate, as depicted in Figure 1.3b.

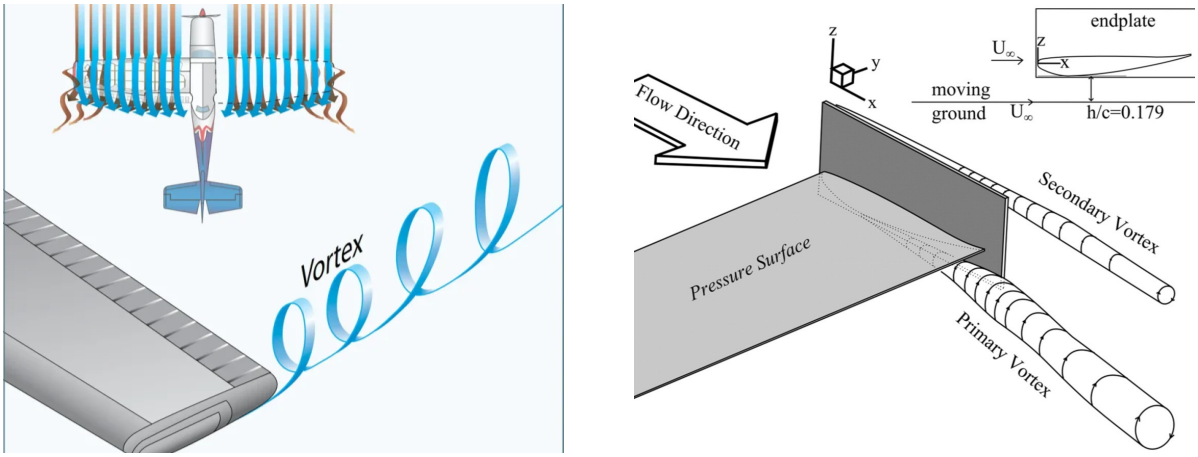

(a) **(b)**

Figure 1.3: Tip vortices from an airfoil/wing (a) Vorticity generated by a conventional aircraft wing [Flight Study, 2024] (b) Formation of primary and secondary vortices from an inverted airfoil (T026) with an endplate in a straight-line flow [Keogh, Doig, et al., 2015]

1.5. Previous Investigations on wings in ground effect

Extensive investigations have been conducted on wings operating in ground effect. Detailed results are presented in Appendix B, with the most significant and relevant findings summarized below.

In the ground effect era of Formula 1, as discussed in subsection 1.4.2, understanding the relationship between C_D (coefficient of drag) and C_L (coefficient of lift) with respect to ground height is crucial for optimizing performance. Katz, 2006 performed analysis on the LS(1) - 0413 airfoil, and observed that as the height between the airfoil and the ground (h) increases, the C_D continues to decrease. In contrast, the C_L initially increases before decreasing, as shown in Figure 1.4. This indicates that while drag forces decrease as the airfoil moves further from the ground, lift forces increase and then decrease. This correlation is critical in optimizing performance for the new generation of F1 cars.

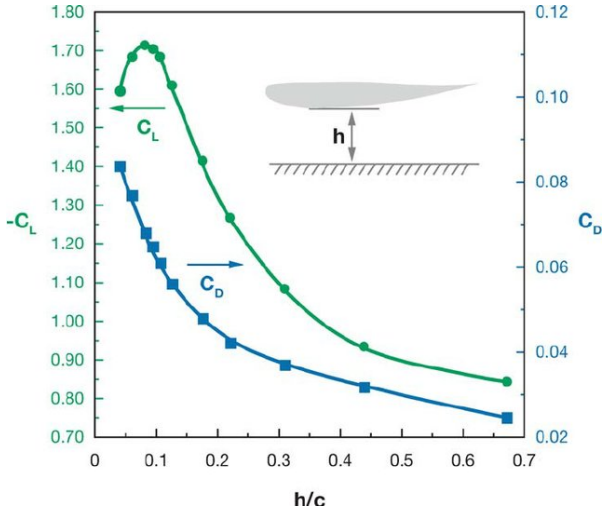

Figure 1.4: Coefficients of Drag and Lift force versus Ground Clearance, h for an Inverted LS(1) - 0413 Airfoil [Katz, 2006]

Accelerating flows are an important aspect, as the car experiences high acceleration and deceleration. Pathanadka, 2022 performed a study on the T026 airfoil was performed with nonlinear acceleration profiles to analyze the drag and lift forces, along with the instantaneous drag and lift coefficients ($C_D - ins$ and $C_L - ins$) where ρ is the density of the fluid, $V(t)$ is the instantaneous velocity and A is the area of the airfoil:

$$C_{D\_ins} = \frac{2F_D}{\rho V(t)^2 A} \tag{1.1}$$

$$C_{L\_ins} = \frac{2F_L}{\rho V(t)^2 A} \tag{1.2}$$

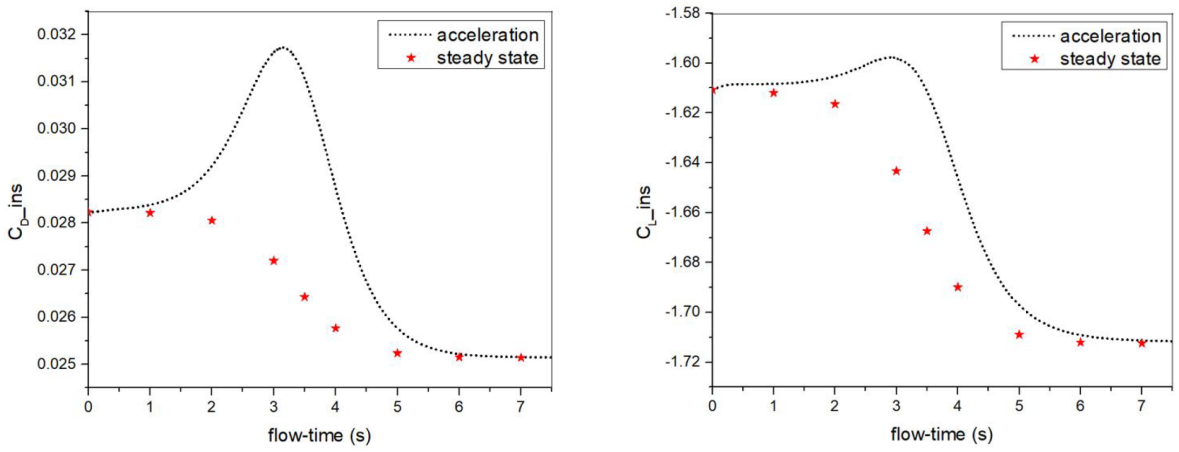

Figure 1.5: Instantaneous aerodynamic force coefficients under a non-linear acceleration profile compared to steady-state values: (a) Instantaneous coefficients of drag, $C_D - ins$ (b) Instantaneous coefficients of lift, $C_L - ins$ [Pathanadka, 2022]

The drag and lift forces were analyzed for a non-linear acceleration profile featuring a 5-second acceleration phase within a total duration of 7.5 seconds. As shown in Figure 1.5, both the instantaneous drag coefficient, $C_D - ins$, and the lift coefficient, $C_L - ins$, deviate noticeably from their steady-state values during this phase. These deviations highlight the influence of transient flow effects, which are particularly pronounced in the drag direction.

One of the primary contributors to this behavior is the added mass effect, which arises due to the inertia of the surrounding fluid as it is accelerated by the moving body. This phenomenon leads to elevated unsteady aerodynamic forces that differ from those predicted under steady-state assumptions. As discussed in prior studies Pathanadka, 2022; Reijtenbagh et al., 2022, the added mass effect is especially significant during acceleration and deceleration, making it a critical consideration in understanding real-world aerodynamic performance.

Experimental studies have also been conducted by Grift et al., 2019 on accelerating flows on a T026 profile, employing the experimental setup described in subsubsection A.1.1.2, similar to the previously discussed simulations. As shown in Figure 1.6, a momentary peak in the forces was observed, consistent with findings from computational studies discussed earlier. This phenomenon arises due to the addition of virtual mass.

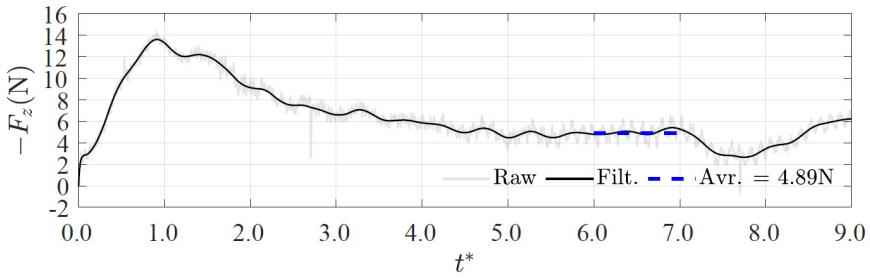

Figure 1.6: Downforce generated by the airfoil during an acceleration phase from 0 to 0.4 seconds, followed by maintaining the final velocity reached at the end of acceleration [Zhou, 2023]

Keogh et al., 2014 analyzed an airfoil under four different cases (Figure 1.7) and observed that the coefficients of lift and drag remained relatively unchanged. However, with the introduction of yaw, a noticeable coefficient of side force emerged. During cornering, the yawing moment coefficient ($C_{M\psi}$) and rolling moment coefficient ($C_{M\phi}$) were found to be negative, whereas the addition of yaw caused both $C_{M\psi}$ and $C_{M\phi}$ to become positive, indicating adverse effects. Meanwhile, the pitching moment coefficient ($C_{M\theta}$) remained consistent across all flow conditions.

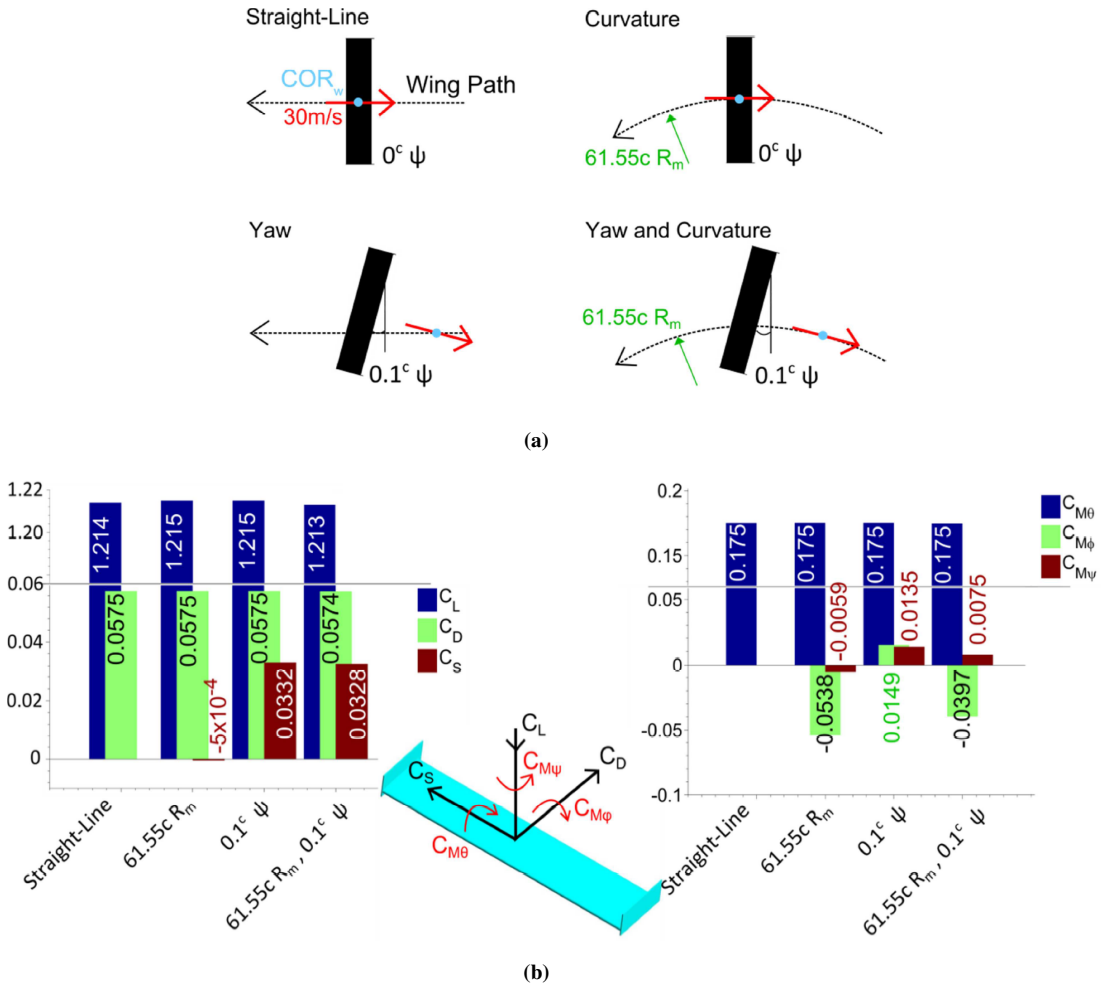

Figure 1.7: (a) Illustration of the four different types of tests performed on the wing: Straight-Line, Curvature, Yaw, and Yaw with Curvature (b) Coefficients of lift, drag, and side forces, along with the coefficients of yaw, pitch, and rolling moments for the four different cases shown in Figure 1.7a [Keogh et al., 2014]

From the above results, it is evident that cornering significantly influences drag, lift, side force, and moment coefficients, with variations depending on the cornering radius and the inclusion of yaw effects. While some studies have explored these parameter changes for different geometries, their impact on airfoils remains largely unaddressed. Additionally, there is limited insight into the role of ground clearance, and the effects of cornering on flow structures, as well as the influence of acceleration and deceleration, remain largely unexplored.

2

Simulation Setup and Turbulence Modeling

2.1. Computational Domain

For this study, the front wing of the Tyrrell 026 (T026) Formula 1 car is selected due to the availability of extensive prior research on this configuration [Pathanadka, 2022; Zerihan and Zhang, 2001a; Zhou, 2023]. The investigation is conducted in two stages. First, a 2D simulation is performed to obtain preliminary insights and to guide the development of an appropriate meshing strategy for the 3D case. This is followed by a 3D simulation, which captures the aerodynamic effects during both straight-line motion and cornering scenarios.

2.1.1. 2D Computational Domain

To analyze the aerodynamic behavior of the T026 frontwing under acceleration and deceleration, a two-dimensional (2D) simulation is conducted. A 2D computational domain is created with the airfoil positioned at an angle of incidence of 3.45° and a chord length of $c = 0.2234$ m. The airfoil coordinates are sourced from Table C.1.

The domain boundaries are defined to minimize wall-induced interference with the flow around the airfoil:

- **Inlet (I):** Located $5c$ upstream of the airfoil.
- **Outlet (O):** Positioned $10c$ downstream of the airfoil.
- **Top Wall (TW):** Placed $5c$ above the airfoil.
- **Bottom Wall (BW):** Ground clearance set to $h = 0.179c$, consistent with prior research and representative of realistic ground-effect studies [Pathanadka, 2022; Zerihan and Zhang, 2001a].

This domain setup ensures sufficient space to capture the development of the wake while maintaining the influence of ground effect. The airfoil's proximity to the bottom wall allows for a focused investigation of ground proximity effects under dynamic flow conditions. The 2D domain configuration is illustrated in Figure 2.1.

Figure 2.1: 2D computational domain for the Tyrrell 026 airfoil. I: Inlet, O: Outlet, TW: Top Wall, BW: Bottom Wall. The airfoil is positioned near the ground to investigate ground-effect behavior

2.1.2. 3D Computational Domain

A rectangular (cuboidal) computational domain is employed for all 3D simulations, as illustrated in Figure 2.2a. An 80% scaled model of the Tyrrell 026 front wing is utilized, resulting in a chord length of 0.2234 m. This particular model is chosen due to its extensive use in prior aerodynamic studies and also because using a scaled down model provides significant computational advantages, such as reduced mesh size, lower memory usage, and faster simulation times [Pathanadka, 2022; Zerihan and Zhang, 2001a]. Detailed geometric specifications of both the airfoil and the endplate are provided in section C.1. The aerodynamic forces and moments acting on the wing are evaluated at the aerodynamic center, denoted as C^*, as shown in Figure 2.2b and Figure 2.2d [NASA, 2024a].

A ground clearance of $h = 0.224c$ is chosen, as it lies within the typical range of Formula 1 configurations and has been used in previous studies [Pathanadka, 2022; Zerihan and Zhang, 2001a]. The domain boundary conditions are defined as follows:

- **Main Inlet:** Located $5c$ upstream of the wing's leading edge.
- **Main Outlet:** Positioned $10c$ downstream of the trailing edge.
- **Top Boundary:** Placed $5c$ above the wing.
- **Bottom Boundary:** Ground clearance maintained at $h = 0.224c$.
- **Side Boundaries:** Located $7c$ laterally from the wing on either side.

A cuboidal domain provides the flexibility to accommodate unsteady simulations by allowing velocity and pressure variations at the inlet and outlet boundaries. This is particularly important when simulating acceleration, braking, and cornering conditions where transient effects play a critical role. A more detailed discussion on the application of boundary conditions is provided in section 2.3.

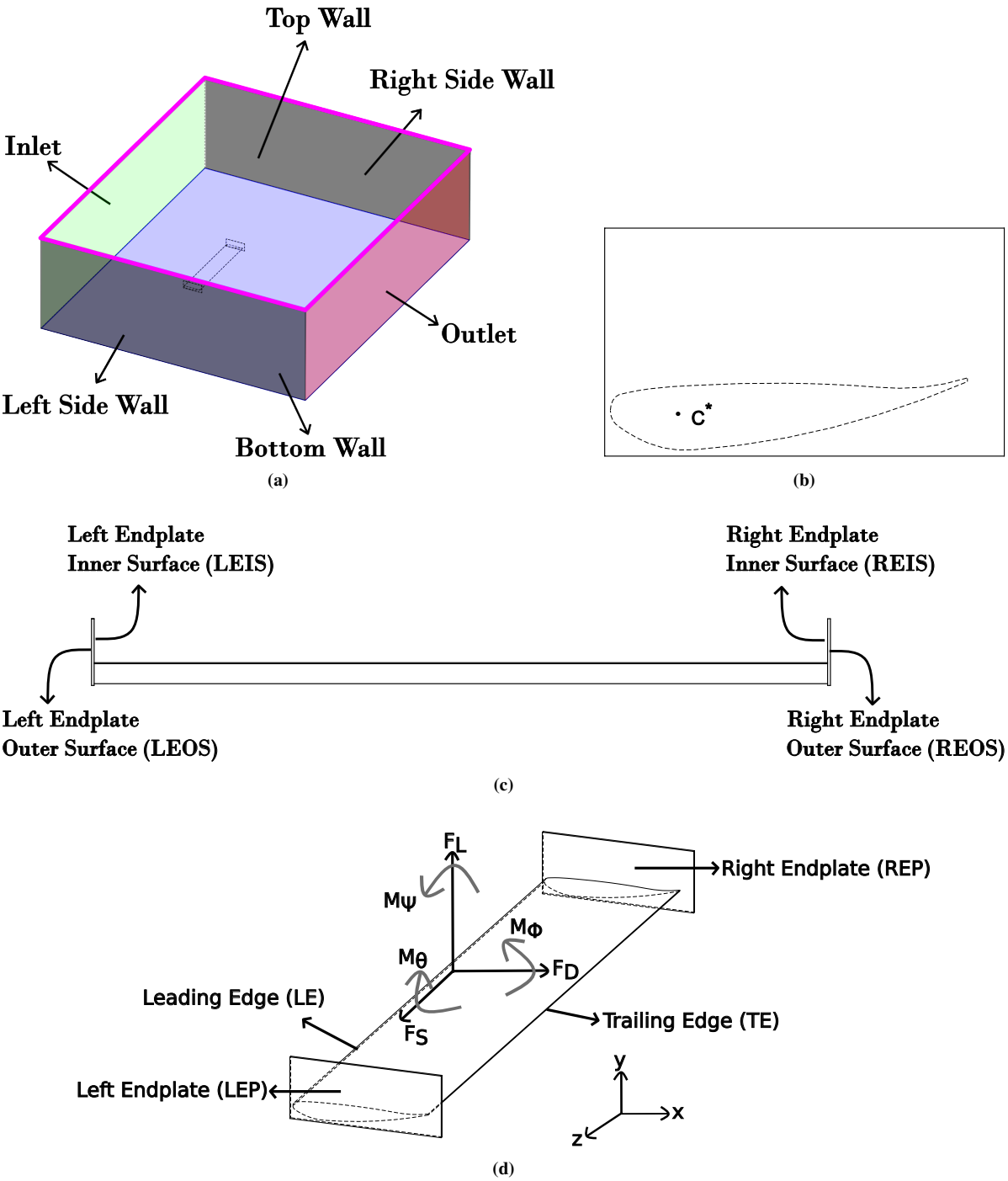

Figure 2.2: (a) Isometric view of the complete domain (b) Side view of the airfoil with endplate, showing the aerodynamic center C^* (c) View of the airfoil from the Trailing edge view of the wing showing the naming convention for the endplates (d) Isometric view of the airfoil illustrating the coordinate system for aerodynamic forces and moments, where F_D, F_L and F_S represent the drag, lift and side forces while M_ϕ, M_ψ and M_θ denote the rolling, yawing and pitching moment

2.2. Meshing

2.2.1. 2D Meshing

The 2D domain was meshed using ANSYS Mechanical Meshing tools in ANSYS 2024R1, employing face meshing to generate a high-quality, structured mesh. Edge sizing and face meshing techniques were used strategically to achieve mesh refinement near critical regions. Various edge sizings were applied to create inflation layers and to accurately capture the curvature of the airfoil. Face meshing was configured with quadrilateral cells, which helps maintain a structured grid and improves solver stability.

The final mesh consists of 215,818 nodes, with a non-dimensional wall distance, $y^+ < 1$ along the airfoil and bottom wall, ensuring adequate resolution for capturing boundary layer effects. A depiction of the mesh is shown in Figure 2.3. To maintain $y^+ < 1$ in near-wall regions, the non-dimensional wall distance was calculated using the following formulation:

$$y^+ = \frac{\rho u_\tau \Delta y_1}{\mu} \tag{2.1}$$

where ρ is the fluid density, u_τ is the friction velocity, Δy_1 is the height of the first mesh cell from the wall, and μ is the dynamic viscosity of the fluid. The friction velocity, u_τ (Equation 2.2), is computed based on the wall shear stress, τ_w (Equation 2.3), and the fluid density:

$$u_\tau = \sqrt{\frac{\tau_w}{\rho}} \tag{2.2}$$

The wall shear stress is defined by:

$$\tau_w = \mu \left(\frac{\partial u}{\partial y} \right)_{y=0} \tag{2.3}$$

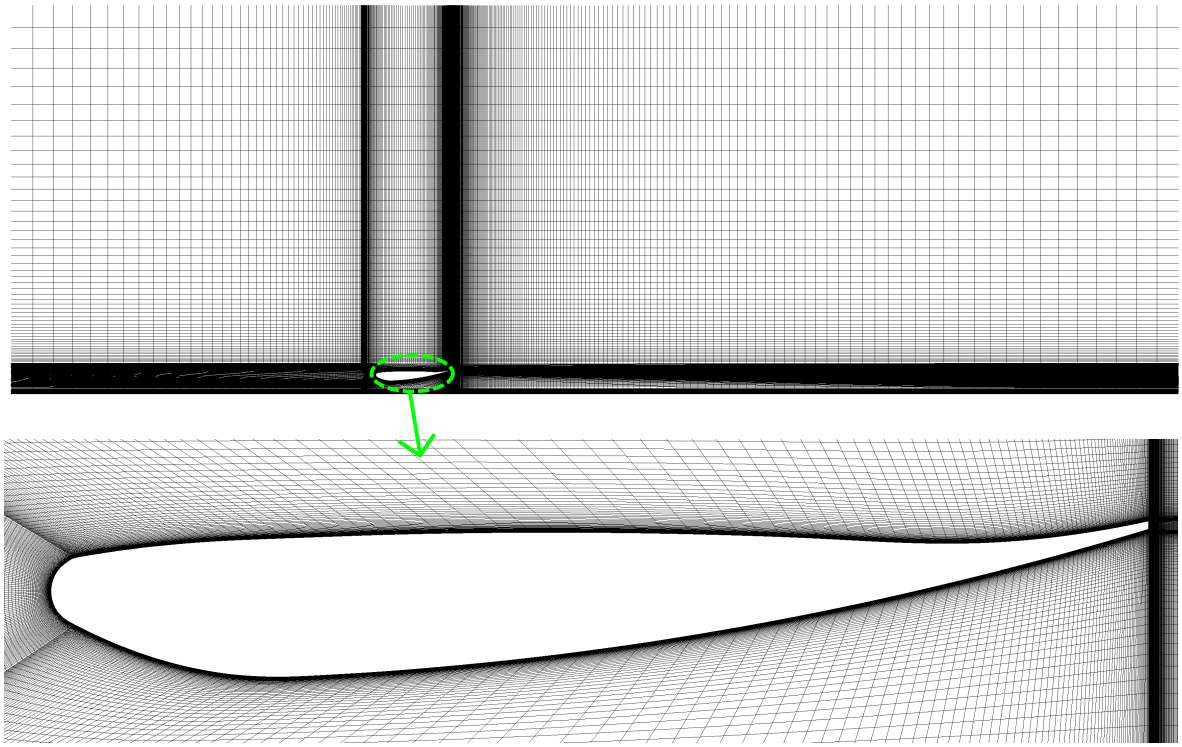

Figure 2.3: Structured Mesh for a 2D T026 Airfoil with a $h/c = 0.179$ at $\alpha = 3.45°$. The structured mesh of the entire computational domain, where the green line shows the region that is given a zoomed-in view, highlighting the mesh refinement in the vicinity of the airfoil

2.2.2. 3D Meshing

The domain was meshed using Fluent Meshing in ANSYS Fluent 2024 R2, employing multiple local refinement zones and inflation layers to ensure smooth transitions and achieve high mesh resolution near the airfoil. Initially, a fine surface refinement was applied to the airfoil geometry to accurately capture its curvature and preserve its aerodynamic fidelity.

Three box-type refinement zones were implemented using localized fine cells to capture the wake region and flow features with high accuracy. These refinement zones are highlighted by the red boundaries in Figure 2.4. Additionally, boundary layers were applied on the airfoil and bottom wall surfaces shown in blue in Figure 2.4 to ensure wall-resolved accuracy. The inflation layers were designed such that the non-dimensional wall distance, y^+ (Equation 2.1), remained below 1 along both the wing surface and the bottom wall, which are the most critical regions for turbulence resolution in wall-bounded flows.

The domain volume was filled with tetrahedral elements. Tetrahedral elements were selected due to their ability to fill complex 3D geometries efficiently and their suitability for domains with intricate features and high-curvature surfaces [Cadence CFD, 2022]. They also enhance mesh conformity in regions of complex refinement. This choice balanced computational efficiency with resolution accuracy. A summary of mesh settings is presented in Table 2.1, and the meshing strategy is visually illustrated in Figure 2.4.

Table 2.1: Detailed Mesh Settings for the 3D Computational Domain

Mesh Settings			
Surface Mesh			
	Size		
Airfoil	1 mm		
Local Refinement zone 1			
x min	0.2 m	x max	0.2 m
y min	0.2 m	y max	0.2 m
z min	0.2 m	z max	0.2 m
Mesh size	10 mm		
Local Refinement zone 2			
x min	0.5 m	x max	0.5 m
y min	0.5 m	y max	0.5 m
z min	0.3 m	z max	0.3 m
Mesh size	20 mm		
Local Refinement zone 3			
x min	3 m	x max	5 m
y min	2 m	y max	5 m
z min	0.5 m	z max	0.5 m
Mesh size	40 mm		
Boundary Layers			
Method Type	Uniform		
Number of layers	40		
First Layer Height	0.0016 mm		
Growth Rate	1.2		
Volume Mesh			
Type	Tetrahedral		
Growth Rate	1.2		
Max cell length	100 mm		
Mesh Statistics			
Number of Cells	63208107		
Number of Nodes	29891563		

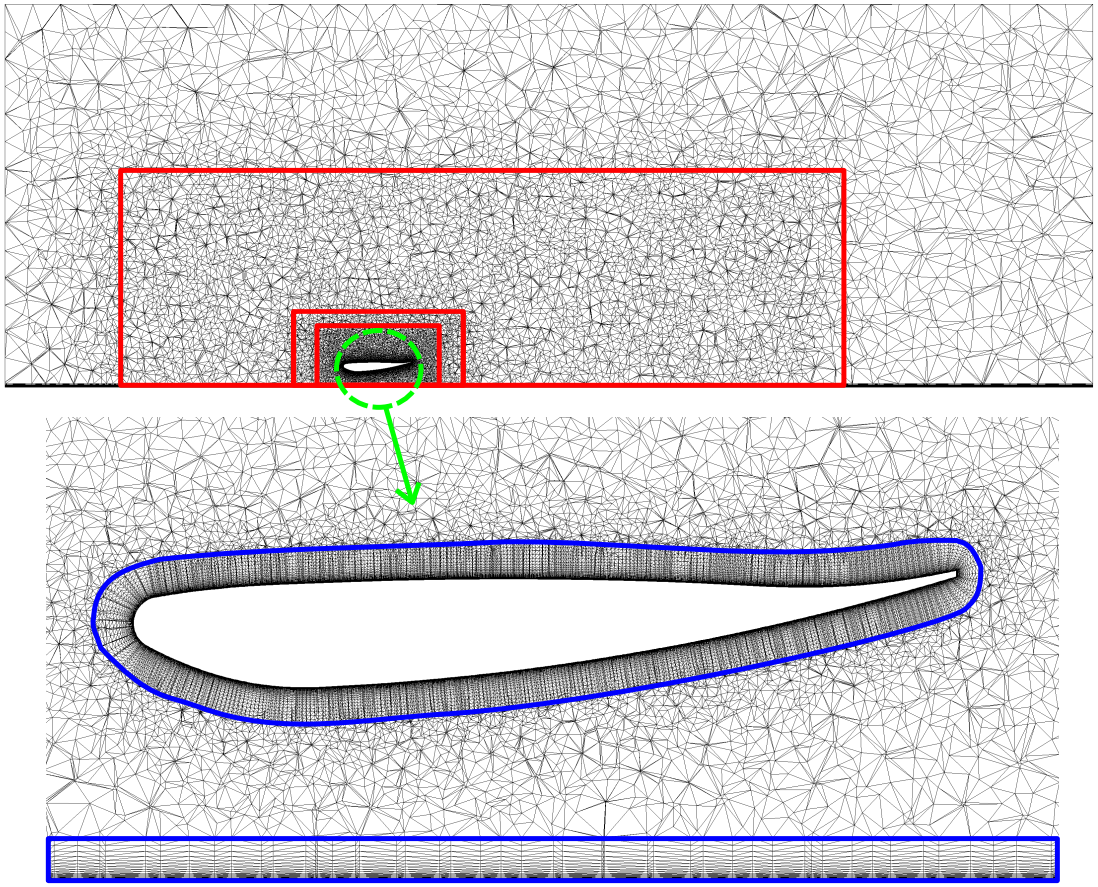

(a)

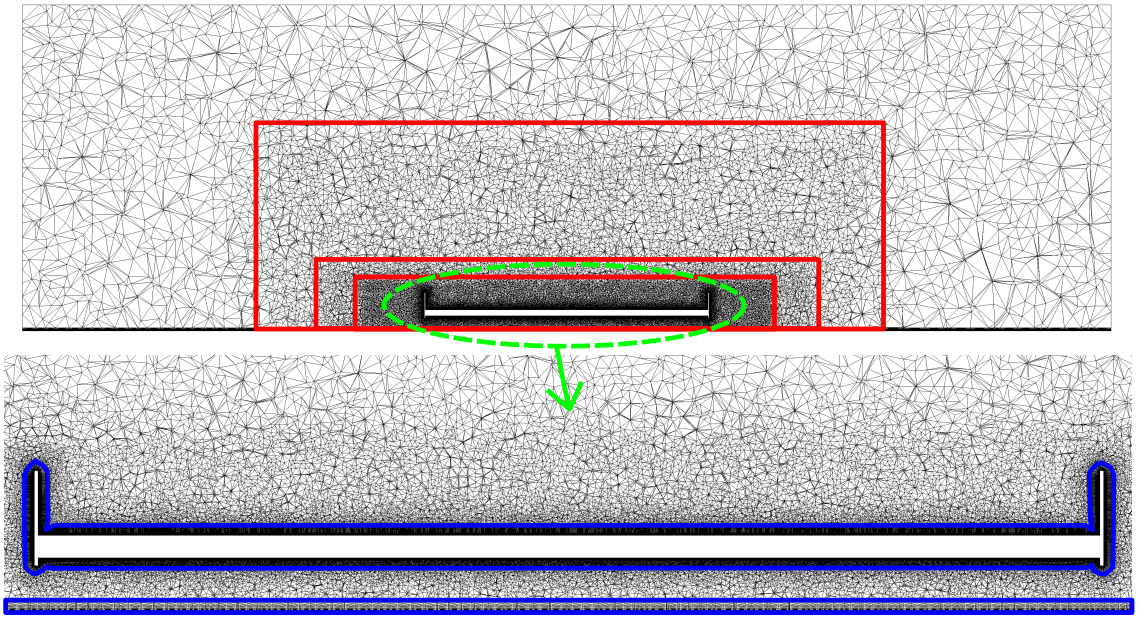

(b)

Figure 2.4: 3D Mesh shown in different 2D planes. The red lines showing the three different refinement zones used, the green line showing the region that is given a zoomed in view, while the blue lines show the boundary layers used. (a) Midplane of the side view of the front wing (b) Plane across the front wing at a distance of $0.5c$ from the leading edge

2.3. Boundary Conditions

2.3.1. 2D Simulations Boundary Conditions

The moving boundary method is employed for the simulation as it better replicates real-life scenarios. In particular, for the moving frame as discussed earlier, the momentum terms are inherently accounted for during accelerating flows. This makes it more convenient to simulate such cases. Additionally, prior studies have shown that using a moving reference frame yields more accurate results in accelerating flow regimes [Pathanadka, 2022].

For the cell zone conditions, the moving frame method is applied, where the frame velocity follows the profile shown in Figure 2.7. The inlet is set to 0 m/s in the absolute reference frame, and the outlet is maintained at 0 Pa static pressure. The bottom wall is set to 0 m/s and is treated as a no-slip moving wall relative to the moving frame. The airfoil is also assigned a velocity of 0 m/s and is modeled as a moving no-slip wall relative to the adjacent cell zone. These conditions ensure a consistent simulation setup that mimics relative motion experienced in actual vehicle-ground interaction. The domain setup is illustrated in Figure 2.1.

2.3.2. 3D Simulations Boundary Conditions

For all 3D cases, appropriate inlet and outlet conditions are applied, and the exact positions of the boundaries are illustrated in Figure 2.5. For the straight-line simulation, the side walls and rear boundary are treated as outlets, while the front boundary is defined as a velocity inlet.

For the cornering simulations, two configurations are considered:

1. In the first configuration, the center of rotation is aligned with the aerodynamic center of the airfoil, as shown in Figure 2.5b.
2. In the second configuration, referred to as true cornering, the center of rotation is positioned at the midpoint of the wheelbase of a Formula 1 car. This point follows the actual racing line seen in real-world scenarios, where the car rotates perpendicularly about this axis. The position is calculated based on the dimensions of the Tyrrell 026 and is illustrated in Figure 2.5c, along with a top view of the Tyrrell 026 for reference [BrambleCFD, 2022; FindBlueprints, 2024; Lux, 2024].

For the simulation, the Moving Reference Frame (MRF) method in ANSYS Fluent is used, which is particularly suitable for simulating accelerating and rotating flows. Within the cell zone conditions, the moving reference frame is applied, where the frame velocity follows the profile shown in Figure 2.7, and rotational motion is applied where relevant.

The airfoil is modeled as a moving no-slip wall with a velocity of 0 m/s relative to the adjacent rotating frame. The bottom wall is treated as a moving no-slip wall with an absolute velocity of 0 m/s, and the top wall is similarly defined.

The inlet boundary condition is specified as a velocity inlet with a magnitude of 0 m/s in the absolute frame, while the outlet is defined as a pressure outlet with static pressure of 0 Pa in the absolute frame. These choices ensure that the only motion is due to the frame and not external flow, which is critical for capturing transient aerodynamic loads in cornering scenarios.

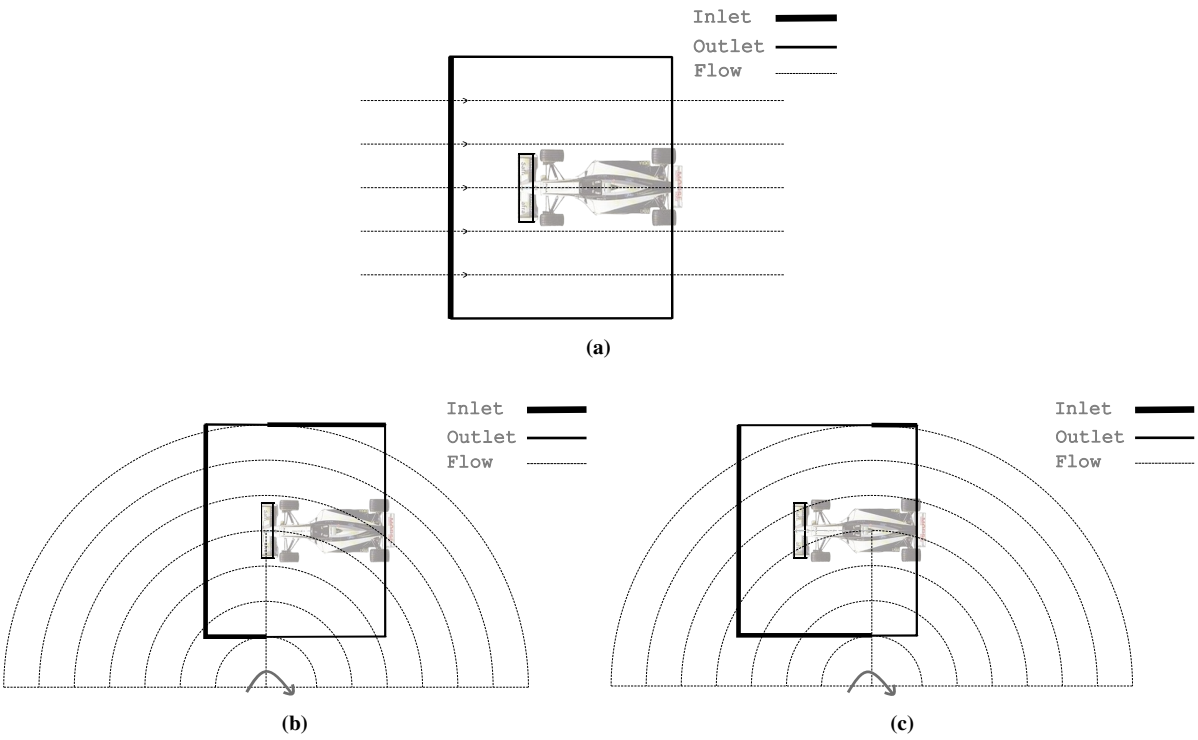

Figure 2.5: Top view of the computational domain (see Figure 2.2) showing the applied boundary conditions for different flow configurations with T026 F1 car [FindBlueprints, 2024]: (a) Straight Line (b) Cornering Normal - Flow with the center of rotation along the airfoil center (c) Cornering Yaw - Flow with center of rotation along the center of wheelbase (Not to be scaled)

2.4. Governing Equations and Turbulence Modeling

The flow simulations are carried out using *ANSYS Fluent 2023 R2*, which employs the Finite Volume Method (FVM) to solve the incompressible Navier–Stokes (NS) equations. The assumption of incompressibility is justified by the low Mach numbers typically encountered in Formula 1 applications. The Mach number is defined as $Ma = \frac{v}{c_s}$, where v is the flow velocity and c_s is the speed of sound. For the velocities considered in this study, $Ma \approx 0.1$, indicating negligible density variations. Therefore, the incompressible formulation is appropriate for the present analysis.

The governing equations differ depending on the simulation approach. This study distinguishes between the absolute frame and the moving frame methods. The absolute frame method is widely adopted in literature and its governing equations are detailed in subsection 2.4.1. However, the moving frame method, which is more relevant to the present work, is employed in the simulations and its governing equations are presented in subsection 2.4.2.

2.4.1. Absolute Frame Method Governing Equations

The equation for conservation of mass or continuity equation is written in Equation 2.4, where ρ is the density, $\vec{v}$ is the velocity vector and S_m is the mass added to the continuous phase from the dispersed second phase and any user-defined sources [ANSYS Inc., 2021].

$$\frac{\partial \rho}{\partial t} + \nabla \cdot (\rho \vec{v}) = S_m \tag{2.4}$$

The conservation of momentum is described in Equation 2.5, where M_{terms} shows the acceleration moment terms which comes into play for accelerating and decelerating flows which comprises of Corolis acceleration, $\vec{a_{cor}} = 2\vec{\omega} \times \vec{v}$, Centripetal acceleration, $\vec{a_c} = \vec{\omega} \times \vec{\omega} \times \vec{r}$, Angular acceleration, $\vec{\alpha} = \frac{d\vec{\omega}}{dt}$ and the linear acceleration is $\vec{a} = \frac{d\vec{v}}{dt}$. $\omega = \nabla \times \vec{v}$ is the angular velocity, p is the static pressure, $\overline{\overline{\tau}}$ is the stress tensor (Equation 2.6) and $\rho\vec{g}$, $\vec{F}$ are the gravitational body force and external body forces respectively [ANSYS Inc., 2021].

Coriolis acceleration and centripetal acceleration arise in both steady motion and unsteady motion. In contrast, the angular acceleration and linear acceleration terms appear only when there is a time-varying change in the rotational speed and translational velocity, respectively. These unsteady terms are absent when the motion involves constant translational and/or rotational velocities.

$$\frac{\partial}{\partial t}(\rho \vec{v}) + \nabla \cdot (\rho \vec{v} \vec{v}) + \underbrace{\rho(\vec{a_{cor}} + \vec{a_c} + \vec{\alpha} + \vec{a})}_{\text{Acc Momentum Term }, M_{terms}} = -\nabla p + \nabla \cdot (\overline{\overline{\tau}}) + \rho\vec{g} + \vec{F} \tag{2.5}$$

The stress tensor $\overline{\overline{\tau}}$ is given by Equation 2.6, where μ is the molecular viscosity, I is the unit tensor, and the second term on the right hand side is the effect of volume dilation [ANSYS Inc., 2021].

$$\overline{\overline{\tau}} = \mu \left[\left(\nabla \vec{v} + \nabla \vec{v}^T \right) - \frac{2}{3} \nabla \cdot \vec{v} I \right] \tag{2.6}$$

The governing equations, namely the conservation of mass and momentum are modified under the assumption of incompressibility, i.e., the density remains constant with respect to time. As a result, the equations simplify accordingly. The resulting forms of the mass and momentum equations in the absolute frame are presented in Equation 2.7 and Equation 2.8 [ANSYS Inc., 2021; SimScale, 2023].

$$\frac{\partial u_i}{\partial x_i} = 0 \tag{2.7}$$

$$\rho \left(\frac{\partial u_i}{\partial t} + \frac{u_j \partial u_i}{\partial x_j} \right) + \underbrace{\rho \left(2\vec{\omega_i} \times \vec{u_i} + \vec{\omega_i} \times \vec{\omega_i} \times \vec{r} + \frac{d\vec{\omega_i}}{dt} + \frac{d\vec{u_i}}{dt} \right)}_{\text{Acc Momentum Term }, M_{terms}} = -\frac{\partial p}{\partial x_i} + \mu \frac{\partial^2 u_i}{\partial x_j^2} \tag{2.8}$$

The Reynolds Averaged Navier Stokes (RANS) model is employed for simulating turbulence in this study. Compared to Direct Numerical Simulation (DNS) and Large Eddy Simulation (LES), RANS is computationally more efficient, making it suitable for complex engineering applications such as Formula 1 aerodynamics. While RANS provides a reasonable approximation of mean flow behavior, it lacks the ability to resolve detailed vortex structures, which limits its accuracy in capturing transient flow features.

We employ the eddy viscosity model, which assumes a mathematical analogy between the Reynolds stresses and the linear stress–strain relationship in a Newtonian fluid. This assumption is known as the Boussinesq approximation, which provides a simplified expression for the Reynolds stress tensor in terms of the turbulent kinetic energy k, the eddy viscosity μ_t, and the mean strain rate.

There are several types of eddy viscosity models; however, for this study, the $k-\omega$ model is chosen due to its wellestablished accuracy and reliability. This model involves solving two additional transport equations: one for the turbulent kinetic energy k, and another for the specific dissipation rate ω. Within the $k-\omega$ framework, the SST $k-\omega$ model is adopted, as it ensures a smooth transition from the standard $k-\omega$ model in the near-wall region to a high Reynolds number variant in the outer region of the boundary layer.

The SST $k-\omega$ model has proven to be robust across a wide range of flows, particularly in cases involving strong adverse pressure gradients and flow over aerodynamic surfaces. Compared to the standard $k-\omega$ model, it offers improved prediction capability for flow separation and wake behavior, making it especially suitable for simulating flow over airfoils [ANSYS Inc., 2024]. Previous studies involving airfoils have demonstrated that the SST $k-\omega$ model effectively captures key aerodynamic phenomena such as boundary layer development, separation, and wake dynamics [Keogh, Doig, et al., 2015; Pathanadka, 2022; Zerihan and Zhang, 2001b; Zhou, 2023]. The coefficients of the turbulence model are shown in Table 2.2.

2.4.2. Moving Frame Method Governing Equations

A moving reference frame is also used, which leads to modifications in the velocity definitions and the governing equations [ANSYS Inc., 2021]. The relative velocity is the velocity observed from the moving (non-inertial) frame, whereas the absolute velocity is observed from a stationary (inertial) frame. First, we examine how the velocity transforms, as shown in Equation 2.9:

$$\vec{v}_r = \vec{v} - \vec{u}_r \tag{2.9}$$

where $\vec{v}_r$ is the relative velocity, $\vec{v}$ is the absolute frame velocity and $\vec{u}_r$ is the velocity of the moving frame relative to the inertial frame and is given in Equation 2.10.

$$\vec{u}_r = \vec{v}_t + \vec{\omega}_r \times \vec{r} \tag{2.10}$$

where $\vec{v}_t$ is the translational frame velocity, $\vec{\omega}_r = \nabla \times \vec{v}_r$ is the angular velocity and $\vec{r}$ is the position vector from the origin of the moving frame.

As discussed in subsection 2.4.1, the relevant governing equations are the conservation of mass (Equation 2.11) and momentum (Equation 2.12), modified for the moving frame as follows:

$$\frac{\partial \rho}{\partial t} + \nabla \cdot \rho \vec{v}_r = 0 \tag{2.11}$$

$$\frac{\partial}{\partial t}(\rho \vec{v}_r) + \nabla \cdot (\rho \vec{v}_r \vec{v}_r) + \underbrace{\rho\,(2\vec{\omega}_r \times \vec{v}_r + \vec{\omega}_r \times \vec{\omega}_r \times \vec{r} + \vec{\alpha}_r \times \vec{r} + \vec{a}_r)}_{\text{Acc Momentum Term, } M_{terms}} = -\nabla p + \nabla \cdot \bar{\bar{\tau}}_r + \vec{F} \tag{2.12}$$

Although the form of the governing equations remains consistent, the distinction lies in the velocity terms: the absolute frame equations employ absolute velocities and angular velocities, whereas the moving frame equations are expressed in terms of relative velocities, as defined in Equation 2.9.

In the momentum equation (Equation 2.12) within the moving frame, four additional acceleration terms emerge. These are formulated using relative velocity and include: the coriolis acceleration $a_{cor_r} = 2\vec{\omega}_r \times \vec{v}_r$, the centripetal acceleration $a_{c_r} = \vec{\omega}_r \times \vec{\omega}_r \times \vec{r}$, the angular acceleration $\vec{\alpha}_r = \frac{d\vec{\omega}_r}{dt}$, and the linear acceleration $\vec{a}_r = \frac{d\vec{v}_t}{dt}$. Other terms include the viscous stress tensor $\bar{\bar{\tau}}_r$ and the body force $\vec{F}$. The viscous stress tensor is expressed as:

$$\bar{\bar{\tau}}_r = \mu \left[\left(\nabla \vec{v}_r + \nabla \vec{v}_r^T \right) - \frac{2}{3} \nabla \cdot \vec{v}_r I \right] \tag{2.13}$$

where μ is the molecular velocity, I is the unit tensor.

As discussed in subsection 2.4.1, both coriolis (a_{cor_r}) and centripetal (a_{c_r}) accelerations are present under steady and unsteady conditions, while angular ($\vec{\alpha}_r$) and linear ($\vec{a}_r$) accelerations arise only when there are time-varying rotational or translational velocities. These latter terms become zero under constant translation and/or rotation.

Among the available eddy viscosity models, the SST k-ω model is selected for this study, consistent with its use in the absolute frame (as discussed in subsection 2.4.1). Prior studies involving airfoils have shown that the SST k–ω model effectively captures essential aerodynamic features such as boundary layer evolution, separation, and wake behavior [ANSYS Inc., 2024; Keogh, Doig, et al., 2015; Pathanadka, 2022; Zerihan and Zhang, 2001b; Zhou, 2023]. The coefficients of the turbulence model are shown in Table 2.2.

2.5. Solution Methods

The moving frame is selected for the CFD simulation as it replicates the real-life movement of the front wing, where, in practice, the wing moves through the air. This choice better represents the relative motion between the wing and the surrounding fluid. Hence, this method is used and explained in detail in subsubsection A.2.2.3. As the flow undergoes acceleration and deceleration, there are some additional acceleration-induced moment terms (see Equation 2.12) which are not straightforward to model. Using the moving frame simplifies this complexity, particularly in the cornering case.

Due to the presence of acceleration and deceleration in the flow, the concept of added mass becomes important. The added mass effect refers to the inertia imparted to the surrounding fluid as the body accelerates or decelerates, resulting in additional force and moment components. The added mass matrix helps to approximate this difference. It facilitates the computation of added mass forces and moments in the three linear force directions: $F_{D_{am}}$, $F_{L_{am}}$, and $F_{S_{am}}$ as well as the three rotational moment directions: $M_{\phi_{am}}$, $M_{\psi_{am}}$, and $M_{\theta_{am}}$. These components are key factors in accelerating and decelerating flows [Pathanadka, 2022; Zhou, 2023]. The added mass effect is mathematically given by:

$$\mathbf{F} = -\rho \dot{U}_i \iint_{S_B} \phi_i \mathbf{n} dS - \rho U_i \Omega \times \iint_{S_B} \phi_i \mathbf{n} dS \tag{2.14}$$

where $\mathbf{F}$ is the hydrodynamic force, ρ is the fluid density, $\dot{U}_i$ is the time derivative of the velocity component U_i, Ω is the angular velocity vector, ϕ_i are the Kirchhoff potentials, S_B is the surface of the body, and $\mathbf{n}$ is the outward-pointing surface normal.

From this formulation, the total force and moment on a moving body can be expressed in terms of the added mass and added moment coefficients (see Equation 2.15):

$$\begin{aligned} F_j &= -\dot{U}_i m_{ji} - \varepsilon_{jkl} U_i \Omega_k m_{li}, \\ M_j &= -\dot{U}_i m_{j+3,i} - \varepsilon_{jkl} U_i \Omega_k m_{l+3,i} - \varepsilon_{jkl} U_i U_k m_{li} \end{aligned} \tag{2.15}$$

Here, F_j and M_j are the j^{th} components of the hydrodynamic force and moment, respectively; ε_{jkl} is the Levi-Civita symbol; and m_{ij} are the added mass matrix components of M_a. The indices $j, k, l \in 1, 2, 3$ refer to the linear components, while indices $i, 4, 5, 6$ denote rotational components [Newman, 2018]. Where M_a is given by

$$M_a = \begin{bmatrix} m_{11} & m_{12} & m_{13} & m_{14} & m_{15} & m_{16} \\ m_{21} & m_{22} & m_{23} & m_{24} & m_{25} & m_{26} \\ m_{31} & m_{32} & m_{33} & m_{34} & m_{35} & m_{36} \\ m_{41} & m_{42} & m_{43} & m_{44} & m_{45} & m_{46} \\ m_{51} & m_{52} & m_{53} & m_{54} & m_{55} & m_{56} \\ m_{61} & m_{62} & m_{63} & m_{64} & m_{65} & m_{66} \end{bmatrix} \tag{2.16}$$

The coefficients represent combinations for each degree of freedom: 1 represents the x direction, 2 the y direction, 3 the z direction, 4 the ϕ angular direction, 5 the ψ angular direction, and 6 the θ angular direction [Massachusetts Institute of Technology, 2005; Severholt, 2017].

The final expression in Equation 2.15 depends solely on the body's velocity, acceleration components, and the added mass coefficients m_{ij}, making it directly applicable to the unsteady CFD analysis of the front wing under dynamic manoeuvres.

For the simulation settings, a pressure based solver was adopted since compressibility effects are negligible at the flow velocities considered, consistent with previous studies. The pressure–velocity coupling was handled using the coupled scheme, which solves all governing equations simultaneously over the domain. This scheme is more robust for flows with complex geometries and strong pressure gradients, albeit computationally expensive [Analytics, n.d.].

Given the priority on accuracy, the coupled scheme was selected, along with Rhie–Chow momentum interpolation, which was kept constant throughout the simulation. For spatial discretization of gradients, the Least Squares Cell-Based method was chosen for its computational efficiency. Pressure was discretized using a Second-Order scheme.

For momentum, the Third-Order MUSCL scheme was used, as it combines second-order upwind stability with central differencing accuracy. This choice is particularly useful in resolving shear layers and wake structures. For turbulent kinetic energy (k) and specific dissipation rate (ω), Second-Order Upwind schemes were employed to preserve accuracy in boundary layers. A Bounded Second-Order Implicit time discretization was used to improve numerical stability, particularly for bounded quantities like k and ω.

These solver settings align with those used in validated studies of front wings operating under ground effect conditions [ANSYS Inc., 2024; Pathanadka, 2022], and are summarized in Table 2.2.

Table 2.2: Simulation Settings for 2D and 3D Flow Analysis

Parameter	**Type**
Solver	
Type	Pressure-Based
Time	Transient
Velocity formulation	Absolute
Turbulence Model	
Model	SST k-ω
Near-Wall Treatment	correlation
Options	Production Limiter
Transition Model	none
α^*_∞	1.00
α_∞	0.52
β^*_∞	0.09
a_1	0.31
β_i (Inner)	0.075
β_i (Outer)	0.0828
TKE (Inner) Prandtl	1.176
TKE (Outer) Prandtl	1.00
SDR (Inner) Prandtl	2.00
SDR (Outer) Prandtl	1.168
Production Limiter Clip Factor	10.00
Materials	
Density, ρ [kg/m^3]	1.225
Dynamic Viscosity, μ [Pa s]	$1.789 * 10^{-5}$
Cell Zone Conditions	
Phase	Fluid (all volumes)
Operating Pressure [Pa]	101325
Reference Pressure Location	Velocity Inlet BC
Solution Methods	
Pressure Velocity Coupling Scheme	Coupled
Flux Type	Rhie-Chow: momentum based
Gradient	Least Squares Cell Based
Pressure	Second Order
Momentum	Third-Order MUSCL
Turbulent Kinetic Energy	Second Order Upwind
Specific Dissipation Rate	Second Order Upwind
Transient Formulation	Bounded Second Order Implicit

2.6. Velocity, Acceleration Profile and Simulation Path

To define the target velocity for the simulation, the reference corner chosen in this study is the Fairmont Hairpin at the Circuit de Monaco, one of the slowest and tightest corners in Formula 1 (see Figure 2.6). The minimum cornering velocity, based on actual F1 telemetry data, is approximately 65 km/h, and this value is used as the baseline for determining the corresponding velocity for the 80% scaled model [F1 Chronicle, 2023].

Using a scaled-down model provides significant computational advantages, such as reduced mesh size, lower memory usage, and faster simulation times. However, this approach introduces important trade-offs. Specifically, reducing the geometric scale while keeping the same freestream velocity lowers the Reynolds number, which can significantly influence flow characteristics.

To preserve dynamic similarity, the Reynolds number must be matched by increasing the freestream velocity for the scaled model. This adjustment, however, increases the Courant number (Co), which may require a reduction in time-step size to maintain numerical stability, ultimately raising computational cost. Thus, selecting an appropriate model scale involves carefully weighing these competing effects.

The 80% scaled Tyrrell 026 front wing was chosen for this study as it is a well-validated configuration frequently used in literature [Pathanadka, 2022; Zerihan and Zhang, 2001a]. The influence of Reynolds number preservation, Courant number constraints, and time-step selection in setting the simulation velocity is further explained in Figure 2.7.

To ensure Reynolds number similarity (see Equation 2.17), only the velocity is adjusted while all other parameters such as viscosity and characteristic length remain fixed. The final scaled velocity used in the simulation is calculated accordingly and presented in Table 2.3. Additionally, the corner radius is scaled by the same 80% ratio to maintain geometric consistency throughout the simulation.

$$Re = \frac{\rho u c}{\mu} \tag{2.17}$$

Table 2.3: Comparison of Tyrell 026 F1 full size car to its 80% scaled model

	Tyrell 026	**Simulation Model (80% scaled Model)**
Radius of Corner, R_{corner} [m]	10	8
Chord Length of the airfoil [m]	0.27925	0.2234
Velocity [m/s]	18.056	22.57
Re [-]	345255.40	345255.40

As our primary focus is on the cornering behavior, we calculate the velocity and time required for the car/wing to navigate the Monaco corner, and use the same parameters for the straight-line case to enable a direct comparison. The calculations assume an idealized 180° turn, with deceleration beginning at 0°, ceasing at 90°, where acceleration starts, and continues until 180°, as illustrated in Figure 2.6. The velocity profiles are generated using two different acceleration values, specifically 2g and 5g, as detailed in Table 2.4.

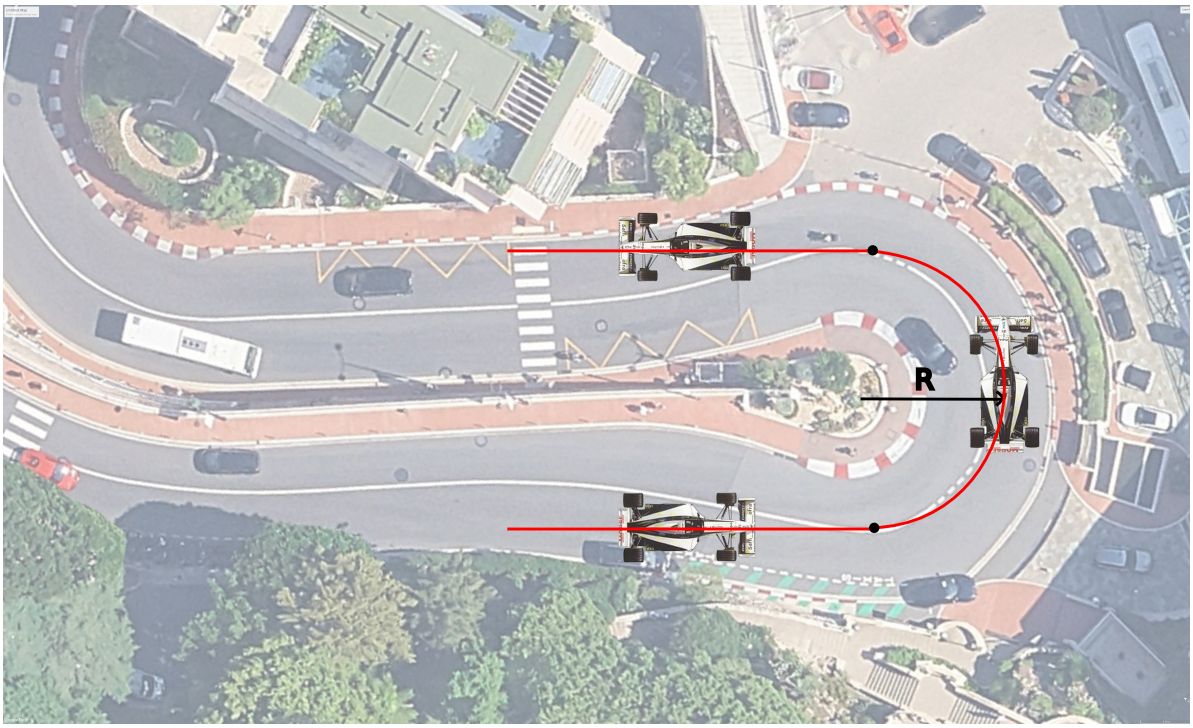

Figure 2.6: Top view of the Monaco Fairmont Hairpin corner on the F1 Monaco Circuit. The red line indicates the simulated path used as reference, with R representing the corner radius. The two black dots mark the start and end points of the cornering section [FindBlueprints, 2024; Google Earth Pro, 2025]

Table 2.4: Velocity and acceleration data along with the time for each phase of the simulation

	Acceleration/Deceleration Values	
	2g	**5g**
Acceleration Value, a [m/s^2]	19.6	49
Minimum Velocity, u_{min} [m/s]	22.57	22.57
Maximum Velocity, u_{max} [m/s]	31.88	42.17
Time for Initial Straight Line, $t_{initial}$ [s]	0.5	0.5
Time for Deceleration/Acceleration, $t_{dec,acc}$ [s]	0.475	0.4
Time for Final Straight Line, t_{final} [s]	0.5	0.5
Total Time, t_{total} ($t_{initial} + 2 \times t_{dec,acc} + t_{final}$) [s]	1.95	1.8

The simulation begins with an initial time period, $t_{initial}$, during which the wing travels in a straight line at a constant velocity of u_{max}. After this phase, the wing begins to decelerate over a duration of $t_{dec,acc}$, either while cornering or continuing in a straight line, depending on the simulation scenario until it reaches a minimum velocity of u_{min}.

This deceleration phase is then followed by an acceleration period, again occurring either during cornering or in straight-line motion, depending on the case. Eventually, the wing resumes motion at a constant velocity of u_{max} in straight-line travel.

The equations used to define these velocity and acceleration profiles are discussed in detail below and illustrated in Figure 2.7.

For the straight line case, the effective velocity at the aerodynamic center of the airfoil is set equal to the prescribed velocity profile. Subsequently, the linear velocity, $u(t)$, and linear acceleration, $a(t)$ are described in Equation 2.18 and Equation 2.19, where t is the simulation time.

$$u(t) = \begin{cases} u_{max} & t \leq t_{initial} \\ u_{max} - a(t - t_{initial}) & t_{initial} < t \leq (t_{initial} + t_{dec,acc}) \\ u_{min} + a(t - (t_{initial} + t_{dec,acc})) & (t_{initial} + t_{dec,acc}) < t \leq (t_{initial} + 2 \times t_{dec,acc}) \\ u_{max} & t > t(t_{initial} + 2 \times t_{dec,acc}) \end{cases} \tag{2.18}$$

$$a(t) = \begin{cases} 0 & t \leq t_{initial} \\ -a & t_{initial} < t \leq (t_{initial} + t_{dec,acc}) \\ a & (t_{initial} + t_{dec,acc}) < t \leq (t_{initial} + 2 \times t_{dec,acc}) \\ 0 & t > (t_{initial} + 2 \times t_{dec,acc}) \end{cases} \tag{2.19}$$

For the cornering case, the effective velocity at the aerodynamic center of the airfoil is set equal to the prescribed velocity profile. Subsequently, the angular velocity, $\omega(t)$, and angular acceleration, $\alpha(t)$, are determined by dividing the linear velocity and acceleration profiles by the effective cornering radius, R_{eff} during the cornering phase, as described in Equation 2.20 and Equation 2.21, where t is the simulation time.

$$\omega(t) = \begin{cases} 0 & t \leq t_{initial} \\ \frac{u_{max} - a(t - t_{initial})}{R_{eff}} & t_{initial} < t \leq (t_{initial} + t_{dec,acc}) \\ \frac{u_{min} + a(t - (t_{initial} + t_{dec,acc}))}{R_{eff}} & (t_{initial} + t_{dec,acc}) < t \leq (t_{initial} + 2 \times t_{dec,acc}) \\ 0 & t > t(t_{initial} + 2 \times t_{dec,acc}) \end{cases} \tag{2.20}$$

$$\alpha(t) = \begin{cases} 0 & t \leq t_{initial} \\ \frac{-a}{R_{eff}} & t_{initial} < t \leq (t_{initial} + t_{dec,acc}) \\ \frac{a}{R_{eff}} & (t_{initial} + t_{dec,acc}) < t \leq (t_{initial} + 2 \times t_{dec,acc}) \\ 0 & t > (t_{initial} + 2 \times t_{dec,acc}) \end{cases} \tag{2.21}$$

From Table 2.4, it is evident that the time required to complete the corner varies between the $2g$ and $5g$ acceleration profiles. To enable a meaningful comparison between the $2g$ and $5g$ datasets, time is normalized using Equation 2.22, where t_{start} denotes the beginning of the deceleration phase and t_{end} represents the conclusion of the acceleration phase. The corresponding velocity and acceleration profiles plotted against the normalized time (t^*) are presented in Figure 2.7, generated using Equation 2.18, Equation 2.19, Equation 2.20, Equation 2.21, and Equation 2.22.

$$t^* = \frac{t - t_{start}}{t_{end} - t_{start}} \tag{2.22}$$

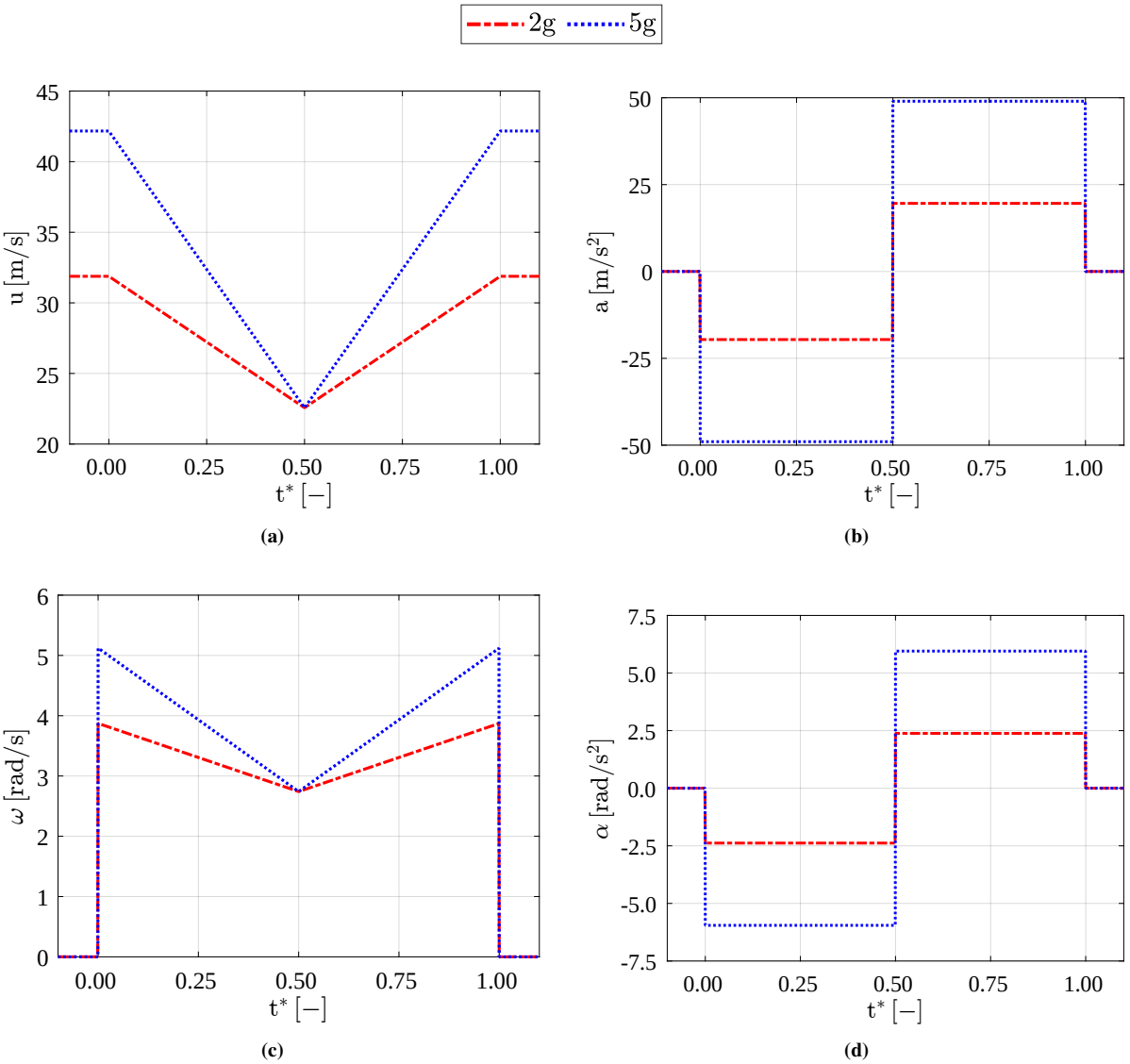

Figure 2.7: Velocity and acceleration profiles plotted against normalized time, t^* (Equation 2.22), for $2g$ and $5g$ acceleration cases: (a) Linear velocity, u (b) Linear acceleration, a (c) Angular velocity, ω (d) Angular acceleration, α

These velocity profiles are used to prescribe the motion of the rotating frame. It is important to note that in the rotating reference frame approach, the coordinate system rotates along with the frame. Therefore, when defining the velocity profiles, the directional components must be expressed relative to this rotating coordinate system.

Since the simulations are transient (i.e., time-dependent), the choice of an appropriate time step is critical for ensuring both accuracy and stability. The time step must be consistent with the local mesh size and the imposed velocity fields. To assess this, the Courant number, Co, a non-dimensional parameter widely used in computational fluid dynamics (CFD), is utilized. It defines the ratio of the distance traveled by a fluid particle in one time step to the local mesh spacing and is expressed as [IdealSimulations, 2024]:

$$\mathrm{Co} = \frac{\mathrm{U}\Delta\mathrm{t}}{\Delta\mathrm{h}} \tag{2.23}$$

where U is the local flow velocity, Δt is the time step size, and Δh is the local mesh size.

According to the Courant Friedrichs Lewy (CFL) condition, for explicit and semi-implicit schemes, the Courant number must satisfy [IdealSimulations, 2024]:

$$\mathrm{Co} = \frac{\mathrm{U}\Delta\mathrm{t}}{\Delta\mathrm{h}} \leq Co_{max} \tag{2.24}$$

where $Co_{\max}$ is the maximum allowable Courant number. To ensure numerical stability and accuracy, $Co_{\max}$ is typically kept less than or equal to 1. This condition ensures that information does not propagate beyond one cell per time step, which could otherwise lead to non-physical results and numerical instabilities as shown in Figure 2.8.

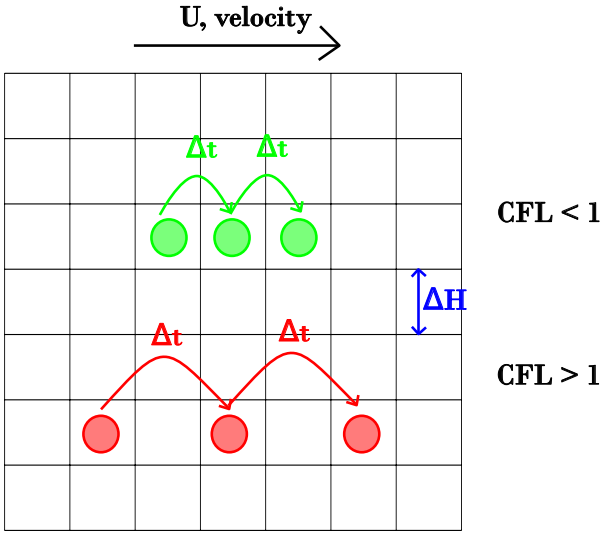

Figure 2.8: Visualization of the Courant number, Co, and the Courant Friedrichs Lewy (CFL) condition on a representative computational grid. The illustration shows the relationship between the time step size (Δt), local mesh size (Δh), and flow velocity (U).

For the 3D simulations conducted, it was determined that a time step of $\Delta t = 0.001$ s was appropriate for the $2g$ cornering case, while a finer time step of $\Delta t = 0.0005$ s was required for the $5g$ case. This difference arises due to the increased flow velocities in the $5g$ scenario, which result in higher Courant numbers for the same grid resolution. To maintain $Co \leq 1$ across the domain, the time step was adjusted accordingly. Consequently, the $5g$ simulation required approximately twice the number of time steps to reach the same physical time as the $2g$ case.

3

Simulation Results

3.1. 2D Simulation

3.1.1. Mesh Independent study

A 2D mesh independence study was conducted to determine an appropriate resolution around the airfoil surface, using the number of discretization points on the airfoil, n, as the primary parameter. The simulation setup included a ground clearance of $h = 0.224c$, a chord length of 223.4 mm, and an aspect ratio of 4.92, identical to the configuration used for the 3D front wing. The mesh was generated to ensure a non-dimensional wall distance of $y^+ < 1$ (Equation 2.1) near both the airfoil surface and the lower ground wall, ensuring adequate near-wall resolution for turbulence modeling.

Five mesh configurations were tested, with n = 165, 215, 315, 365, and 415 points along the airfoil surface. The inlet flow velocity was set at a constant 30 m/s. As shown in Figure 3.1, the variation in computed drag and lift forces between $n = 365$ and $n = 415$ was negligible, indicating mesh convergence. Therefore, $n = 415$ was selected as the baseline resolution for subsequent 3D simulations.

This resolution provides a solid foundation for accurate 3D results and is used as the basis for the 3D meshing strategy, as discussed in more detail in subsection 3.2.1.

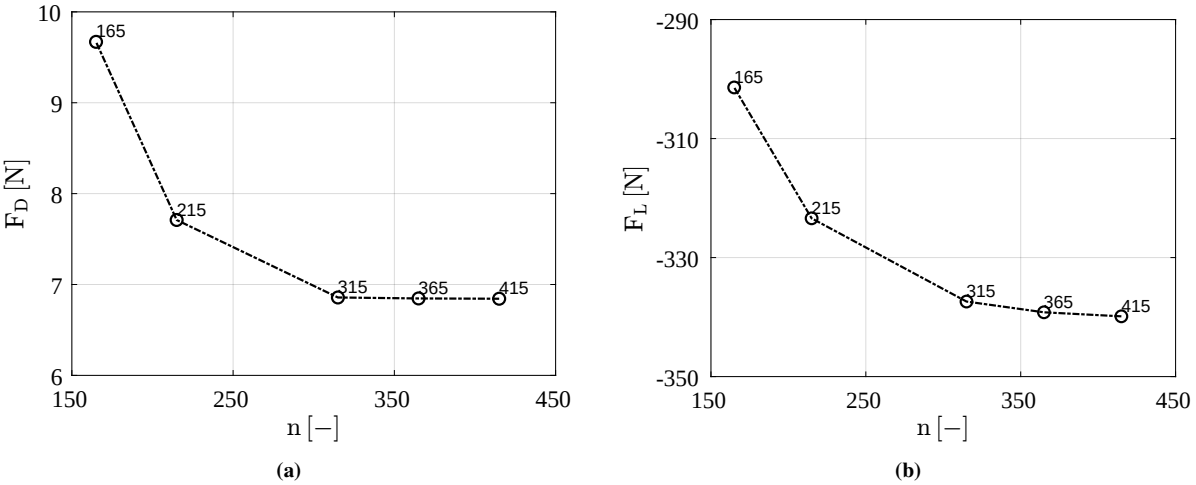

Figure 3.1: Variation of Aerodynamic forces for five different points on the airfoil where n shows the number of points on the airfoil (a) Drag Force, F_D (b) Lift Force, F_L

3.2. 3D Simulation

3.2.1. Mesh Independent study

A conventional mesh independence study could not be performed due to specific design constraints in the meshing strategy for the 3D simulation. Instead, the primary criterion for mesh quality was based on matching the number of surface cells on the airfoil to the optimal value obtained from the 2D mesh independence study (subsection 3.1.1). The surface mesh was fixed accordingly to maintain geometric consistency and to accurately resolve the airfoil curvature.

To ensure a wall-resolved mesh, the first cell height was adjusted to achieve a target non-dimensional wall distance of $y^+ < 1$ near both the airfoil surface and the lower ground plane. Additionally, multiple refinement zones were applied to allow a smooth gradation in cell sizes from the wall regions to the far-field domain, thus balancing accuracy and numerical stability. The overall meshing approach is illustrated in Figure 2.4.

Due to the absence of a traditional mesh convergence study, the mesh was validated by comparing simulation results with those from a prior validated study under similar straight-line flow conditions at an inlet velocity of 30 m/s. The resulting aerodynamic coefficients of drag and lift were evaluated and found to be in good agreement with the reference values, as shown in Table 3.1.

Table 3.1: Comparison of Present Simulation Results with Literature Values for the Straight-Line Case

	Present Simulation	Reference Data [Pathanadka, 2022]
Drag Force, F_D [N]	6.933	6.920
Lift Force, F_L [N]	-143.220	-143.119

From Table 3.1, it is evident that the present simulation closely matches the reference data, with negligible differences in both drag and lift forces. This agreement indicates that the near-wall mesh is well-resolved and that the applied meshing strategy yields physically reliable results

To further evaluate mesh quality, the velocity magnitude distribution in the relative frame, $v_{r_{mag}}$ (Equation 3.1) is assessed along several vertical lines in the center plane of the airfoil, as shown in Figure 3.2. The velocity magnitude in the relative frame is computed using by calculating the individual components (v_{r_x}, v_{r_x} and v_{r_x}) using Equation 2.9:

$$v_{r_{mag}} = \sqrt{(v_{r_x}^2 + v_{r_y}^2 + v_{r_z}^2)} \tag{3.1}$$

These velocity profiles are evaluated at six streamwise locations: $-1.0c$, $-0.5c$, $0c$ (leading edge), $0.5c$, $1.0c$ (trailing edge), and $1.5c$, relative to the chord length, c. The corresponding visual results are shown in Figure 3.2.

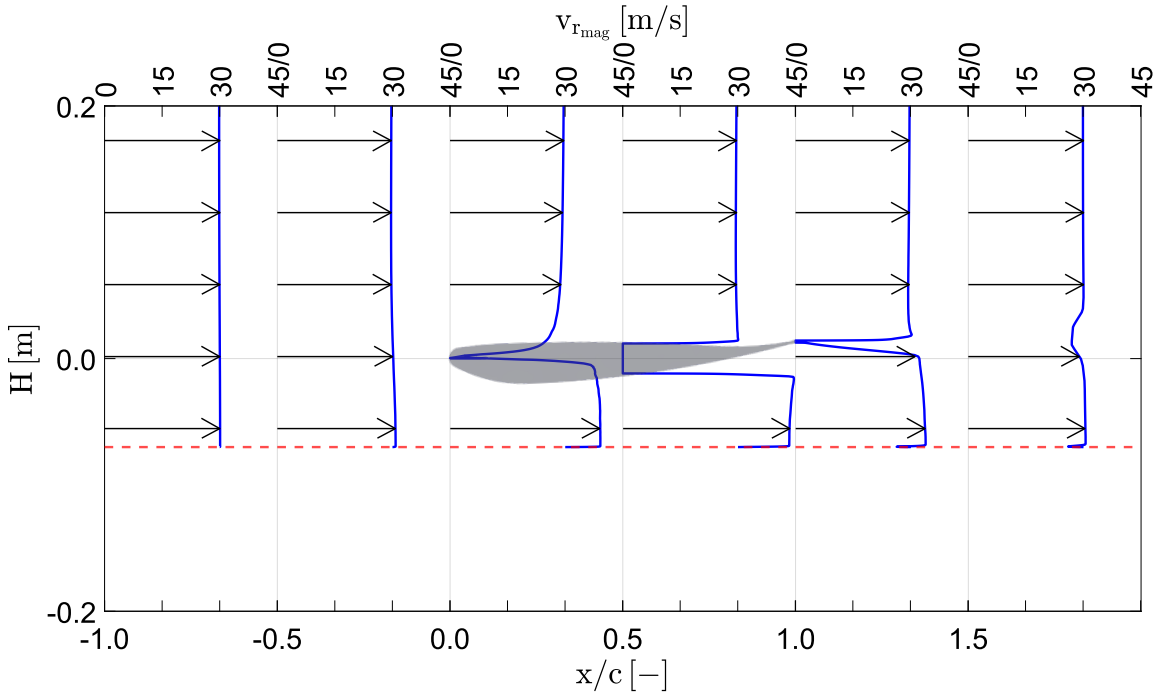

Figure 3.2: Velocity magnitude in the relative frame, $v_{r_{mag}}$, distribution at various streamwise locations along the center plane of the front wing: $-1.0c$, $-0.5c$, $0c$, $0.5c$, $1.0c$, and $1.5c$, where c is the chord length of the airfoil. The x-axis is normalized by chord length, and the y-axis represents the vertical distance from the bottom wall. The reference origin ($x = 0$) is taken at the leading edge of the airfoil. The airfoil geometry is shown for visual reference only and is not to scale. The blue lines represent the velocity magnitude in the relative frame, $v_{r_{mag}}$, and the red horizontal line indicates the bottom wall boundary of the simulation domain.

As observed, the flow velocity upstream of the airfoil (at $-1.0c$) closely matches the freestream velocity of 30 m/s. Near the airfoil surface, velocity drops to zero, consistent with the no-slip condition, including at the leading and trailing edge. On the suction side, velocity increases above the freestream value due to flow acceleration over the curved surface, while on the pressure side, it smoothly transitions back toward the freestream as distance from the surface increases. These trends confirm that the velocity field evolves smoothly, consistent with real-world aerodynamic behavior, validating the fidelity of the mesh.

Therefore, despite not conducting a full mesh independence study, the close match with validated results and smooth velocity transitions justify the mesh configuration employed. A detailed breakdown of the meshing strategy, refinement zones, and associated settings is provided in section 2.2.

3.2.2. Simulation Results

To begin, a steady-state simulation was conducted to analyze the differences between straight line motion, normal cornering, and cornering with yaw. These results are detailed in subsubsection 3.2.2.1, with the corresponding domain setups and boundary condition variations illustrated in Figure 2.5. Building upon these preliminary findings, a more comprehensive investigation into accelerating and decelerating flows during cornering and straight-line scenarios is presented in subsubsection 3.2.2.2.

3.2.2.1. Straight Line vs Cornering Normal vs Cornering Yaw

Initial analysis was conducted to understand the differences between straight line motion, cornering normal, and yaw cornering. The key parameters examined are the coefficients of force, C_F (including drag, lift, and side forces), and the coefficients of moments, C_M (rolling, yawing, and pitching moments). These coefficients are calculated as follows:

$$C_F = \frac{2 \times F}{\rho u^2 A} \tag{3.2}$$

$$C_M = \frac{2 \times M}{\rho u^2 A l} \tag{3.3}$$

where F is the respective force, M is the respective moment, ρ is the fluid density, u is the flow velocity, A is the reference area of the wing, and l is the reference length. In this study, the density ρ is taken as 1.225 kg/m^3, the reference area A is calculated as the chord length c multiplied by the span length s, and the reference length l is the chord length c. For this set of results, the velocity magnitude at the aerodynamic center was set to $30m/s$ for all three cases to allow a consistent comparison of the data.

From Figure 3.3a, a comparison of the force coefficients reveals that the drag coefficient C_D remains relatively consistent across all three cases. The lift coefficient C_L shows a slight reduction in the cornering yaw configuration compared to the other two. As expected, the side force coefficient C_S is approximately zero for both the straight-line and normal cornering cases, while a significant non-zero C_S is observed in the cornering yaw case, indicating lateral aerodynamic loading.

Comparing the coefficient of moments from Figure 3.3b, it can be observed that C_{M_ϕ}, for a straight line, is zero while there is a C_{M_ϕ} for cornering with a higher magnitude value for cornering yaw compared to cornering normal. For C_{M_ψ}, for a straight line it was again zero, but for cornering C_{M_ψ} is opposite and by magnitude it is higher for cornering yaw. For C_{M_θ}, it is almost the same for both straightline and cornering normal, but it was observed that the magnitude of the value for lower for cornering with yaw.

In terms of moment coefficients, shown in Figure 3.3b, the rolling moment coefficient C_{M_ϕ} is zero in the straight-line case but becomes non-zero during cornering, with a higher magnitude observed in the cornering yaw scenario compared to normal cornering. The yawing moment coefficient C_{M_ψ} is again zero in the straight-line case, while during cornering it is non-zero and of opposite sign for the two cornering types, with a greater magnitude in the yawing configuration. The pitching moment coefficient C_{M_θ} is similar between straight-line and normal cornering, but a reduction in magnitude is observed for cornering with yaw.

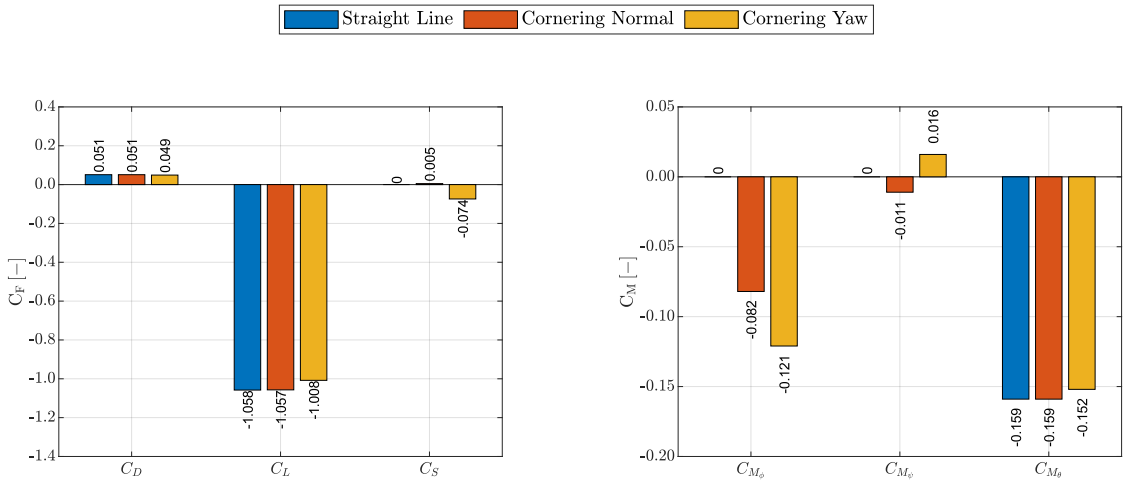

(a) **(b)**

Figure 3.3: Comparison of aerodynamic forces and moments for Straight Line, Cornering Normal, and Cornering Yaw cases: (a) Coefficient of Force, C_F (namely C_D, C_L, and C_S); (b) Coefficient of Moment, C_M (namely C_{M_ϕ}, C_{M_ψ}, and C_{M_θ})

To better understand these differences in the force and moment coefficients, the first step to analyse this different is to understand the velocity around the airfoil and see how the flow changes. to understand this the velocity magnitude is understand about how it changes along the streamwise direction of the downstream of the airfoil. As a moving frame is used the relative velocity magnitude, $v_{r_{mag}}$ is used which is calculated by Equation 3.1. Firdstly 3 different planes are selected to understand, at different distances from the leading edge along the airfoil chord length. The values it is understand is at $0.5c$, $1c$ and $1.5c$ from the leading edge as shown in Figure 3.4

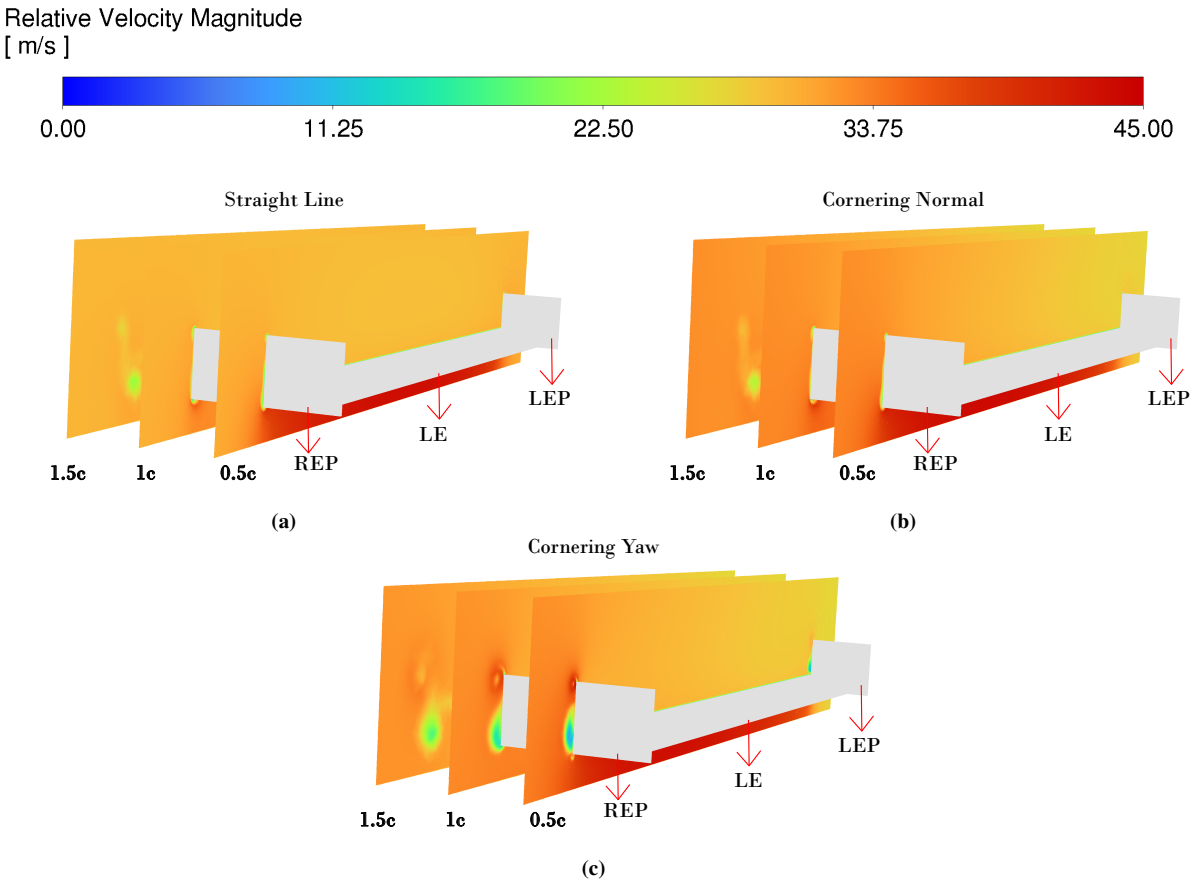

Figure 3.4: Velocity magnitude in the relative frame, $v_{r_{mag}}$ distributions in the spanwise direction at three streamwise locations: $0.5c$, $1c$, and $1.5c$ downstream of the airfoil leading edge (LE). LEP and REP denote the Left and Right EndPlate of the wing (a) Straight Line (b) Cornering Normal (c) Cornering Yaw

It was observed in Figure 3.4 that for the straight-line case (Figure 3.4a), the velocity magnitude distribution remains relatively symmetric across the span. However, a significant velocity change is noted near the endplates at the streamwise locations of $1c$ and $1.5c$ downstream of the leading edge. This indicates the development of wake structures or localized vortices near the endplates even under symmetric inflow.

In contrast, for the cornering normal condition (Figure 3.4b), the velocity near the REP is noticeably higher than that at the LEP. This asymmetry is consistent with the expected flow curvature due to the rotation of the domain, as described in Figure 2.5. Despite this difference in velocity distribution, the vortex strength and development near the endplates appear similar to those in the straight-line case.

For the cornering yaw configuration (Figure 3.4c), a similar trend of higher velocity at the REP compared to the LEP is observed. However, a distinct difference emerges: at the REP, regions of both significantly higher and lower velocity are present, unlike the other two cases. Particularly at $0.5c$, an early formation of a vortex-like structure can be seen, which becomes well-developed by $1c$.

To examine this phenomenon in greater detail, the velocity magnitude field at a fixed streamwise location of $1c$ from the airfoil leading edge is analyzed in Figure 3.5.

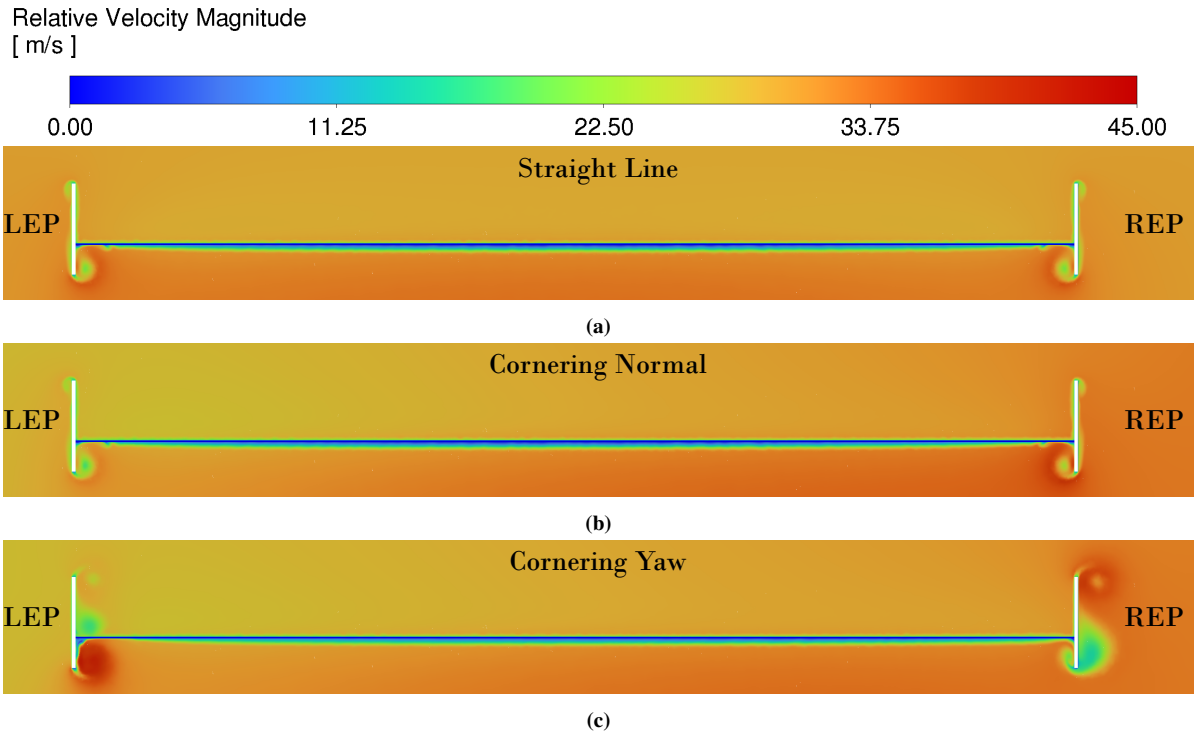

Figure 3.5: Velocity magnitude in the relative frame, $v_{r_{mag}}$ distribution at a plane located 1c downstream of the airfoil leading edge. LEP and REP denote the Left and Right EndPlate, respectively (a) Straight Line, (b) Cornering Normal, (c) Cornering Yaw.

In Figure 3.5a, the velocity field for the straight-line case is relatively symmetric near the LEP and REP, with no pronounced asymmetries or distortions. This further confirms the uniform inflow condition.

In the cornering normal configuration (Figure 3.5b), the overall velocity distribution remains similar to the straight-line case. However, a region of increased velocity magnitude is observed near the REP, in agreement with the expected flow curvature caused by the rotational frame as described in Figure 2.5.

The cornering yaw case (Figure 3.5c) presents a markedly different flow behavior. Notably, regions of high velocity appear near the Right Endplate Outer Face (REOF), while a sharp drop is observed near the Left Endplate Inner Face (LEIF). This spatial velocity variation across the span suggests enhanced vortex stretching or possible vortex breakdown due to the yaw-induced asymmetry.

Furthermore, high-velocity gradients are observed at the lower regions of the endplates, motivating further investigation. Therefore, a top-view velocity field is examined at a streamwise plane located 0.02 m below the aerodynamic center, C^*. The corresponding relative velocity magnitude, $v_{r_{mag}}$, is presented in Figure 3.6.

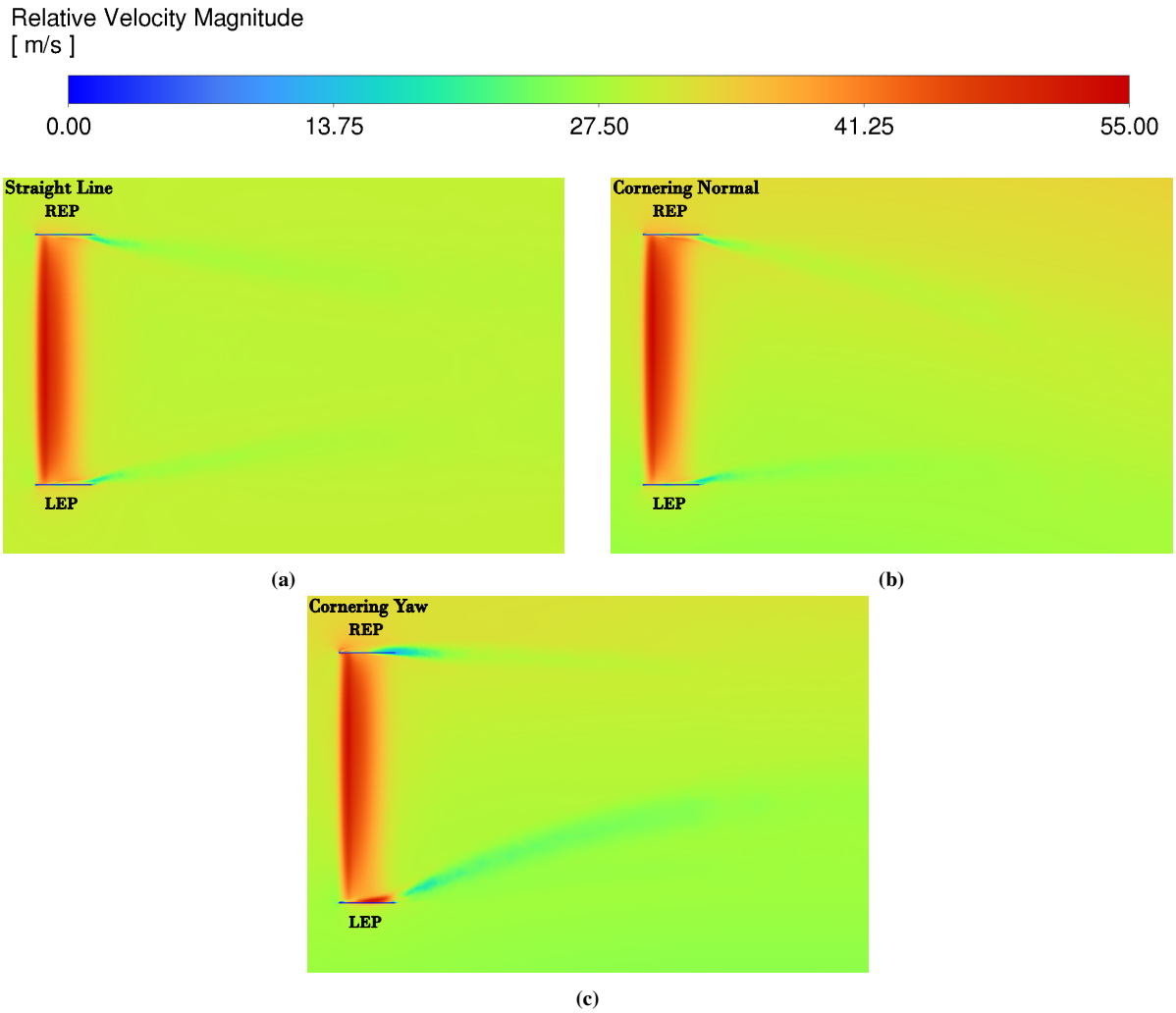

Figure 3.6: Velocity magnitude in the relative frame, $v_{r_{mag}}$ in the horizontal plane located 0.02 m below the aerodynamic center of the airfoil. LEP and REP denote the Left and Right EndPlate, respectively (a) Straight Line, (b) Cornering Normal, (c) Cornering Yaw

From Figure 3.6, it is evident that the velocity magnitude downstream of the airfoil exhibits distinct characteristics for each flow condition. In the straight-line case, the velocity distribution remains symmetric about the centerline, indicating balanced flow behavior across both endplates. In contrast, for the cornering normal and cornering yaw scenarios, the symmetry is lost due to the induced rotational effects. Particularly for the cornering yaw case, a localized region of elevated velocity is observed at the LEIS, as shown in Figure 3.6c. This asymmetry reflects the altered inflow conditions and pressure distribution arising from the vehicle's yawed motion.

The disparity in flow behavior between the left and right endplates becomes pronounced during cornering. Specifically, in both cornering scenarios, the REP consistently experiences higher velocity magnitudes than the LEP, as shown in Figure 3.6b and Figure 3.6c, respectively.

Given the evident shear and rotational flow structures near the endplates particularly at the LEIS and REOS, the observed velocity gradients suggest the generation of vortical structures. To better characterize these phenomena, we proceed to analyze the vorticity magnitude, ω_{mag}. The vorticity magnitude is defined as follows:

$$
\begin{aligned}
\vec{\omega} &= \nabla \times \vec{u} \\
\omega_{mag} &= |\vec{\omega}| = \sqrt{\omega_x^2 + \omega_y^2 + \omega_z^2} \\
\omega_x &= \frac{\partial w}{\partial y} - \frac{\partial v}{\partial z} \\
\omega_y &= \frac{\partial u}{\partial z} - \frac{\partial w}{\partial x} \\
\omega_z &= \frac{\partial v}{\partial x} - \frac{\partial u}{\partial y}
\end{aligned}
\tag{3.4}
$$

Here, $\vec{u}$ represents the velocity vector field, and ω_x, ω_y, and ω_z denote the components of the vorticity vector $\vec{\omega}$ in the x, y, and z directions, respectively. The velocity components in these directions are u, v, and w, while the spatial derivatives are denoted by $\frac{\partial}{\partial x}$, $\frac{\partial}{\partial y}$, and $\frac{\partial}{\partial z}$.

To capture the vorticity dynamics, we focus on the vertical plane located at the trailing edge of the airfoil. This corresponds to the same cross-section in which the velocity distributions were previously examined, as shown in Figure 3.4. Since velocity gradients are strongest in this plane, it is expected that vorticity generation would also be most prominent here.

Accordingly, the vorticity magnitude is evaluated at a distance of $1c$ downstream from the leading edge, as depicted in Figure 3.7. The vorticity distribution for the straight-line and normal cornering cases appears relatively comparable. As shown in Figure 3.7a, the straight-line configuration exhibits a symmetric vorticity pattern on both sides of the wing, consistent with observations in previous studies [Flight Study, 2024].

In the case of normal cornering (Figure 3.7b), the vorticity remains largely symmetric, although slightly stronger structures are seen on the REP side. This is attributed to the velocity differential caused by the curved path—where the REP side experiences higher relative velocity than the LEP side.

In contrast, the cornering with yaw case (Figure 3.7c) displays a markedly asymmetric vorticity distribution. Due to the yaw-induced flow direction, the incoming airflow impacts the endplates at an angle, rather than orthogonally. This results in skewed vorticity structures, with intensified rotational flow near the LEP and REP edges. Notably, in the wake region, the vorticity is predominantly shifted toward the REP side unlike the more balanced distribution observed in the other two configurations.

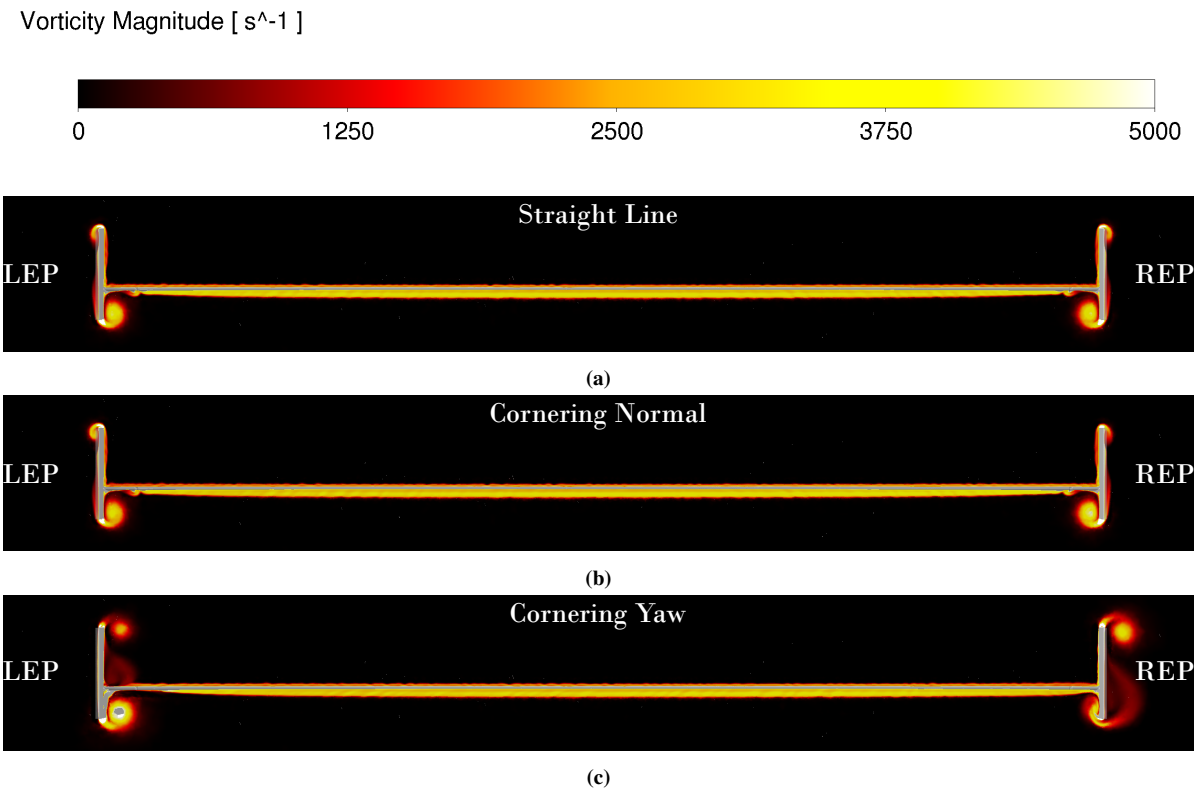

Figure 3.7: Vorticity magnitude in the vertical plane located one chord length downstream of the airfoil, where LEP and REP denote the Left and Right EndPlate, respectively (a) Straight Line, (b) Cornering Normal, (c) Cornering Yaw.

To understand the evolution and convection of vortices behind the airfoil, the vorticity magnitude is visualized in a horizontal plane located 0.02m below the aerodynamic center of the airfoil, viewed from the top, as shown in Figure 3.8. From the figure, it can be seen that in both the straight-line and normal cornering cases, the vortex structures grow symmetrically downstream. However, in the cornering with yaw case, the vorticity persists longer on the LEP side compared to the REP side of the airfoil.

In Figure 3.8b, corresponding to normal cornering, the vortices display slight curvature relative to the straight-line case shown in Figure 3.8a. In contrast, the flow structure in the cornering with yaw case, shown in Figure 3.8c, is significantly different. Here, the vorticity on the REP side dissipates more rapidly, while on the LEP side, the vorticity magnitude decays more slowly and follows a path with a larger radius of curvature compared to the normal cornering case.

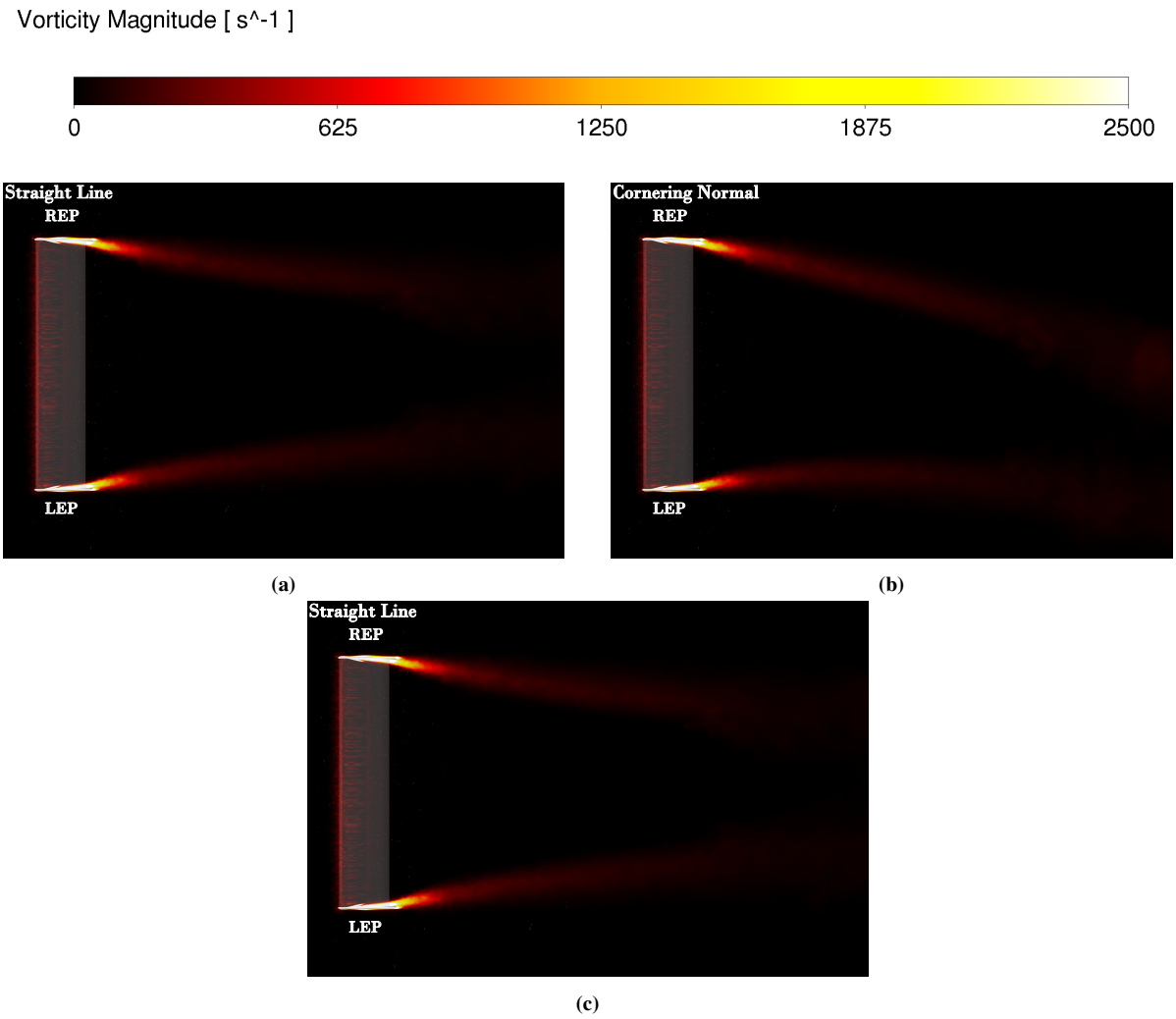

Figure 3.8: Vorticity magnitude in the horizontal plane located 0.02 m below the aerodynamic center of the airfoil, where LEP and REP denote the Left and Right EndPlate, respectively (a) Straight Line (b) Cornering Normal (c) Cornering Yaw

The vorticity structures have been thoroughly analyzed across multiple planes as discussed above. While vortices near the endplates have been well documented, Figure 3.5 highlights the presence of a low-velocity zone on the airfoil, which coincides with regions of high vorticity magnitude observed in Figure 3.7. However, the velocity and vorticity magnitude plots alone do not provide sufficient insight into the nature of the flow in these regions. To investigate whether turbulence is being generated, the Turbulent Viscosity Ratio (TVR) is studied. This parameter quantifies the relative importance of turbulent transport compared to molecular diffusion.

The Turbulent Viscosity Ratio is defined in Equation 3.5, where μ_t is the turbulent viscosity (defined in Equation 3.6) and μ is the laminar viscosity, which for air is approximately $\mu \approx 1.8 \times 10^{-5}$ kg/m·s.

$$TVR = \frac{\mu_t}{\mu} \tag{3.5}$$

$$\mu_{\mathrm{T}} = \frac{\rho a_1 k}{\max\left(a_1 \omega, S f_{v2}\right)} \tag{3.6}$$

where ρ is the fluid density, a_1 is the Bradshaw constant, k is the turbulent kinetic energy, ω is the specific dissipation rate ($\omega = \frac{\epsilon}{k}$), S is the characteristic magnitude of the mean velocity gradients, and f_{v2} is an interpolation function [DMS, 2025; NASA, 2025].

The ranges of TVR corresponding to different flow regimes are summarized in Table 3.2.

Table 3.2: Ranges of Turbulent Viscosity Ratio (TVR) and their corresponding Flow Regimes in CFD Simulation [DMS, 2025]

Turbulent Viscosity Ratio (TVR) Value	**Region**
0 – 1	Laminar zones
1 – 10	Transitional flow
10 – 100	Fully turbulent Zones
100 – 1000	Strong turbulence zones

Using this classification, the TVR was evaluated in a horizontal plane located 0.02 m below the leading edge, as shown in Figure 3.9. As anticipated and discussed previously, high TVR values are observed near the endplates and downstream of them, indicating strong turbulence, consistent with the vorticity magnitude trends in Figure 3.8. However, a notable feature emerges directly behind the airfoil. Initially, $TVR \approx 0$, indicating laminar flow, but further downstream, the ratio increases gradually, transitioning through the laminar, transitional, and eventually fully turbulent regimes, as defined in Table 3.2. This confirms the development of turbulence in the wake of the airfoil, particularly pronounced near the endplates. The elevated turbulence levels behind the endplates arise due to the interaction between vortical structures shed from the pressure and suction surfaces, leading to increased shear layer instabilities.

The turbulence in the central wake region originates from the mixing of flows from the suction and pressure sides of the airfoil, which have different velocities and directions. This mixing creates a shear layer that becomes unstable over a short distance behind the trailing edge, eventually breaking down into small-scale turbulent structures. This gradual transition is visible in the TVR distribution and marks the onset of unsteady wake behavior, which is critical for understanding aerodynamic drag and flow-induced vibrations.

In the cornering yaw configuration (Figure 3.9c), a region of extremely high $TVR \approx 400$ is observed near the Right Endplate Outer Surface (REOS), indicating strong turbulence that gradually dissipates downstream. Simultaneously, the Left Endplate Inner Surface (LEOS) shows increased TVR compared to both the cornering normal and straight-line configurations. These observations suggest that cornering yaw induces significantly more turbulence than the other two cases. This has major implications for downstream flow conditions, especially when analyzing the aerodynamics of the full vehicle, as yaw-induced turbulence can alter pressure fields, wake behavior, and downstream aerodynamic loads.

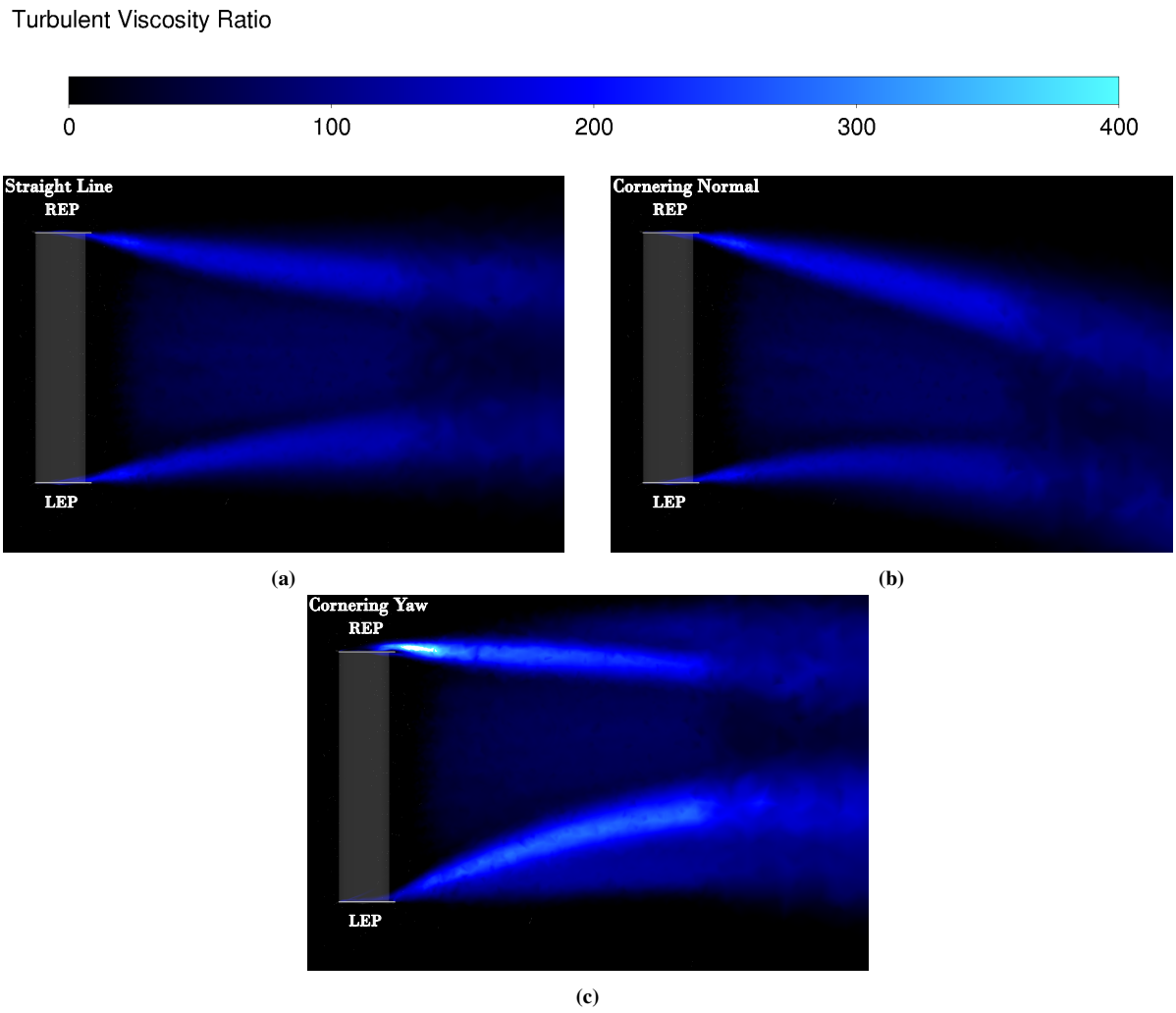

Figure 3.9: Turbulent Viscosity Ratio (TVR) in the horizontal plane located 0.02 m below the aerodynamic center of the airfoil, where LEP and REP denote the Left and Right EndPlate, respectively (a) Straight Line (b) Cornering Normal (c) Cornering Yaw

We now turn our attention to the coefficient of pressure, C_P, on the airfoil. The definition of C_P is provided in Equation 3.7 [AeroTools, n.d.]. In this analysis, we focus on the pressure distribution along the underside of the airfoil, as shown in Figure 3.10.

$$C_P = \frac{P_s - P_\infty}{\frac{1}{2}\rho u_{mean}^2} \tag{3.7}$$

where P_s is the static pressure, P_∞ is the freestream pressure, ρ is the fluid density, and u_{mean} is the mean flow velocity.

A point with $C_P = 1$ corresponds to a stagnation point. When $C_P > 1$, the local velocity is reversed. For $0 < C_P < 1$, the local velocity is less than the mean velocity u_{mean}, and for $C_P < 0$, the local velocity exceeds u_{mean}.

Upon comparing the three flow configurations: Straight Line, Cornering Normal, and Cornering Yaw, it is evident that the minimum C_P region on the airfoil's lower surface shifts slightly towards the Right Endplate Inner Surface (REIS) during cornering. This shift becomes especially pronounced in the Cornering Yaw case, where a significant pressure drop (low C_P) appears near the Left Endplate Inner Surface (LEIS), close to the leading edge. This phenomenon is attributed to the formation of strong vortical structures near the LEP endplate region, which is consistent with the vorticity distributions shown in Figure 3.7 and Figure 3.8.

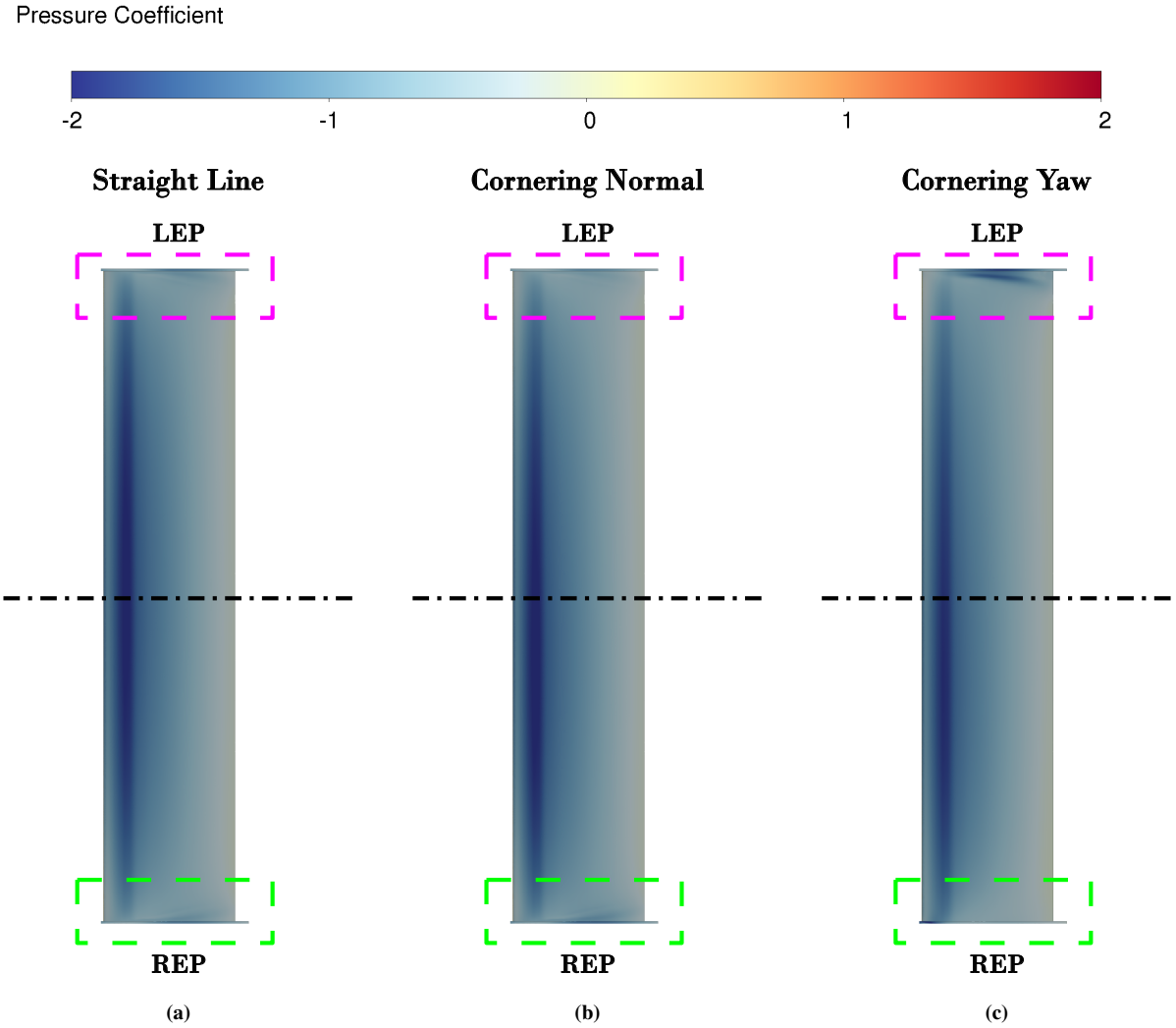

Figure 3.10: Comparison of pressure coefficient, $C_P$aat the suction side of the front wing for all three cases, where LEP stands for Left EndPlate, REP stands for Right EndPlate: Pink square represents the area near the LEP and green square represents the area near the REP (a) Straight Line, (b) Cornering Normal, (c) Cornering Yaw

To further investigate the aerodynamic implications, the pressure coefficient distribution is analyzed at the airfoil's mid-span cross-section. As shown in Figure 3.11, the Straight Line and Cornering Normal configurations exhibit nearly identical C_P distributions along the centerline, which is consistent with their symmetric vortex structures and flow profiles. In contrast, the Cornering Yaw configuration shows a significant asymmetry. The deviation is primarily due to the yaw-induced flow not being aligned with the chordwise direction, resulting in an altered pressure recovery on the surface.

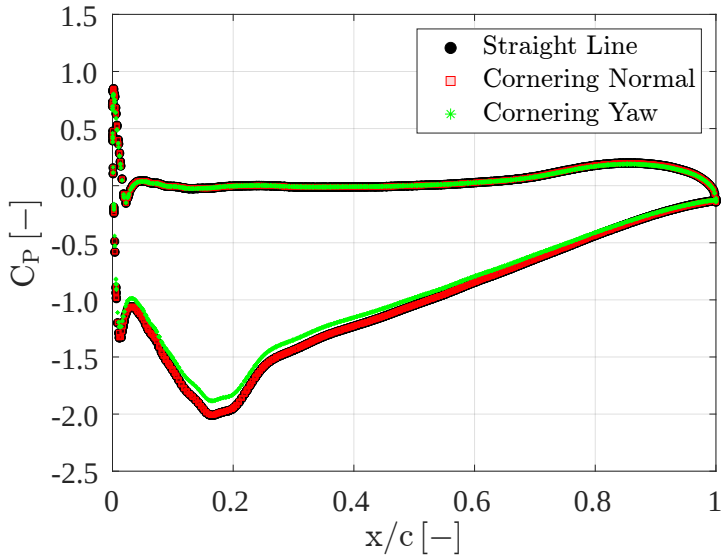

Figure 3.11: Comparison of pressure coefficient, C_P, at the mid-plane cross section of the airfoil side profile for all three cases: Straight Line, Cornering Normal, and Cornering Yaw. Here, $x/c = 0$ and $x/c = 1$ correspond to the leading edge and trailing edge of the airfoil respectively

However, the differences in C_P distributions on the main airfoil surfaces alone cannot fully explain the variations in lateral aerodynamic forces, especially the side force F_S. To explore this further, C_P distributions on the surfaces of the endplates are shown in Figure 3.12. While the Straight Line and Cornering Normal cases demonstrate largely symmetric C_P patterns across all endplate surfaces, the Cornering Yaw case reveals a clear imbalance. Specifically, the REIS and LEOS exhibit higher C_P values, while REOS and LEIS show lower C_P values. This asymmetry contributes significantly to the side force generation in the Cornering Yaw configuration, reinforcing the importance of the endplates in generating lateral aerodynamic loads.

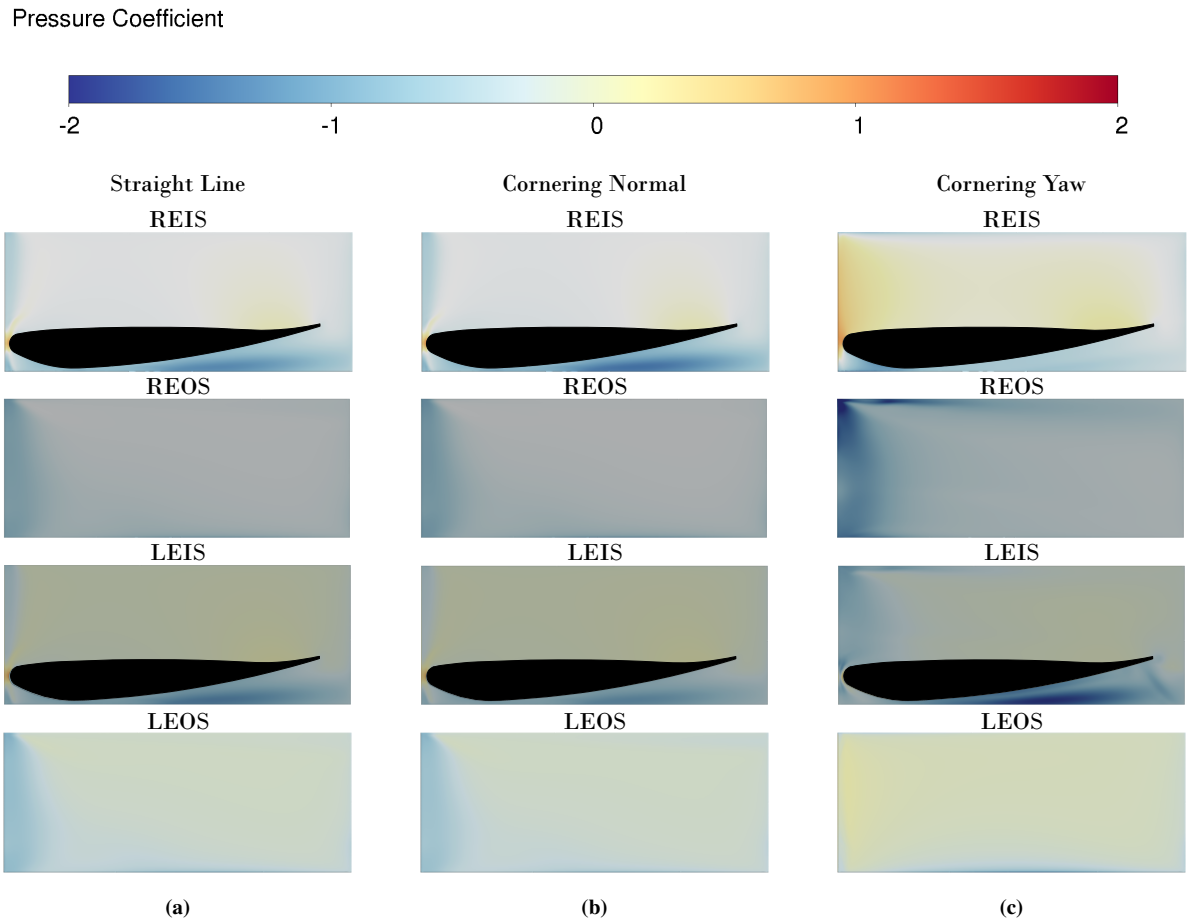

Figure 3.12: Pressure coefficient C_P on the surfaces of the endplates for all three configurations, where REIS is Right Endplate Inner Surface, REOS is Right Endplate Outer Surface, LEIS is Left Endplate Inner Surface and LEOS is Left Endplate Outer Surface (a) Straight Line (b) Cornering Normal (c) Cornering Yaw

In summary, the analysis confirms that the Cornering Yaw configuration provides a more realistic representation of the actual aerodynamic behavior of a Formula 1 car during turning, compared to the idealized Cornering Normal case. This conclusion is consistent with prior literature [BrambleCFD, 2022]. As a result, all further simulations focus exclusively on the Cornering Yaw scenario, which is subsequently compared against the Straight Line configuration in subsubsection 3.2.2.2.

3.2.2.2. Analysis of Transient Aerodynamics in Straight Line and Cornering Yaw Conditions

Straight Line and Cornering Yaw configurations are selected for detailed analysis, as they most closely replicate real-world racing conditions, as discussed earlier. This investigation is conducted using the acceleration and deceleration profiles as shown in Figure 2.7. To ensure a consistent comparison between the straightline and cornering yaw cases, it was confirmed that the velocity magnitude at the midplane of the wing's side profile is identical in both cases. Based on these velocity profiles, the aerodynamic forces, moments, and their corresponding instantaneous coefficients are calculated using Ansys Fluent. The primary focus is on the range $t^* = 0$ to $t^* = 1$, which captures the deceleration and acceleration phases. Additionally, a small window before and after this interval is examined to assess the steady-state behavior and its influence on the transient flow response.

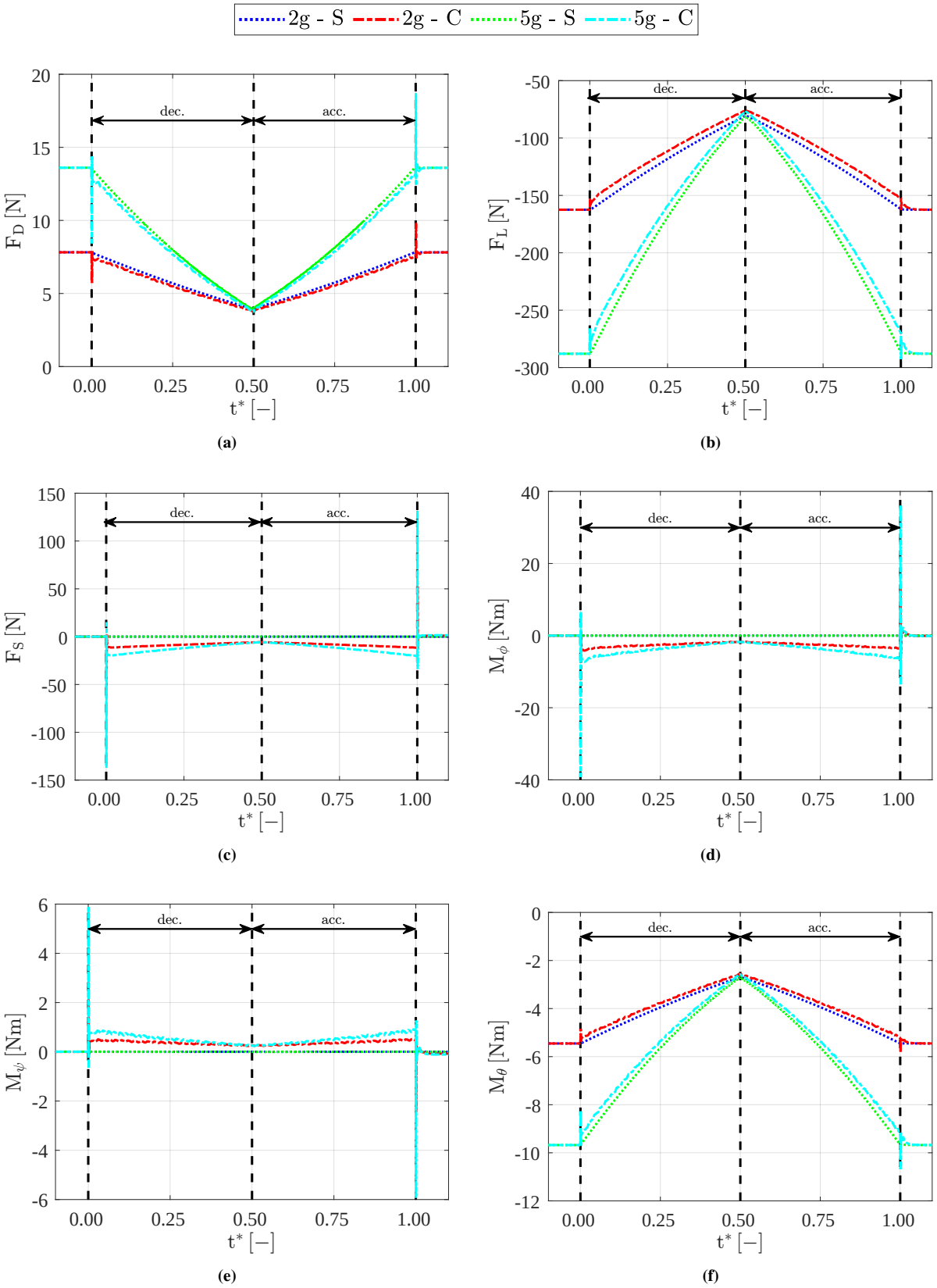

Figure 3.13: Force and moment results plotted against non-dimensionalized time, t^* (Equation 2.22), where S represents Straight Line, C represents Cornering, and the black vertical lines indicate the transition between different simulation phases: dec. refers to deceleration and acc. refers to acceleration: (a) Drag Force, F_D, (b) Lift Force, F_L, (c) Side Force, F_S, (d) Rolling Moment, M_ϕ, (e) Yawing Moment, M_ψ, (f) Pitching Moment, M_θ

Figure 3.13 presents the aerodynamic forces and moments acting on the airfoil, with the directions of these forces illustrated in Figure 2.2d. Noticeable peaks in the force and moment values are observed at the start of deceleration ($t^* \approx 0$) and at the end of acceleration ($t^* \approx 1$), which are primarily attributed to the combined effect of added mass and jerk, resulting from the sudden change in linear acceleration, a, for the straight-line case, and in angular velocity, ω, and angular acceleration, α, for the cornering case.

It is observed that the peak magnitudes near $t^* = 0$ and $t^* = 1$ are more significant for F_D, F_S, M_ϕ, and M_ψ compared to F_L and M_θ. This behavior arises from the abrupt changes in acceleration, as evident in the acceleration profiles (Figure 2.7), which induce large inertial responses. Similar peaks have also been reported in previous studies [Pathanadka, 2022]. These occur due to the non-zero time derivative of acceleration (jerk) when acceleration starts or ends suddenly, causing a sharp gradient in force. This change in the forces and moments is discussed in detail below.

3.2.2.2.1 Analysis of Initial Peak Forces and Moments To investigate the initial peaks in the force and moment values, we focus on the start of deceleration, i.e., at $t^* = 0.0$ which corresponds to $t = 0.5$ s in normal time. The analysis considers both straight-line and cornering scenarios for the $5g$ acceleration case. Since the time step was $\Delta t = 0.0005$ s, we examine the values from $t = 0.498$ s to $t = 0.504$ s, as shown in Figure 3.14.

The major differences occur at flow time of $t = 0.5000$ s, $t = 0.5005$ s, and $t = 0.5010$ s. While the changes in aerodynamic forces and moments are relatively minor for the straight-line case, they are considerably more pronounced during cornering.

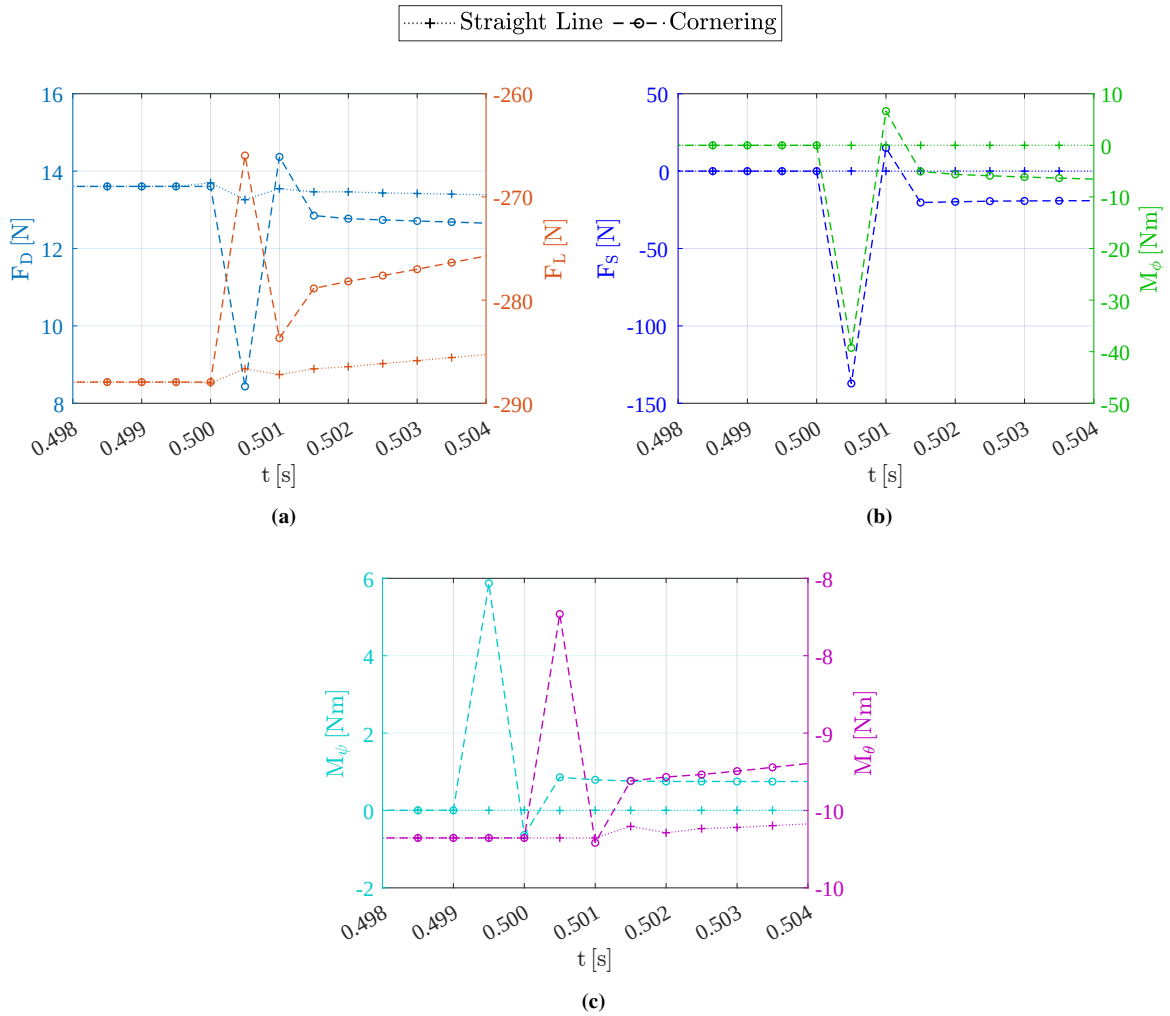

Figure 3.14: Aerodynamic Force and Moments versus flow time, t, between $t = 0.498$ and $t = 0.504$(a) Drag Force, $F_{D_{ins}}$ and Lift Force, $F_{L_{ins}}$ (b) Side Force, $F_{S_{ins}}$ and Rolling Moment, $M_{\phi_{ins}}$ (c) Yawing Moment, $M_{\psi_{ins}}$ and Pitching Moment, $M_{\theta_{ins}}$

Identifying the presence of peaks is useful; however, it is equally important to quantify the change. This is done by comparing the aerodynamic forces and moments at the start of deceleration ($t = 0.5005$ s and $t = 0.5010$ s) with their reference values just before deceleration begins ($t = 0.5000$ s). The corresponding percentage changes are shown in Table 3.3, calculated using Equation 3.8:

$$\% \text{ Change} = \frac{y - x}{x} \times 100 \tag{3.8}$$

Here, y represents the aerodynamic force or moment at the time of interest ($t = 0.5005$ s or $t = 0.5010$ s), and x is the reference value at $t = 0.5000$ s.

Table 3.3: Aerodynamic force and moment components with corresponding percentage changes relative to $t = 0.5000\,\text{s}$

Aerodynamic Force						
Flow Time t [s]	Drag Force F_D [N]	% Change [-]	Lift Force F_L [N]	% Change [-]	Side Force F_S [N]	% Change [-]
0.5000	13.605	-	−287.946	-	−0.008	-
0.5005	8.434	38.005	−265.990	7.625	−137.232	1744696.607
0.5010	14.367	5.602	−283.676	1.483	14.983	190594.185

Aerodynamic Moment						
Flow Time t [s]	Rolling Moment M_ϕ [Nm]	% Change [-]	Yawing Moment M_ψ [Nm]	% Change [-]	Pitching Moment M_θ [Nm]	% Change [-]
0.5000	−0.001	-	0.004	-	−9.677	-
0.5005	−39.264	3702421.900	5.873	135082.100	−8.231	14.945
0.5010	6.633	625613.834	−0.634	14699.529	−9.709	0.326

From Table 3.3, it is observed that at the onset of cornering i.e., at $t = 0.5005\,\text{s}$ there is a significant deviation in the aerodynamic forces and moments compared to the previous time step ($t = 0.5000\,\text{s}$), which marks the end of the straight-line phase. A sharp increase in both magnitudes and percentage differences (see Equation 3.8) indicates the presence of an instantaneous peak, which subsequently begins to decay.

For the drag force F_D, a reduction of approximately 5 N is observed, corresponding to a 38% decrease. In contrast, the lift force F_L changes by around 22 N, translating to a 7.6% increase. However, the most dramatic change is seen in the side force F_S, which increases by roughly 137 N. Due to the near-zero reference value, this results in an enormous percentage change on the order of 1.7×10^6%, indicating a sudden surge in lateral aerodynamic loading.

Similarly, the aerodynamic moments particularly the rolling moment M_ϕ and yawing moment M_ψ exhibits large deviations. M_ϕ undergoes a jump of approximately 39 Nm, resulting in a percentage change of 3.7×10^6%. M_ψ increases by about 5.8 Nm, leading to a change of 1.3×10^5%. In contrast, the pitching moment M_θ changes relatively little, with a difference of 1.45 Nm and a corresponding 14.9% variation.

Since the aerodynamic moments are directly influenced by the distribution and magnitude of aerodynamic forces, it becomes essential to investigate the underlying causes of these changes. To this end, the pressure coefficient distribution C_P across various surfaces of the front wing is examined in Figure 3.15.

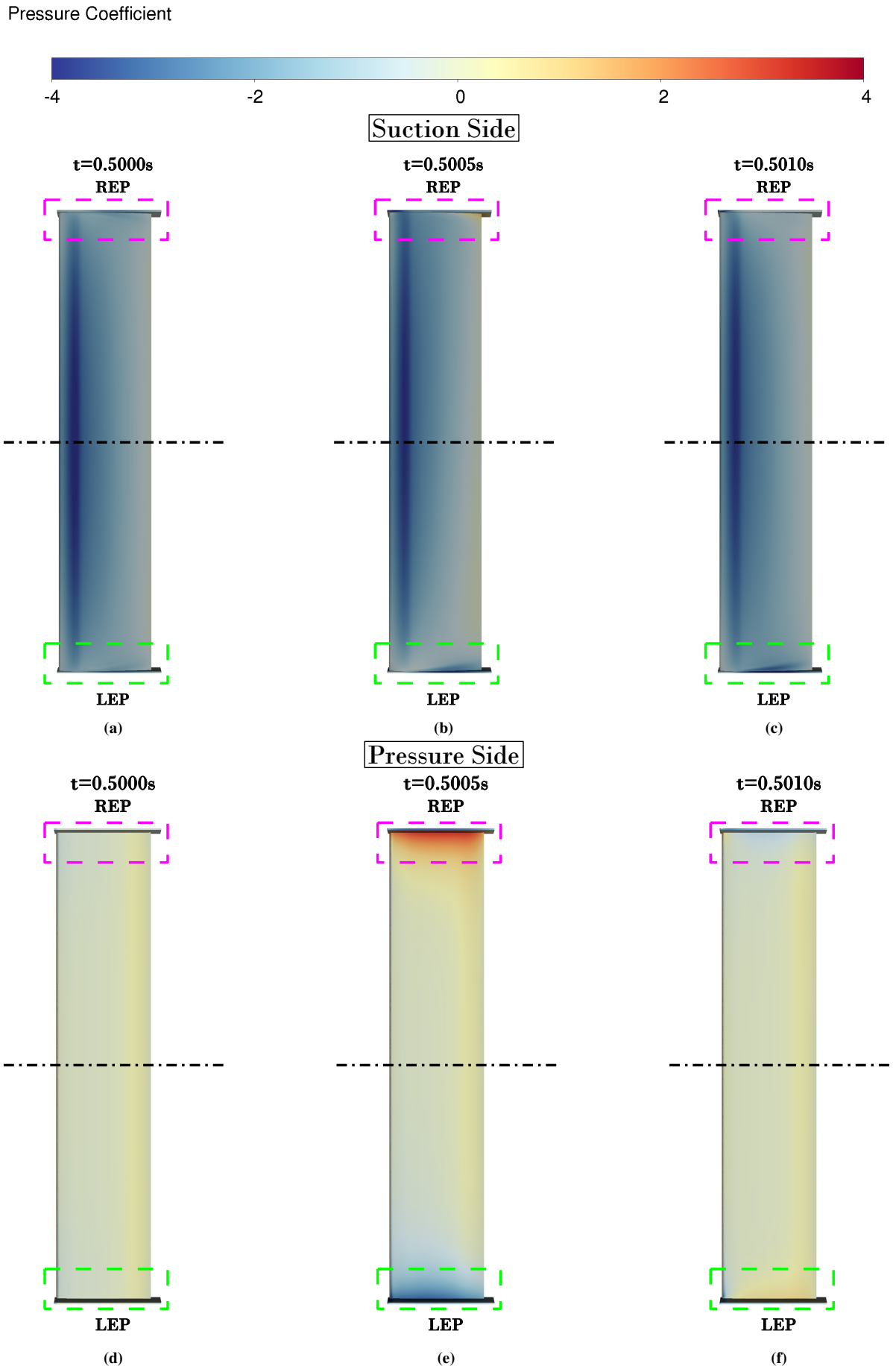

Figure 3.15: Coefficient of pressure, C_P, on the suction and pressure sides of the front wing at three time instances. REP denotes the Right Endplate, and LEP the Left Endplate. The pink rectangle highlights the region near the LEP, and the green rectangle highlights the region near the REP. (a–c) Suction side at $t = 0.5000$ s, 0.5005 s, and 0.5010 s respectively (d–f) Pressure side at $t = 0.5000$ s, 0.5005 s, and 0.5010 s respectively

From Figure 3.15, it is observed that across all three flow times, there is no significant change in the pressure distribution on the suction side of the front wing, except for two notable features: (i) a shift in C_P values towards the REP, and (ii) the appearance of a low C_P region near the LEP at $t = 0.5005$ s and $t = 0.5010$ s. This behavior has been discussed in detail in subsubsection 3.2.2.1.

In contrast, on the pressure side, a large C_P region is observed near the REP at $t = 0.5005$ s, along with a corresponding low C_P region near the LEP. By $t = 0.5010$ s, the C_P distribution closely resembles that at $t = 0.5000$ s, except for a slightly lower C_P near the REP.

Given these evolving differences at the LEP and REP, we now focus on examining the C_P distribution specifically at the endplate surfaces to better understand their aerodynamic effects, as shown in Figure 3.16.

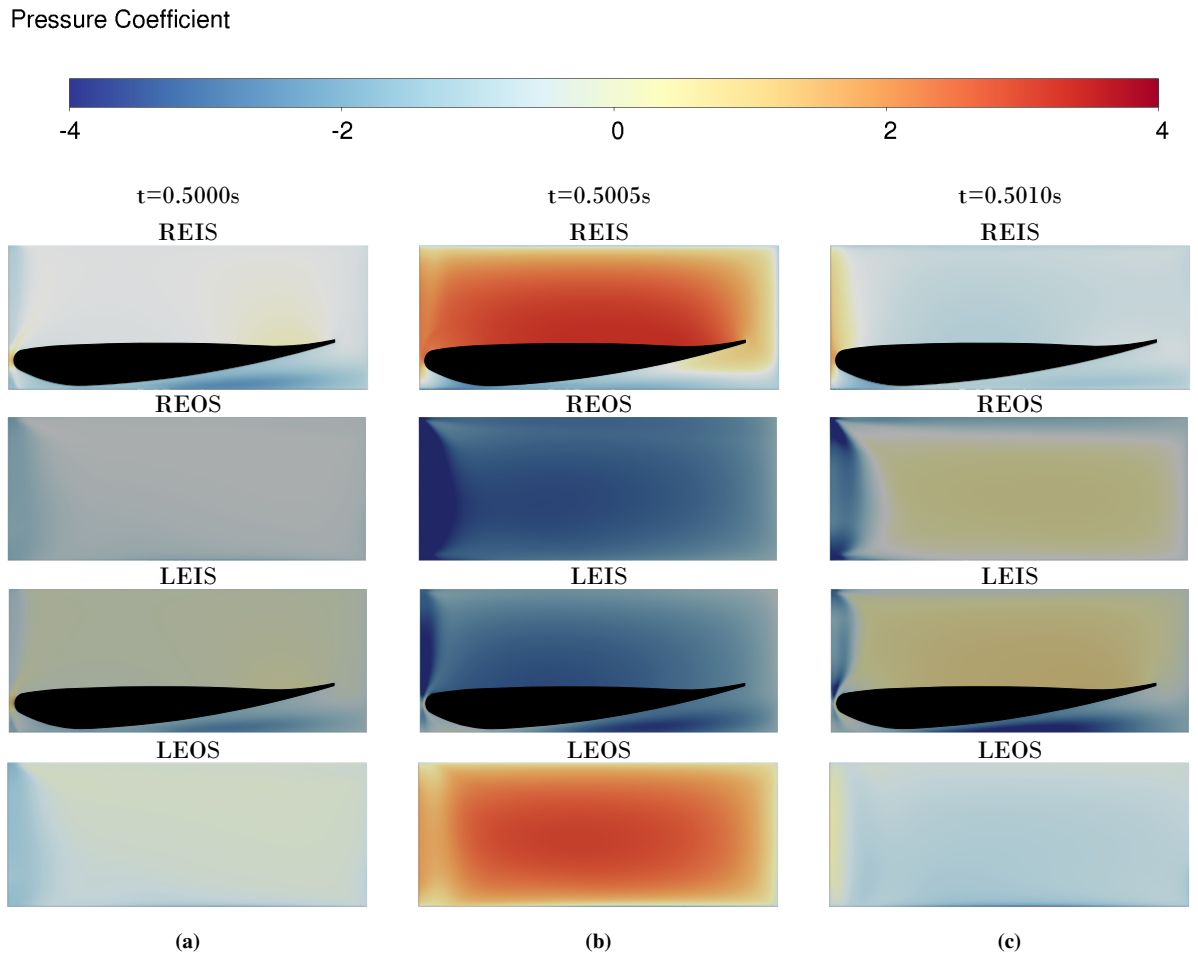

Figure 3.16: Pressure coefficient, C_P, on the surfaces of the endplates at three different times. REIS: Right Endplate Inner Surface, REOS: Right Endplate Outer Surface, LEIS: Left Endplate Inner Surface, and LEOS: Left Endplate Outer Surface. (a) $t = 0.5000$ s, (b) $t = 0.5005$ s, (c) $t = 0.5010$ s

From Figure 3.16, it is observed that at $t = 0.5005$ s, compared to $t = 0.5000$ s, there is a significant increase in C_P at REIS and LEOS, and a corresponding drop in C_P at REOS and LEIS. When comparing $t = 0.5000$ s with $t = 0.5010$ s, the differences are not as significant as in the comparison between $t = 0.5005$ s and $t = 0.5000$ s: C_P at REIS and LEOS is slightly lower, while it is slightly higher at REOS and LEIS.

From Figure 3.15 and Figure 3.16, the differences in aerodynamic forces and moments observed in Table 3.3 can be explained by examining the Coefficient of Pressure, C_P, distribution on the front wing. The peak in pressure observed at $t = 0.5005$ s compared to $t = 0.5000$ s during the onset of deceleration can be attributed to a combination of factors:

- Sudden transition from straight-line to cornering motion, with a sudden onset of angular velocity and angular acceleration, as shown in Figure 2.7. From $t = 0.0000$ s to $t = 0.5000$ s, the path is a straight line ($R \approx \infty$), whereas at $t = 0.5005$ s, the cornering starts and the radius of the turn becomes $R = 8$ m, as seen in Figure 2.6.
- The effect of sudden deceleration and acceleration, transitioning from 0 m/s^2 to the required linear acceleration and angular acceleration values.

To gain deeper insight into these effects, the coefficients of forces and moments are evaluated, as using coefficients provides a more universal basis for comparison than raw force values. This approach also facilitates comparison with results from other studies. The differences between transient and steady-state conditions are examined by comparing the coefficients of the instantaneous aerodynamic forces and moments, as defined in Equation 3.9 and Equation 3.10:

$$C_{F_{ins}} = \frac{2 \times F}{\rho V(t)^2 A} \tag{3.9}$$

$$C_{M_{ins}} = \frac{2 \times M}{\rho V(t)^2 A l} \tag{3.10}$$

When visualizing the aerodynamic coefficients, noticeable vibrations and fluctuations were observed. These are primarily attributed to vortex shedding near the endplates, as supported by previous studies [Pathanadka, 2022; Zhou, 2023], and are further discussed in subsubsection 3.2.2.3 and subsubsection 3.2.2.4. To better interpret the underlying trends in the data without the influence of high-frequency fluctuations, a second-order Savitzky-Golay filter, SG filter with a filter width of $t = 0.1$ s of the flow time, is applied. This allows simultaneous visualization of both the raw and smoothed coefficient data.

To further analyze the effects of acceleration and deceleration, steady-state forces and moments computed without any acceleration are determined at discrete normalized time instances, $t^* = 0, 0.1, 0.2, \ldots, 1.0$. The corresponding aerodynamic force and moment coefficients are calculated using Equation 3.2 and Equation 3.3. These steady-state coefficients, along with the transient and filtered data, are presented in Figure 3.17 and Figure 3.18.

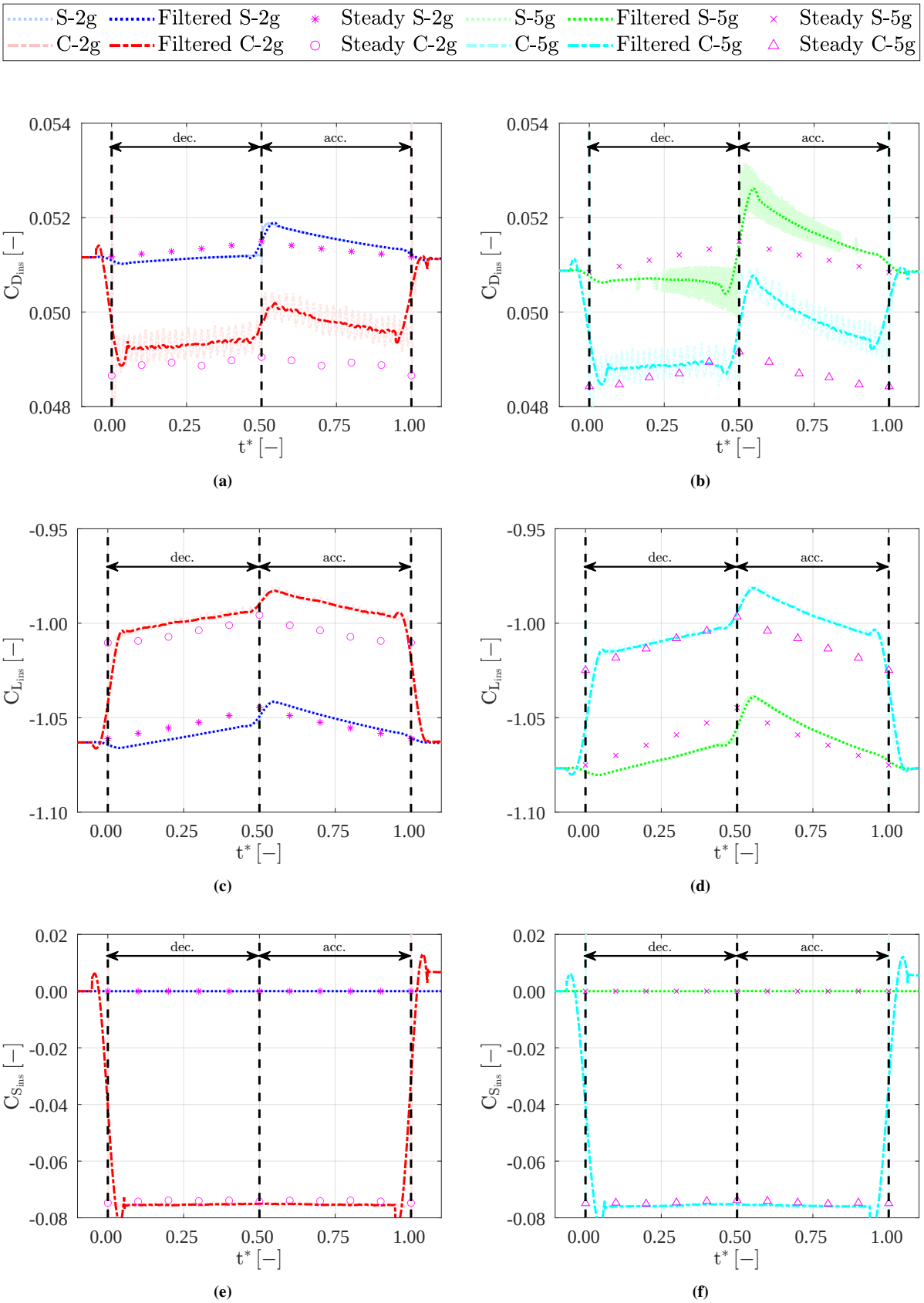

Figure 3.17: Instantaneous Coefficient of Force comparing transient and steady-state data versus nondimensional time t^* (Equation 2.22), where S denotes Straight Line and C denotes Cornering. The semi-transparent lines represent the original data, solid lines are the filtered data, pink points indicate steady-state values, and black vertical lines mark different simulation phases: dec. refers to deceleration and acc. refers to acceleration: (a) Instantaneous Coefficient of Drag force for $2g$ S and $2g$ C (b) Instantaneous Coefficient of Drag force for $5g$ S and $5g$ C (c) Instantaneous Coefficient of Lift force for $2g$ S and $2g$ C (d) Instantaneous Coefficient of Lift force for $5g$ S and $5g$ C (e) Instantaneous Coefficient of Side force for $2g$ S and $2g$ C (f) Instantaneous Coefficient of Side force for $5g$ S and $5g$ C

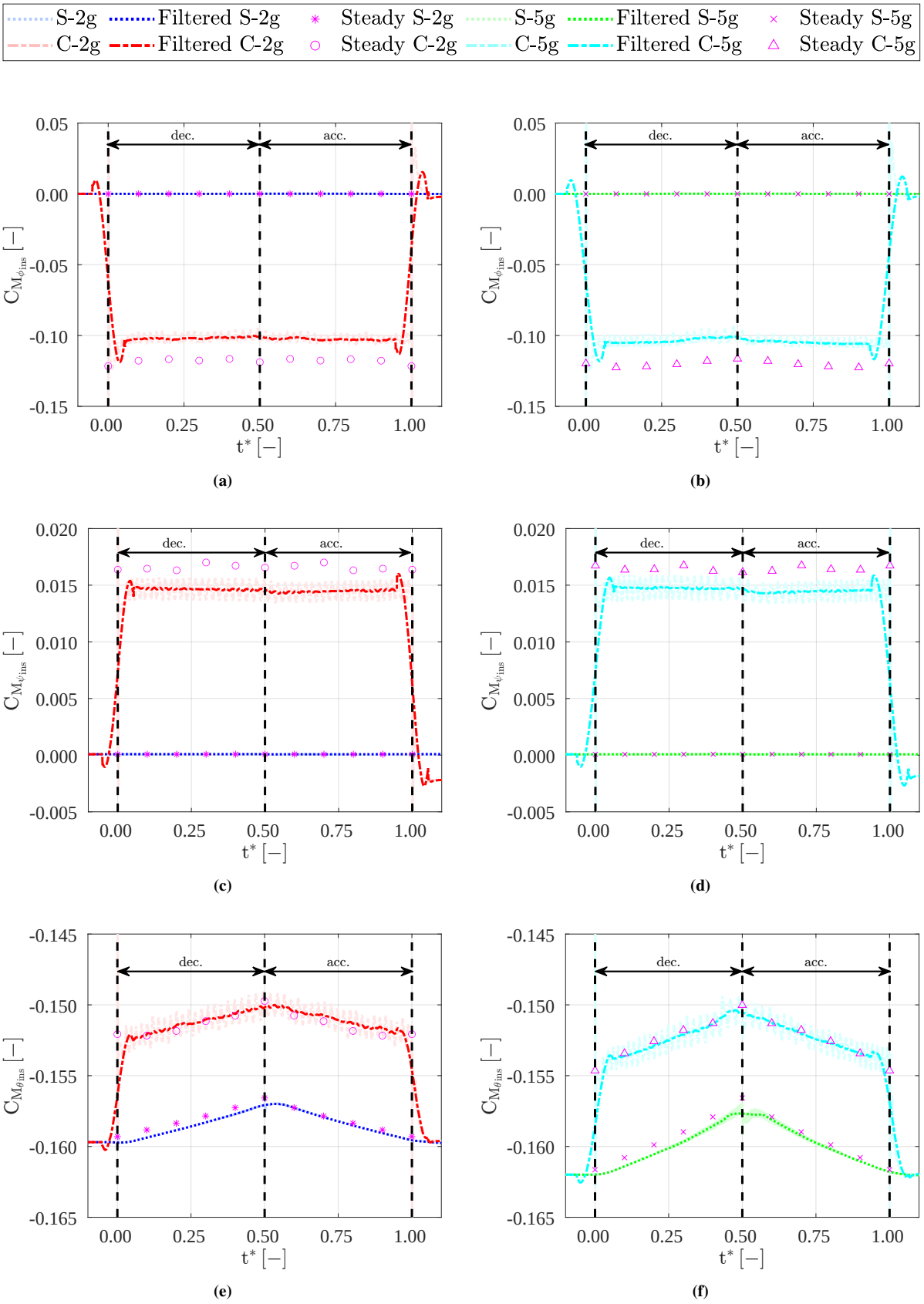

Figure 3.18: Instantaneous coefficient of Moment comparing transient and steady-state data versus nondimensional time t^* (Equation 2.22), where S denotes Straight Line and C denotes Cornering. The semi-transparent lines represent the original data, solid lines are the filtered data, pink points indicate steady-state values, and black vertical lines mark different simulation phases: dec. refers to deceleration and acc. refers to acceleration: (a) Instantaneous Coefficient of Rolling Moment for $2g$ S and $2g$ C (b) Instantaneous Coefficient of Rolling Moment for $5g$ S and $5g$ C (c) Instantaneous Coefficient of Yawing Moment for $2g$ S and $2g$ C (d) Instantaneous Coefficient of Yawing Moment for $5g$ S and $5g$ C (e) Instantaneous Coefficient of Pitching Moment for $2g$ S and 4 C (f) Instantaneous Coefficient of Pitching Moment for $5g$ S and $5g$ C

Firstly, the instantaneous coefficients of aerodynamic forces are shown in Figure 3.17. For $C_{D_{ins}}$ and $C_{L_{ins}}$, both exhibit similar trends. In the straight-line case, it is observed that during deceleration, the steady-state values are higher than the transient data, while during the acceleration phase, the transient values exceed the steady-state values. In contrast, for the cornering case, the steady-state values are consistently lower than the transient data across both deceleration and acceleration phases, with a more significant difference in magnitude during the acceleration phase. When comparing cornering to the straight-line case, $C_{D_{ins}}$ and $C_{L_{ins}}$ are lower in magnitude for the cornering case during both phases. The key difference between the $2g$ and $5g$ profiles is the increased magnitude of the transient to steady-state shift at the transition point ($t^* \approx 0.5$) for the $5g$ case, indicating a higher gradient in acceleration. Additionally, during deceleration, $C_{D_{ins}}$ increases as the velocity decreases, while $C_{L_{ins}}$ shows an overall reduction in magnitude with decreasing velocity, confirming the velocity dependence of both coefficients.

For $C_{S_{ins}}$, in the straight-line case, the coefficient remains approximately zero for both transient and steady-state data. In the cornering case, the magnitude of $C_{S_{ins}}$ is non-zero but remains relatively unchanged across both data sets. Furthermore, $C_{S_{ins}}$ does not vary significantly with velocity, indicating insensitivity to changes in flow speed.

Regarding moment coefficients, for the straight-line case, $C_{M_{\phi_{ins}}}$ and $C_{M_{\psi_{ins}}}$ remain nearly zero, with good agreement between transient and steady-state data. For $C_{M_{\theta_{ins}}}$, the magnitude decreases with decreasing velocity. When compared to steady-state results, both deceleration and acceleration phases show slightly lower steady-state magnitudes than transient ones.

In the cornering case, the moment coefficients differ considerably from the straight-line condition. $C_{M_{\phi_{ins}}}$ exhibits a negative magnitude, with steady-state values higher than the transient data. For $C_{M_{\psi_{ins}}}$, non-zero magnitudes are observed, and again the steady-state values are larger. The unfiltered transient data for $C_{M_{\psi_{ins}}}$ shows notable fluctuations with velocity due to vortex shedding; however, the filtered data reveals minimal variation with velocity. $C_{M_{\theta_{ins}}}$ follows a similar trend to the straight-line case, though with lower magnitudes, and the steady-state and transient values remain closely aligned.

From a racing dynamics perspective, the transition from straight-line motion to cornering results in substantial variations in aerodynamic forces and moments. This aerodynamic instability contributes significantly to the difficulty drivers experience when executing high-speed sharp turns. A pronounced peak in force values was also observed during this transition phase. Notably, the magnitude of drag and lift coefficient was consistently lower during deceleration and higher during acceleration, a difference primarily attributed to the surrounding fluid acceleration/deceleration and added mass effects. Recognizing and optimizing for this disparity can yield performance gains, potentially saving critical milliseconds in competitive racing. Moreover, the increasing velocity amplifies this drag coefficient difference, underscoring the need for precise aerodynamic tuning during transient driving conditions.

Understanding the differences between steady-state (no acceleration or deceleration) and transient aerodynamic data (during acceleration and deceleration phases) is essential for evaluating unsteady aerodynamic effects. This comparison is presented in Table 3.4, which reports results at different t^* values for the $2g$ straight-line case.

The analysis focuses on aerodynamic forces rather than moments, as Figure 3.14 shows negligible variation in moments for the straight-line case, whereas forces exhibit noticeable changes. These force differences arise from two main factors: (i) flow history effects, which capture the influence of prior flow states on the current aerodynamic response, and (ii) added mass, the additional force experienced by the body due to the inertia of the surrounding fluid during acceleration or deceleration.

Table 3.4: Transient and steady-state aerodynamic forces at various time instances with corresponding flow velocities for the 2g acceleration straight-line case

Velocity [m/s]	Force	Transient [N]	Steady State [N]	Difference (Transient - Steady State) [N]
Deceleration				
		$t^* = 0.1$		
30.018	F_D	6.919	6.942	-0.023
	F_L	-144.226	-143.397	-0.829
	F_S	-0.006	-0.005	-0.001
		$t^* = 0.2$		
28.156	F_D	6.093	6.114	-0.021
	F_L	-126.563	-125.826	-0.737
	F_S	-0.006	-0.004	-0.002
		$t^* = 0.3$		
26.294	F_D	5.319	5.338	-0.019
	F_L	-110.088	-109.418	-0.670
	F_S	-0.003	-0.004	0.001
		$t^* = 0.4$		
24.432	F_D	4.595	4.615	-0.020
	F_L	-94.788	-94.152	-0.637
	F_S	-0.0043	-0.0036	-0.0007
Acceleration				
		$t^* = 0.6$		
24.432	F_D	4.646	4.615	0.031
	F_L	-93.698	-94.152	0.454
	F_S	-0.0036	-0.0037	0.0001
		$t^* = 0.7$		
26.294	F_D	5.366	5.338	0.028
	F_L	-108.998	-109.418	0.420
	F_S	-0.0025	-0.0038	0.0013
		$t^* = 0.8$		
28.156	F_D	6.139	6.114	0.025
	F_L	-125.468	-125.826	0.358
	F_S	-0.0039	-0.0040	0.0001
		$t^* = 0.9$		
30.018	F_D	6.962	6.942	0.020
	F_L	-143.111	-143.397	0.286
	F_S	-0.0039	-0.0046	0.0007

From Table 3.4, it is observed that there is a noticeable difference between steady-state and transient data, especially for the drag and lift forces. However, the difference in side force is negligible.

In straight line motion, both the transient and steady-state side forces, F_S, are expected to be zero due to flow symmetry. The minor side force observed is likely attributed to slight mesh asymmetries and variations in vortex shedding frequency, which can cause small lateral force fluctuations. Therefore, the analysis focuses primarily on the drag and lift forces.

It is observed that during deceleration, the drag force is lower than in the steady-state case, whereas it is higher during acceleration. This is due to the relative motion between the airfoil and the surrounding fluid. During deceleration, the airfoil velocity is lower than the fluid's, leading to a slight forward push from the flow, thereby reducing drag. Conversely, during acceleration, the airfoil moves faster than the surrounding fluid, increasing drag. This sign change in drag deviation is also evident in the comparison of force coefficients shown in Figure 3.17.

The observed differences in aerodynamic forces arise from two main contributors: the added mass effect and flow history effects, such as the influence of previous flow structures and fluid acceleration. Among these, the added mass component can be estimated and was computed using potential flow simulations carried out in OpenFOAM.

Potential flow assumes the fluid is inviscid ($\mu = 0$), incompressible, and irrotational ($\nabla \times \mathbf{V} = 0$, where $\mathbf{V}$ is the velocity vector), and free of turbulence. Although idealized, this method provides valuable theoretical insight and is often used to approximate added mass effects and benchmark CFD simulations. Despite its limitations for real-world flows, potential flow offers a useful first approximation, especially for capturing inertial contributions [Lee, 2025; University of Central Florida, 2021].

The potential flow study was conducted using a large external domain surrounding the airfoil, with a bottom plate positioned to match the corresponding ground clearance. The added mass calculation was originally intended to determine the full 6×6 matrix (forces and moments), as described in section 2.5. However, since the present study focuses exclusively on added mass in straight-line motion, and acceleration occurs only in the direction of the drag force, only the m_{11} term in the added mass matrix is relevant for translational forces.

Accordingly, the force equation simplifies from Equation 3.11 to a reduced form, where M_a denotes the added mass matrix. The moment equation in Equation 3.12 is not considered here, as the selected case involves purely straight-line motion. In this scenario, there is no angular velocity, which reduces the associated terms to zero, thereby justifying the simplification of the force equation [Newman, 2018].

$$
\begin{aligned}
F_j &= -\dot{U}_i m_{ji} - \varepsilon_{jkl} U_i \Omega_k m_{li}, \\
\begin{Bmatrix} F_{D_{am}} \\ F_{L_{am}} \\ F_{S_{am}} \\ M_{\phi_{am}} \\ M_{\psi_{am}} \\ M_{\theta_{am}} \end{Bmatrix} &= -M_a \frac{d}{dt} \begin{Bmatrix} u_x \\ u_y \\ u_z \\ \phi \\ \psi \\ \theta \end{Bmatrix} \\
\begin{Bmatrix} F_{D_{am}} \\ F_{L_{am}} \\ F_{S_{am}} \\ M_{\phi_{am}} \\ M_{\psi_{am}} \\ M_{\theta_{am}} \end{Bmatrix} &= - \begin{bmatrix} m_{11} & m_{12} & m_{13} & m_{14} & m_{15} & m_{16} \\ m_{21} & m_{22} & m_{23} & m_{24} & m_{25} & m_{26} \\ m_{31} & m_{32} & m_{33} & m_{34} & m_{35} & m_{36} \\ m_{41} & m_{42} & m_{43} & m_{44} & m_{45} & m_{46} \\ m_{51} & m_{52} & m_{53} & m_{54} & m_{55} & m_{56} \\ m_{61} & m_{62} & m_{63} & m_{64} & m_{65} & m_{66} \end{bmatrix} \frac{d}{dt} \begin{Bmatrix} u_x \\ u_y \\ u_z \\ \phi \\ \psi \\ \theta \end{Bmatrix}
\end{aligned}
\tag{3.11}
$$

$$
M_j = -\dot{U}_i m_{j+3,i} - \varepsilon_{jkl} U_i \Omega_k m_{l+3,i} - \varepsilon_{jkl} U_i U_k m_{li} \tag{3.12}
$$

$$
\left\{F_{D_{am}}\right\} = [m_{11}] \frac{d}{dt} \{u_x\} \tag{3.13}
$$

The added mass matrix was computed for a fluid density $\rho = 1.225\ \mathrm{kg/m^3}$. The resulting added mass matrix, M_a, is expressed as:

$$
M_a = \left[m_{11}\right] = \left[1.29 \times 10^{-3}\right] \tag{3.14}
$$

Using the added mass matrix M_a in the added mass force equation introduced in Equation 3.13, the added mass force vector becomes:

$$
\left\{F_{D_{am}}\right\} = \left[m_{11}\right] \left[a_x\right] = \left[1.29 \times 10^{-3}\right] \left[a_x\right] \tag{3.15}
$$

The added mass values are calculated for both deceleration and acceleration in the straight-line case, as discussed above.

During deceleration, the acceleration components are:

$$
a_x = -a\ \mathrm{m/s^2}, \quad a_y = 0\ \mathrm{m/s^2}, \quad a_z = 0\ \mathrm{m/s^2}
$$

whereas during acceleration, the acceleration components are:

$$a_x = a \text{ m/s}^2, \quad a_y = 0 \text{ m/s}^2, \quad a_z = 0 \text{ m/s}^2$$

Here, a_x, a_y, and a_z denote the acceleration in the x-, y-, and z-directions, respectively, and $a = 2g$ or $a = 5g$, depending on the case considered.

In the present discussion, we focus on an acceleration value of $2g$ for the straight-line case. When these values are substituted into Equation 3.15, the resulting added mass values for deceleration are presented in Equation 3.16, and for acceleration in Equation 3.17.

$$\left\{F_{D_{am}}\right\} = \left[1.29 \times 10^{-3}\right]\left[-19.6\right] = \left[-0.025\right] \tag{3.16}$$

$$\left\{F_{D_{am}}\right\} = \left[1.29 \times 10^{-3}\right]\left[19.6\right] = \left[0.025\right] \tag{3.17}$$

From Table 3.4, it is observed that at different time steps during deceleration and acceleration, the differences in forces are almost the same. This observation is used to verify the added mass calculation from the potential flow by comparing it with the differences between the transient flow and the steady-state values.

Therefore, one representative time step from deceleration and one from acceleration are selected, namely $t^* = 0.1$ for deceleration and $t^* = 0.9$ for acceleration. These results are presented in Table 3.5.

Table 3.5: Comparison of added mass forces from potential flow and the difference between transient and steady state CFD for the $2g$ straight-line case at $t^* = 0.1$ and $t^* = 0.9$

Force	Difference (Transient – Steady State) [N]	Added Mass (Potential Flow) [N]
	$t^* = 0.1$ **(Deceleration)**	
F_D	-0.023	-0.025
	$t^* = 0.9$ **(Acceleration)**	
F_D	0.020	0.025

The added mass force in the drag direction (F_D), computed from potential flow theory, aligns reasonably well with the differences observed between the transient and steady-state simulations for both acceleration and deceleration. The minor discrepancies can be attributed to flow history effects.

Therefore, the added mass approach offers a reasonable first-order validation of unsteady aerodynamic behavior in the drag direction. The findings suggest that added mass theory, when supported by CFD, is a valuable tool for interpreting transient aerodynamic forces. However, the complete 6×6 added mass matrix could not be obtained in this simulation.

Nevertheless, added mass theory alone does not fully explain the observed fluctuations in aerodynamic coefficients. Vortex shedding also plays a significant role in influencing aerodynamic forces and moments, contributing to the differences between added mass predictions and transient CFD results.

To further investigate differences in aerodynamic behavior between straight-line and cornering-yaw conditions, the temporal evolution of the flow must be examined. Since the acceleration and deceleration profiles are symmetric around $t^* = 0.5$ (with deceleration from $t^* = 0.0$ to $t^* = 0.5$ and acceleration from $t^* = 0.5$ to $t^* = 1.0$), analyzing either phase provides meaningful insights. This is further explored in subsubsection 3.2.2.3.

3.2.2.3. Time Resolved Analysis of Turbulence during Straight Line and Cornering Yaw Configuration

To better interpret the flow characteristics, the turbulent kinetic energy (TKE), k, is analyzed. TKE quantifies the energy contained within the turbulent fluctuations and serves as an indicator of turbulence intensity and its spatial distribution downstream of the airfoil. It is particularly useful in distinguishing the differences in fluctuation energy between the straight-line and cornering cases. A higher TKE indicates regions with stronger turbulence and greater energy in the fluctuating components of the flow. This helps identify where turbulence originates, where it is most intense, and how it evolves downstream. The turbulent kinetic energy, k, is defined as:

$$k = \frac{1}{2}\left(\overline{u'^2} + \overline{v'^2} + \overline{w'^2}\right) \tag{3.18}$$

where $\overline{u'}$, $\overline{v'}$, and $\overline{w'}$ are the root mean square (RMS) velocity fluctuations in the x, y, and z directions, respectively.

The data is analyzed for both straight-line and cornering yaw conditions throughout the complete deceleration phase, defined in the normalized time range of $t^* = 0.0$ to $t^* = 0.5$, with a time interval of $\Delta t^* = 0.1250$. This temporal resolution enables a detailed examination of the evolution of TKE, k, and reveals how turbulence intensity and distribution vary between the two flow cases. The corresponding contours are presented in Figure 3.19, providing insights into the spatial and temporal development of turbulence as the vehicle undergoes deceleration.

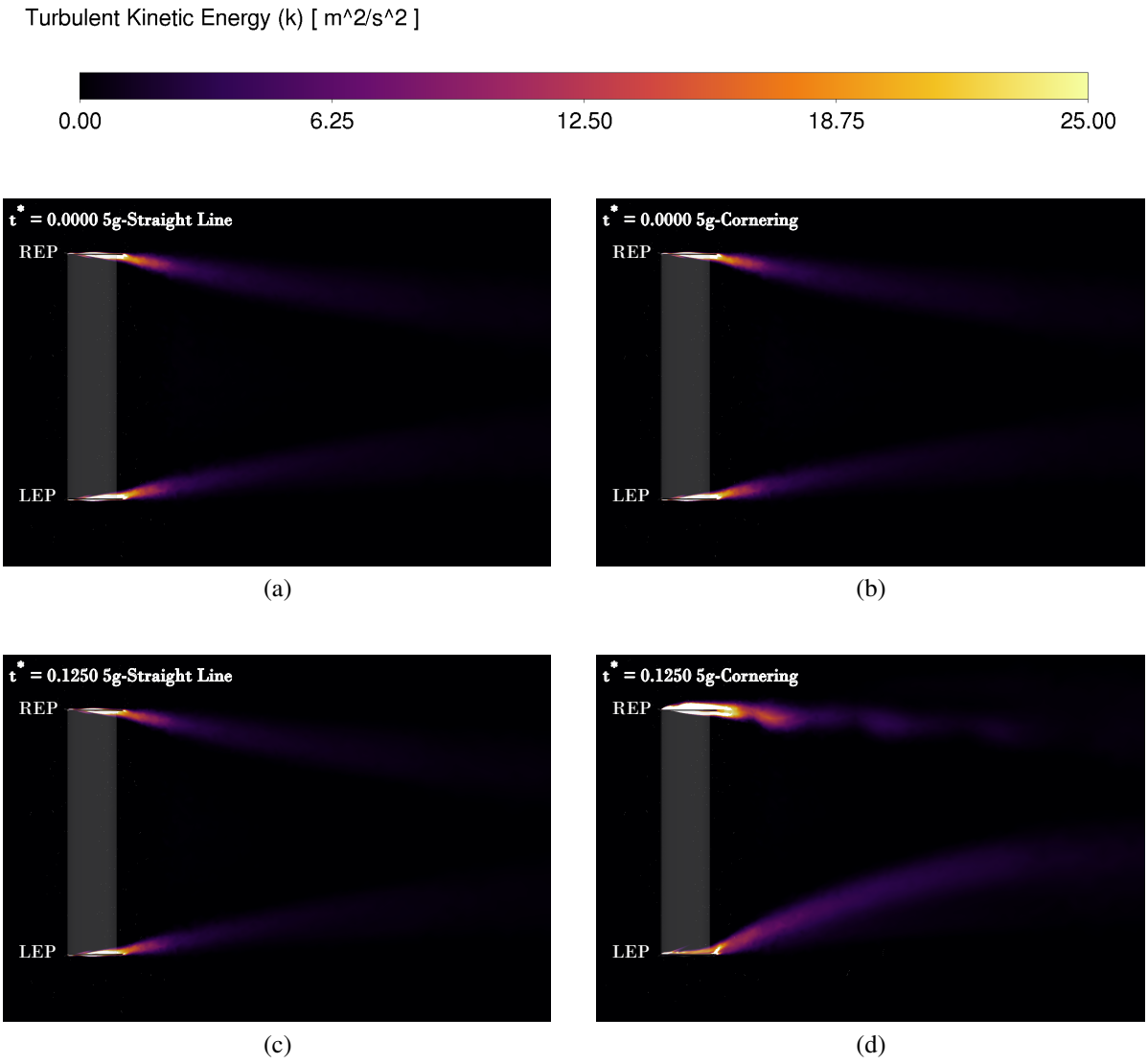

(a) (b)

(c) (d)

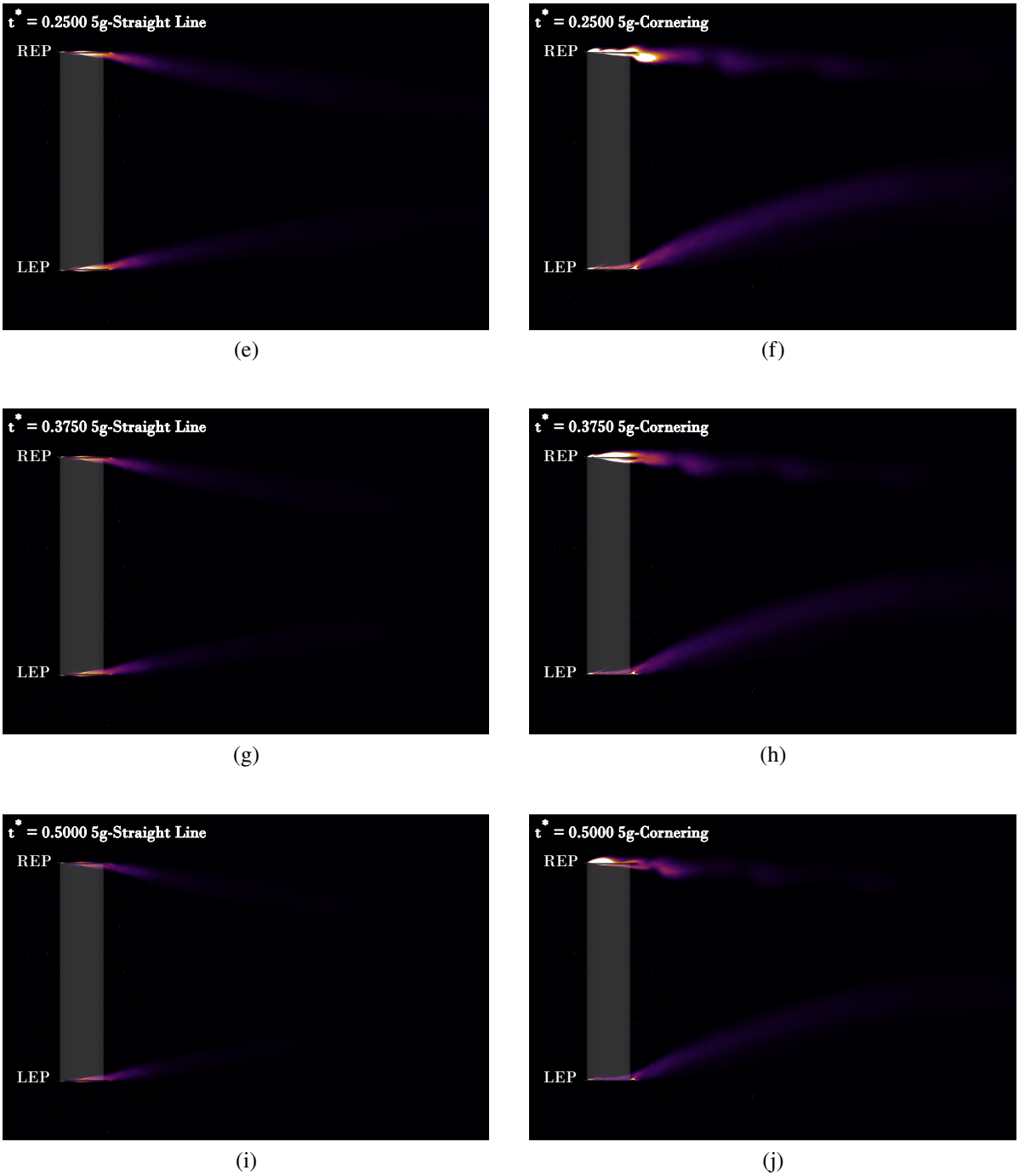

Figure 3.19: Turbulent Kinetic Energy, k, during $5g$ deceleration across the complete deceleration phase for both straight-line and cornering conditions, visualized at various normalized time steps, t^*. Left-side subfigures represent straight-line flow and right-side subfigures represent cornering yaw. REP: Right EndPlate and LEP: Left EndPlate. (a), (b) $t^* = 0.0000$ (c), (d) $t^* = 0.1250$ (e), (f) $t^* = 0.2500$ (g), (h) $t^* = 0.3750$ (i), (j) $t^* = 0.5000$

For the straight-line case, it was observed that the flow behind the airfoil was symmetric, and the turbulent kinetic energy (TKE), k, decreased progressively with the reduction in velocity, as described by Equation 3.18. Furthermore, there was minimal vortex shedding observed at any dominant frequency behind the airfoil. In contrast, for the cornering case, a significantly higher TKE was detected at the REP side of the airfoil, whereas the LEP side exhibited lower TKE compared to both the REP and the straight-line case. It was also noted that the TKE dissipated more rapidly on the REP side than on the LEP side, despite the difference in magnitude. This indicates

that the turbulence dissipates faster at the REP region, while it persists longer and travels further downstream on the LEP side.

Another important observation is that, in the straight-line case, the vorticity tends to move slightly inward towards the center of the airfoil. However, during cornering, the TKE originating from the REP region travels directly downstream behind the airfoil, whereas the TKE on the LEP side shifts towards the airfoil center with a higher gradient compared to the straight-line scenario. This behavior is primarily influenced by the flow parameters and the convection of vorticity with the flow.

To gain a clearer understanding of vortex generation near the airfoil, particular attention is given to the endplates, as these regions are primarily responsible for generating strong vortical structures and turbulence. Therefore, both the LEP and REP endplates are analyzed to highlight the differences in flow behavior, as shown in Figure 3.20. The trends observed in the turbulent kinetic energy (TKE) propagating downstream, as discussed earlier, are also evident in this more focused view.

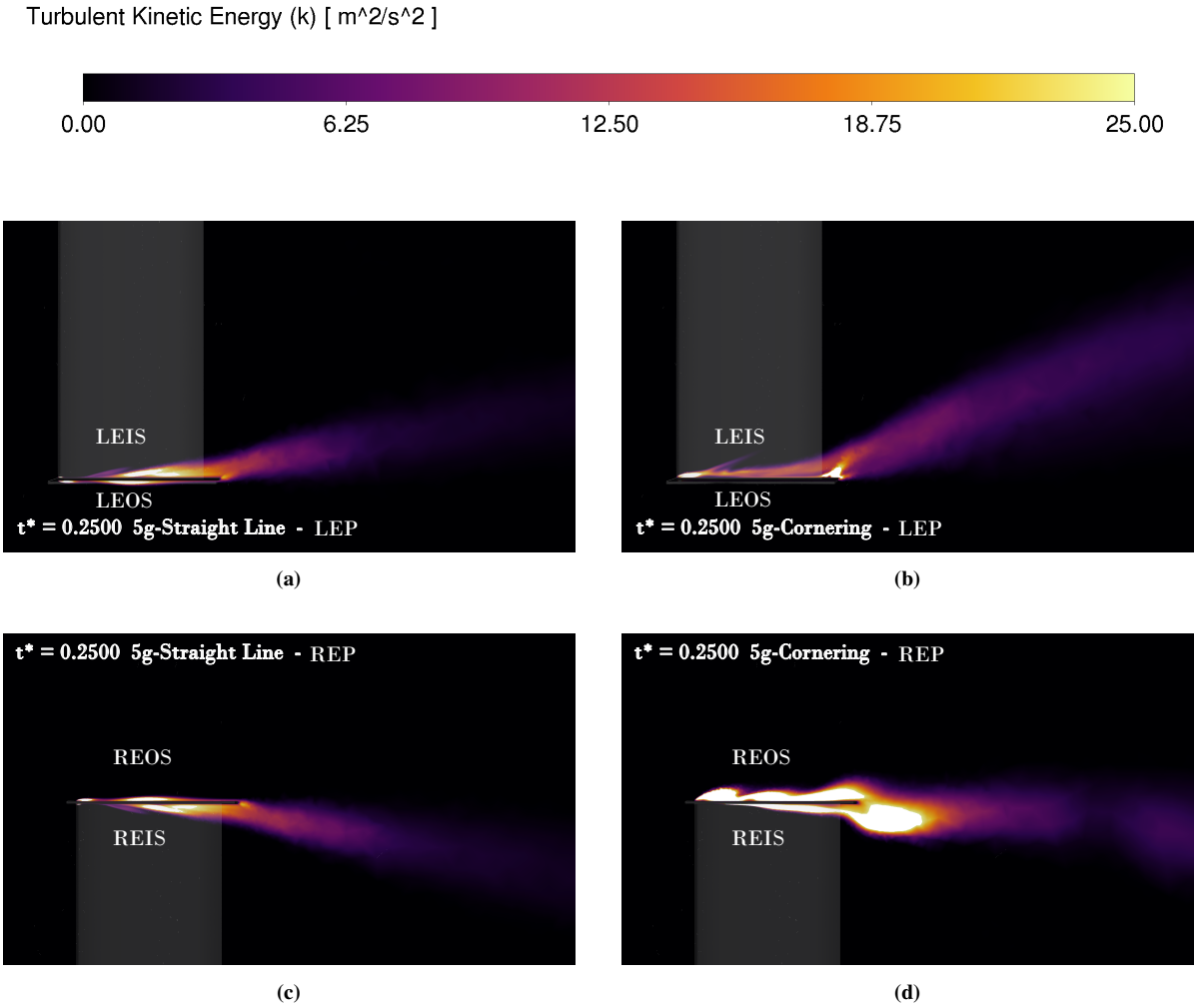

Figure 3.20: Turbulent Kinetic Energy, k, during $5g$ deceleration at $t^* = 0.2500$ (Equation 2.22) for straight-line and cornering conditions, showing a zoomed view of the Left Endplate, LEP and Right EndPlate, REP. REIS: Right Endplate Inner Surface, REOS: Right Endplate Outer Surface, LEIS: Left Endplate Inner Surface and LEOS: Left Endplate Outer Surface. (a) Straight Line – LEP, (b) Cornering – LEP, (c) Straight Line – REP, (d) Cornering – REP

At LEP, a small amount of TKE is observed on the outer face in the straight-line case, indicating limited turbulence. However, for the cornering case, almost no TKE is present in this region, suggesting minimal turbulence generation at the outer surface of the LEP endplate. A notable feature for the cornering scenario is the sharp increase in TKE at the edge of the LEP, indicating significant turbulence generation at this location.

In contrast, the REP endplate reveals a pronounced difference in TKE distribution. For the straight-line case, TKE is relatively low, with a small region of turbulence observed both near the outer and inner sides of the REP endplate. However, under cornering conditions, the TKE is substantially higher across the REP region, both at the outer and inner faces of the endplate. Furthermore, this high TKE extends downstream behind the airfoil, highlighting strong turbulence being carried along the flow direction.

This detailed comparison provides valuable insight into the formation and development of vortices and turbulence at both endplates, demonstrating that the REP endplate during cornering plays a dominant role in vortex shedding and turbulent flow generation.

As shown in Figure 3.19, vortex shedding is present, although its growth and frequency characteristics are not immediately clear. This vortex shedding phenomenon is further reflected in the aerodynamic force and moment coefficients presented in Figure 3.17 and Figure 3.18, where unsteady fluctuations in the data correlate with turbulent structures observed in the flow.

While significant vortex shedding is evident in the cornering case compared to the straight-line case, the detailed characteristics of this shedding require further investigation. To address this, a comprehensive analysis of vortex shedding during cornering is presented in subsubsection 3.2.2.4.

3.2.2.4. Temporal Characterization of Vortex Shedding in Cornering Yaw Configuration

To better understand the development of vortical structures, the analysis focuses on the onset of cornering, specifically, the transition from straight-line motion to cornering with yaw. This phase is critical for observing how the flow field and vorticity evolve, particularly in terms of vortex generation and the initiation of vortex shedding. Vorticity magnitude is used as the primary metric for this analysis.

From Figure 3.21, the top view at a distance of 0.02m below the airfoil's aerodynamic center reveals that, at the beginning of cornering, vorticity magnitude increases significantly on the LEP side of the wing. Simultaneously, the flow begins redirecting more steeply toward the center of the airfoil. On the REP side, vortices form rapidly and at a high frequency.

The front view at the trailing edge showing the LEP and REP sides, highlights additional distinctions. Before the onset of cornering, the vorticity patterns on both sides are nearly symmetrical. However, as cornering begins, the lower edge of the LEP region shows an increase in vorticity magnitude, along with the appearance of a third vortex at the junction between the LEP and the airfoil. In contrast, the REP side exhibits a strong vortex forming on the upper edge of the endplate and a clearly visible vortex shedding pattern at the lower edge, which is also corroborated by the top view.

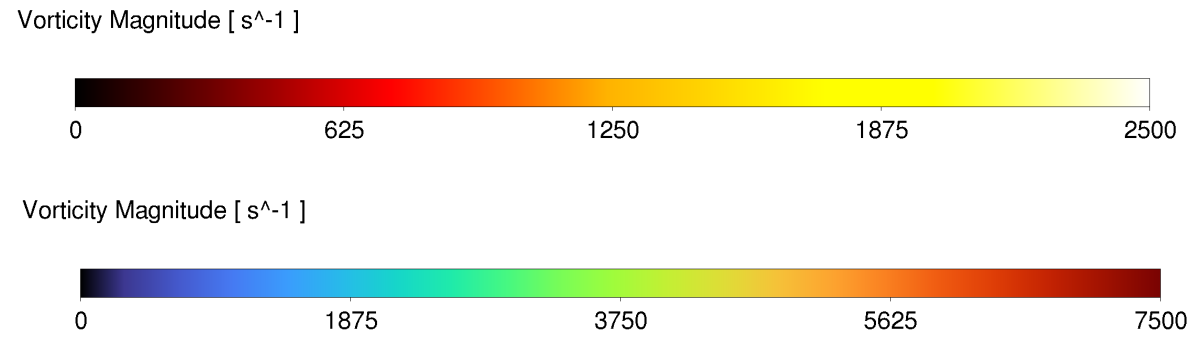
Vorticity Magnitude [s^-1]
0
625
1250
1875
2500
Vorticity Magnitude [s^-1]
0
1875
3750
5625
7500

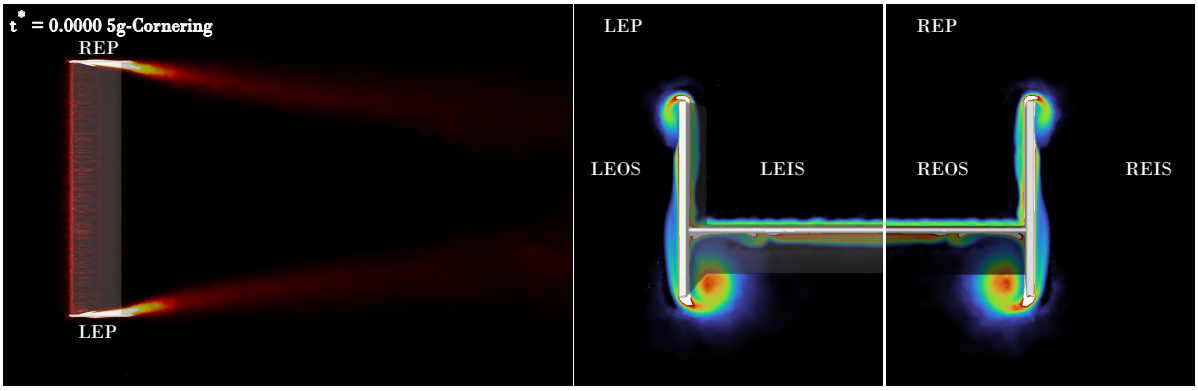
t* = 0.0000 5g-Cornering
REP
LEP
LEP
LEOS
LEIS
REP
REOS
REIS

(a)

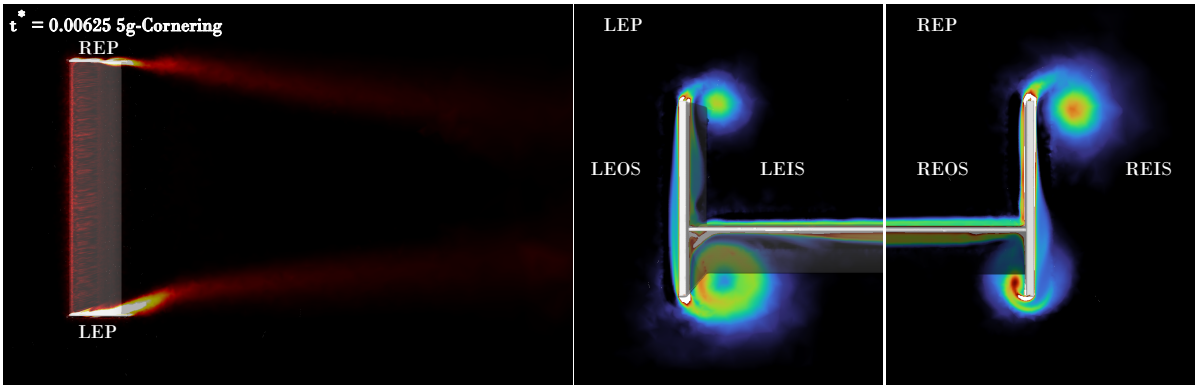
t* = 0.00625 5g-Cornering
REP
LEP
LEP
LEOS
LEIS
REP
REOS
REIS

(b)

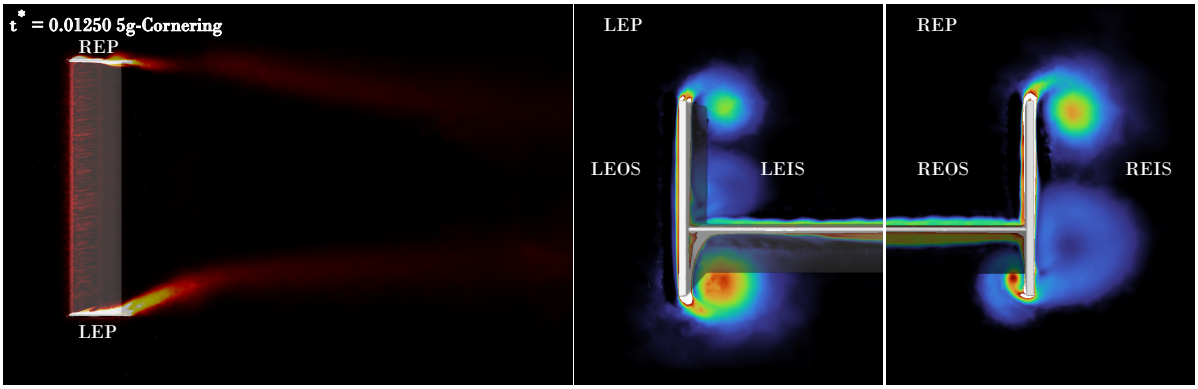
t* = 0.01250 5g-Cornering
REP
LEP
LEP
LEOS
LEIS
REP
REOS
REIS

(c)

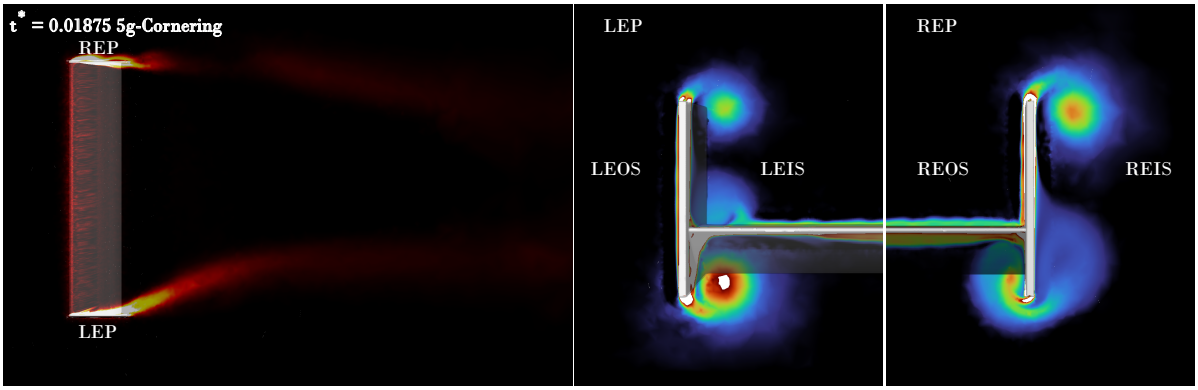
t* = 0.01875 5g-Cornering
REP
LEP
LEP
REP
LEOS
LEIS
REOS
REIS

(d)

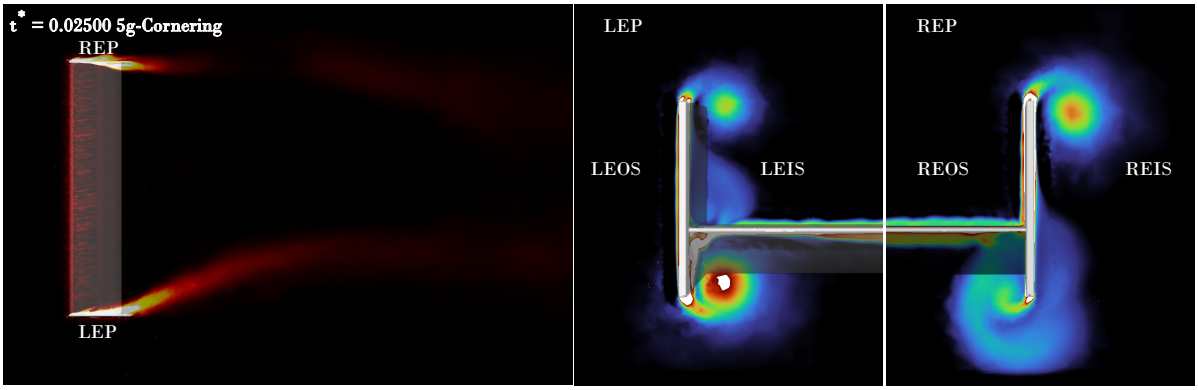
t* = 0.02500 5g-Cornering
REP
LEP
LEP
REP
LEOS
LEIS
REOS
REIS

(e)

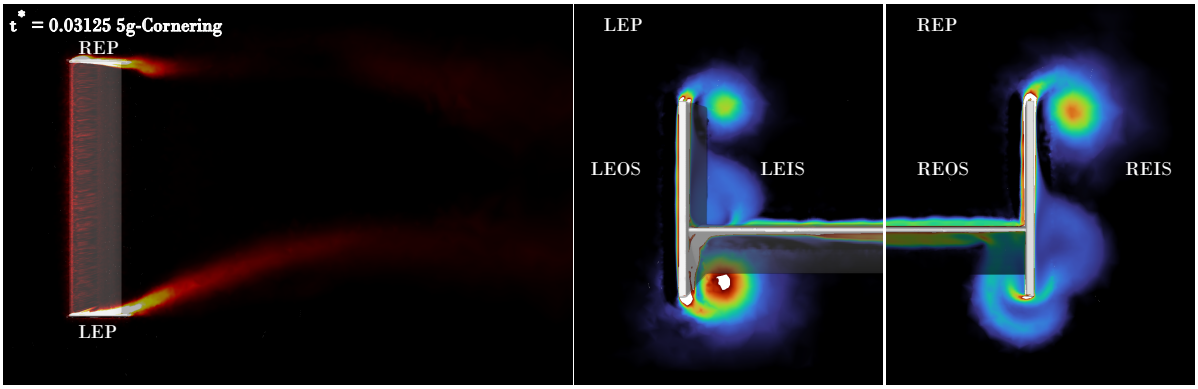
t* = 0.03125 5g-Cornering
REP
LEP
LEP
REP
LEOS
LEIS
REOS
REIS

(f)

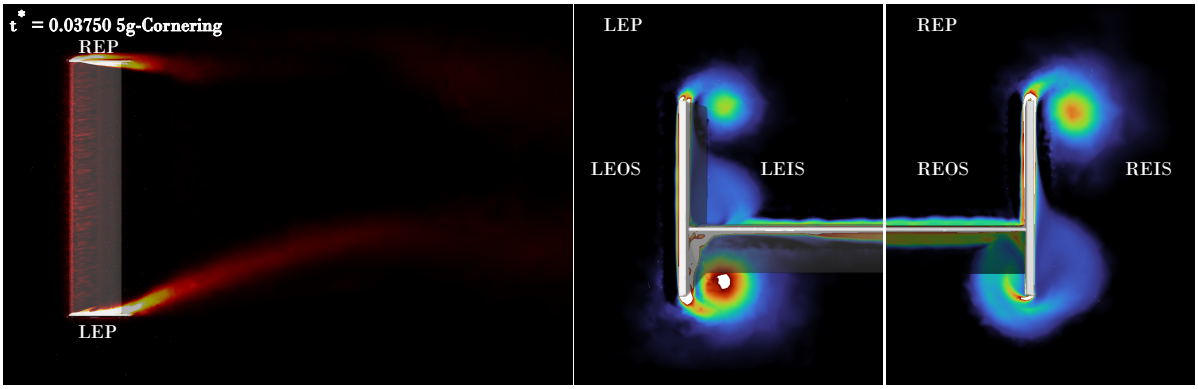
t* = 0.03750 5g-Cornering
REP
LEP
LEP
REP
LEOS
LEIS
REOS
REIS

(g)

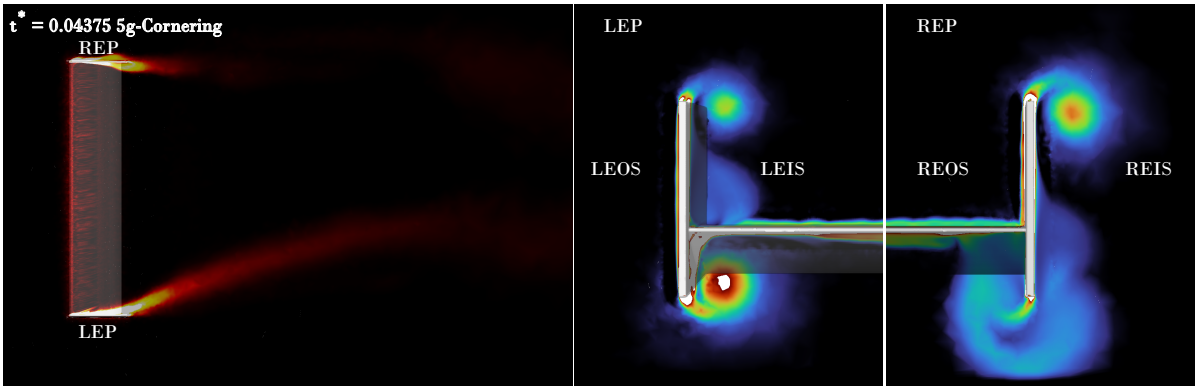

(h)

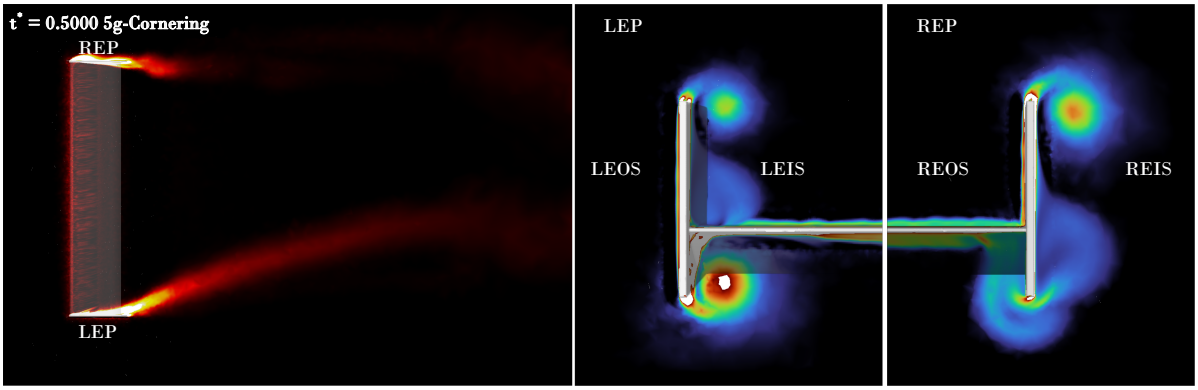

(i)

Figure 3.21: Vorticity Magnitude, ω_{mag}, during the initial phase of 5g deceleration under cornering yaw conditions, shown at various normalized flow times, t^*. The left column displays the top view of the front wing at a plane 0.02 m below the aerodynamic center of the airfoil, where the top side corresponds to the Right EndPlate, REP and the bottom side to the Left EndPlate, LEP of the front wing. The middle and right columns show front views at the trailing edge, focusing on the LEP and REP regions of the wing, respectively. REIS: Right Endplate Inner Surface, REOS: Right Endplate Outer Surface, LEIS: Left Endplate Inner Surface and LEOS: Left Endplate Outer Surface. (a) $t^* = 0.00000$ (b) $t^* = 0.00625$ (c) $t^* = 0.01250$ (d) $t^* = 0.01875$ (e) $t^* = 0.02500$ (f) $t^* = 0.03125$ (g) $t^* = 0.03750$ (h) $t^* = 0.04375$ (i) $t^* = 0.05000$

By around $t^* = 0.01875$, the shedding becomes continuous, and a repeating pattern of vortex shedding is observed, indicating the onset of periodic shedding. Prior to this, the flow remains in transition between the straight-line and cornering regimes, as evidenced by the unsteady vorticity structures on both the LEP and REP sides, with the effect being more pronounced on the REP side.

The key insight here is that the LEP side continues to exhibit minimal vortex shedding, similar to the straight-line condition, whereas the REP side demonstrates significant variations in vorticity and coherent vortical structures at each time step. To further quantify and characterize this vortex shedding behavior, the Strouhal number (St) is introduced and discussed in detail in subsubsection 3.2.2.5.

3.2.2.5. Characterization of Vortex Shedding

Vortex shedding plays a critical role in unsteady aerodynamic loading, influencing both force and moment coefficients, as highlighted in Figure 3.17, Figure 3.18, Figure 3.19, and Figure 3.21. To quantify these oscillatory behaviors, the Strouhal number (St) is used. The Strouhal number represents the ratio of inertial forces associated with local acceleration of the flow to those due to convective acceleration. It serves as a dimensionless measure of the vortex shedding frequency in relation to the flow velocity and characteristic length.

For periodic shedding flows, the Strouhal number is given by Equation 3.19 [Katopodes, 2019]:

$$St = \frac{fl}{u} \tag{3.19}$$

where f denotes the oscillation frequency, l is the characteristic length, and u represents the local flow velocity. In the present study, the characteristic length is defined as the height of the endplate, $h_{endplate} = 100$ mm, which plays a primary role in vortex generation, as observed in Figure 3.20. It is evident that vortices are generated on both sides of the endplates across the height of the endplate. The velocity u corresponds to the flow at the centerline of the wing.

Vortex shedding is observed even during straight-line motion; however, during cornering combined with acceleration and deceleration, more pronounced shedding is evident across the flow. Consequently, this study focuses on the $5g$ deceleration case within the cornering phase. In particular, the drag force and yawing moment coefficients, $C_{D_{ins}}$ and $C_{M_{\psi_{ins}}}$, are examined, as these components experience the most significant accelerations, as discussed in Figure 2.7. The analysis considers two specific intervals: the onset of cornering deceleration ($0.02 \leq t^* \leq 0.07$) and the final phase of deceleration ($0.43 \leq t^* \leq 0.48$).

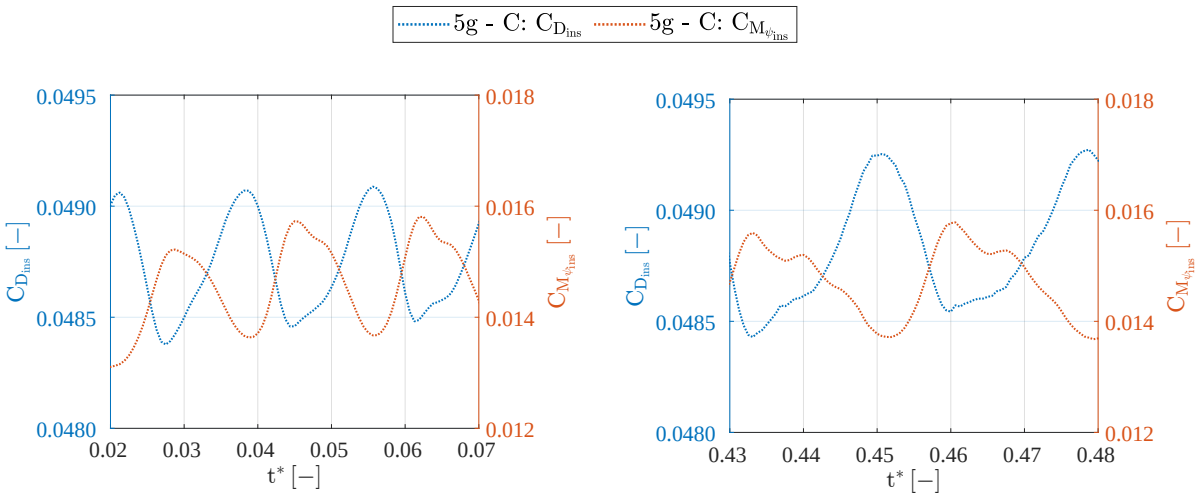

Figure 3.22: Instantaneous coefficient of drag force, $C_{D_{ins}}$ and instantaneous coefficient of yawing moment, $C_{M_{\psi_{ins}}}$ during $5g$ deceleration for the Cornering case, with zoomed-in views highlighting the start and end of the deceleration phase to analyze the effects of vortex shedding. The left y-axis represents $C_{D_{ins}}$, and the right y-axis represents $C_{M_{\psi_{ins}}}$: (a) $0.02 \leq t^* \leq 0.07$, (b) $0.43 \leq t^* \leq 0.48$

From Figure 3.22, it is evident that the oscillation frequencies of both $C_{D_{\text{ins}}}$ and $C_{M_{\psi_{\text{ins}}}}$ are nearly identical. A higher oscillation frequency is observed at the start of deceleration compared to the end, primarily due to differences in flow velocity. Higher flow velocities lead to higher oscillation frequencies of the aerodynamic forces and moments. However, while the amplitude of $C_{D_{ins}}$ fluctuations increases at lower velocities, the amplitude of $C_{M_{\psi_{ins}}}$ remains relatively constant across both intervals.

To properly compare the effects of frequency and velocity, the Strouhal number is computed using Equation 3.19, since a direct comparison of frequencies is not meaningful without accounting for changes in velocity. The computed Strouhal numbers are presented in Table 3.6. The velocity used is the average value during the respective $\Delta t^* = 0.05$ interval in which the frequency is measured. The characteristic length scale used is $l = h_{endplate} = 100$ mm.

From Table 3.6, it is observed that the Strouhal number does not change significantly between the start and end of deceleration, remaining on the order of $St \approx 0.15$. The Strouhal number obtained is broadly consistent with previous findings for a flat plate [Hemmati et al., 2016; Nedić et al., 2013]. However, unlike these studies where the incoming flow was perpendicular to the plate, the present case involves a flow incident at a specific yaw angle due to the front wing orientation during cornering. This angular inflow likely contributes to the slight deviation from values reported in earlier research.

Table 3.6: Vortex shedding characteristics during the $5g$ cornering deceleration phase

	Start of Deceleration Figure 3.22a ($0.02 \leq t^* \leq 0.07$)	End of Deceleration Figure 3.22b ($0.43 \leq t^* \leq 0.48$)
Velocity, u $[m/s]$	40.406	24.334
Time Period of Fluctuations $[s]$	0.0175	0.025
Frequency, f $[s^{-1}]$	57.14	40
Reference length, l $[mm]$	100	100
Strouhal Number, St [-]	0.141	0.164

4

Conclusions

4.1. Summary

This study focused on understanding the aerodynamic flow behavior during cornering through computational simulations, with a particular emphasis on the effects of acceleration and deceleration. It highlighted the importance of distinguishing between straight-line and cornering flow conditions, especially under transient motion, which are critical in vehicle dynamics and aerodynamic performance prediction.

The report begins with an introduction to the motivation behind the research, emphasizing the significance of the front wing in generating downforce and influencing overall vehicle handling. This is followed by a theoretical overview covering essential aerodynamic concepts relevant to automotive applications, including boundary layer behavior, vortex generation, and unsteady flows resulting from acceleration and deceleration. Previous research findings were reviewed, with particular attention given to studies demonstrating the deviations in aerodynamic forces under transient conditions compared to steady-state assumptions.

In chapter 2, the simulation methodology is presented, detailing the computational domain, meshing strategy (including boundary layer resolution and refinement zones), and the applied boundary conditions. The turbulence modeling approach using the SST k–ω model is discussed along with the governing equations. The section also outlines the velocity and acceleration profiles used for both straight-line and cornering cases, providing context for their formulation and relevance.

The results chapter (chapter 3) begins by comparing the different motion scenarios: straight-line, cornering normal, and cornering with yaw. While cornering normal is often used in literature, this study focuses on cornering with yaw, which better represents real-world racecar dynamics. A detailed analysis of aerodynamic forces and moments under acceleration and deceleration conditions was conducted, particularly for the straight-line and cornering-yaw configurations.

Key findings reveal that cornering with yaw leads to significantly different aerodynamic behavior compared to the straight-line case, with added mass effects playing a major role in force variations. Furthermore, vortex shedding was observed in both configurations; however, its frequency and impact were notably higher during cornering, influencing both force and moment coefficients. This made Strouhal number analysis essential to characterize the unsteady flow behavior.

Among the critical results, it was found that the drag force during deceleration is consistently lower than during acceleration in both straight-line and cornering conditions. This insight has potential implications for racecar performance optimization, especially in scenarios where every millisecond matters. Additionally, the large differences observed in yawing moments between straight-line and cornering cases offer a plausible explanation for the unpredictable handling or instability often seen in vehicles entering corners, potentially leading to loss of control.

4.2. Recommendations and Future Works

- In real racecar cornering, angular velocity and acceleration profiles are highly nonlinear and do not follow the step response applied in this study. The simplified profile used here served to isolate and analyze flow characteristics during cornering. Future studies should incorporate gradually varying angular velocities and accelerations to better mimic real vehicle dynamics.
- The linear velocity and acceleration profiles employed in this study were chosen to clearly understand the effects of transient behavior. However, in practical scenarios, vehicle acceleration tends to follow nonlinear trends. Incorporating such realistic profiles in simulations would improve the accuracy and applicability of the findings.
- The simulations used reference data inspired by the Monaco Grand Prix corner, with simplified assumptions including a fixed cornering radius. However, in real races, drivers seldom follow a perfectly circular trajectory. Employing actual telemetry or GPS based racing data to define realistic cornering paths and inputs will significantly enhance simulation fidelity and insight.
- The simulations were performed using the Reynolds-Averaged Navier–Stokes (RANS) approach. While RANS provides a time-averaged solution that captures overall flow behavior efficiently, it has limitations in resolving transient flow structures and vortex dynamics. For more accurate representation of vortex shedding, evolution, and fine-scale turbulence, advanced modeling approaches such as Large Eddy Simulation (LES) can be employed, as they resolve a broader range of turbulent scales and better capture the detailed shape and dynamics of vortical structures.
- The added mass effects were calculated only for the straight-line case in the direction of acceleration. It would be interesting to also investigate the effects in other directions as well as on the moments. Understanding the added mass is expected to be particularly important in the cornering case, as many flow features change significantly, as observed in this thesis. Such an analysis could therefore provide valuable insights into unsteady aerodynamic behaviour under more complex manoeuvres.

A

Experimental and Numerical Methods for Straight Line and Cornering Testing

The experimental setup and the various computational methods used to evaluate the flow behavior are discussed in detail in the following sections, beginning with the procedures applied for the straight line case and then followed by the cornering case.

A.1. Experimental and Numerical Methods in Straight Line Testing

The methodology is presented in two parts: the experimental procedures are outlined first, followed by a detailed description of the numerical simulation techniques:

A.1.1. Experimental Methods in Straight Line Testing

Experiments play a crucial role in the development of products, especially in fields like automotive, aeronautics, and aerospace. Unexpected results can lead to significant financial losses or, in the worst case, pose risks to human life. Therefore, conducting aerodynamic experiments is essential to ensure safety and efficiency.
For straight-line aerodynamic experiments, several highly accurate methods are available. Some of the most widely used approaches are discussed in the following sections.

A.1.1.1. Wind Tunnel

Wind tunnels have played a crucial role in fluid flow analysis across various fields, including automobiles, aircraft, and spacecraft. They provide a realistic representation of flow behavior, allowing engineers to obtain empirical data that can be compared with simulation results, thereby validating and refining computational models as computational methods are cheaper to execute than a wind tunnel test.

In Formula 1, wind tunnels have been extensively utilized for aerodynamic development over the years. However, following the 2021 regulations, wind tunnel usage has been restricted, leading to a greater reliance on accurate CFD simulations. Despite these limitations, teams continue to conduct wind tunnel tests using a 60% scaled model of an F1 car, as shown in Figure A.1, to optimize aerodynamic performance within the permitted constraints.

Figure A.1: A 60% scaled model of a F1 car tested in a Wind tunnel [Formula 1, 2024b]

A.1.1.2. Water Tank

Unlike a wind tunnel, where the test body remains stationary or its wheels run over a treadmill, a water tank experiment involves moving the test body through the system. This is achieved using a high-degree-of-freedom robotic arm that controls the motion and acceleration of the body within the tank, allowing for precise investigation of flow effects.

This method has been employed to study flow behavior over both flat plates and airfoils, providing valuable insights into unsteady aerodynamics. Figure A.2 illustrates the experimental setup used for analyzing the flow over a flat plate moving through the tank.

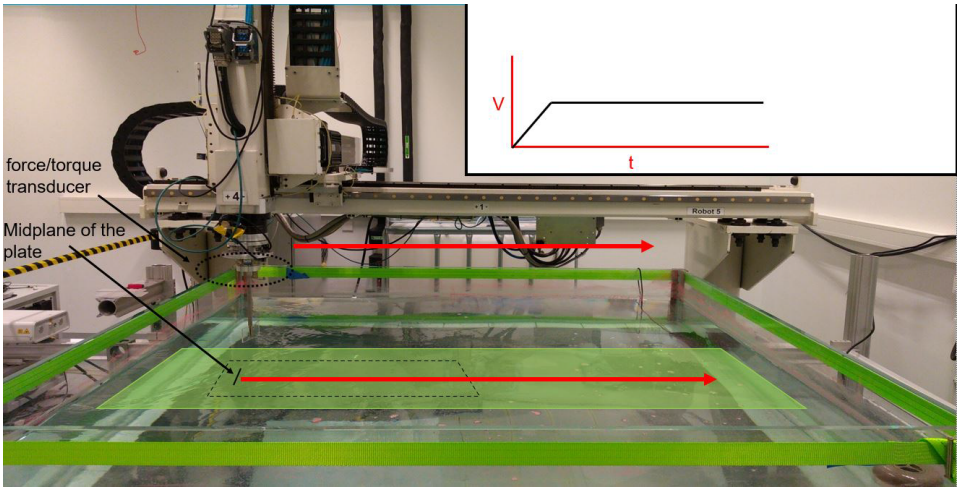

Figure A.2: Experimental setup for Particle Image Velocimetry (PIV). The gantry robot moves the plate from left to right, following the red arrow. From the robot head downwards, the following items are attached: a force/torque transducer, a streamlined strut, and the rectangular plate. The laser sheet comes from the left and the camera is located below the tank. The green area indicates the position of the laser sheet, with the field-of-view of the camera indicated by the dashed black area. The horizontal midplane of the plate is indicated by the black line within the field-of-view. The inset graph shows the plate velocity profile as a function of time [Reijtenbagh et al., 2022]

A.1.1.3. Dynamic track

Another approach involves creating a controlled environment to simulate the required motion. Some existing facilities operate in repurposed rail tunnels for straight-line aerodynamic testing. However, applying this method to cornering aerodynamics presents challenges, as constructing a dedicated curved test section for each new experiment is costly and impractical.

Following a similar principle, the Princeton Dynamic Model Track was developed to assess aircraft stability. In

this setup, a carriage was used to accelerate the model as shown in Figure A.3 and was used primarily for low-speed testing [CURTISS et al., 1964]. While this method offers valuable insights, it requires a significantly large facility, and achieving high-speed conditions poses additional challenges.

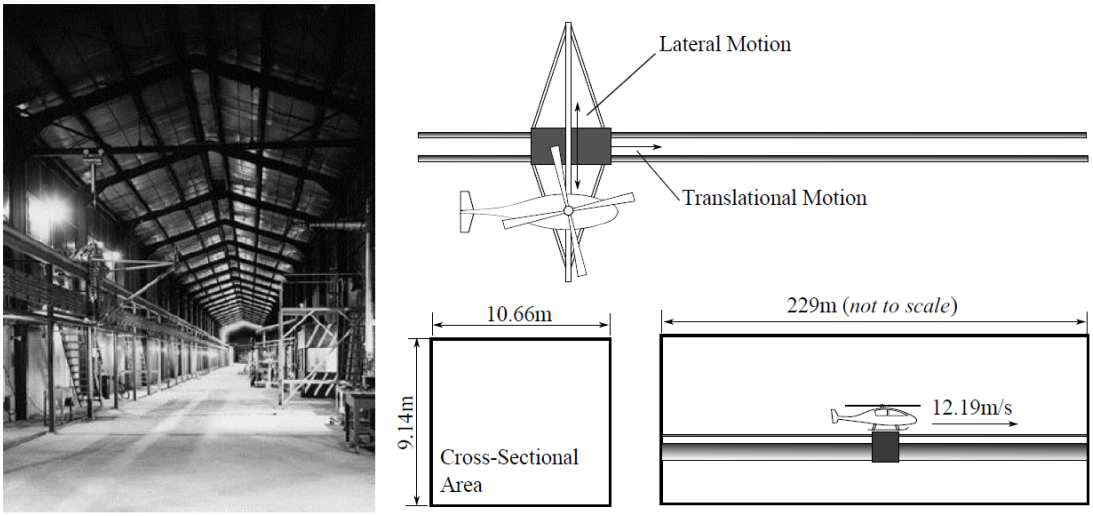

Figure A.3: Depicts the real and a schematic of the Princeton Dynamic Model Track [CURTISS et al., 1964; Keogh, 2016]

A.1.1.4. Ring of Fire

A novel approach developed at TU Delft, known as the Ring of Fire [TU Delft - Aerodynamics Group, 2024], is a type of onsite aerodynamic analysis. This method consists of a controlled tunnel through which the test subject moves, utilizing tracer particles, an illumination system, and an imaging system to provide detailed insights into flow velocity measurements and wake dynamics.

Unlike traditional wind tunnel testing, the Ring of Fire does not require a dedicated test facility and can be deployed directly at training grounds. It has been successfully applied in sports such as ice skating and cycling [Spoelstra et al., 2021; Terra et al., 2023]. Figure A.4 illustrates its use for analyzing the aerodynamics of ice speed skaters.

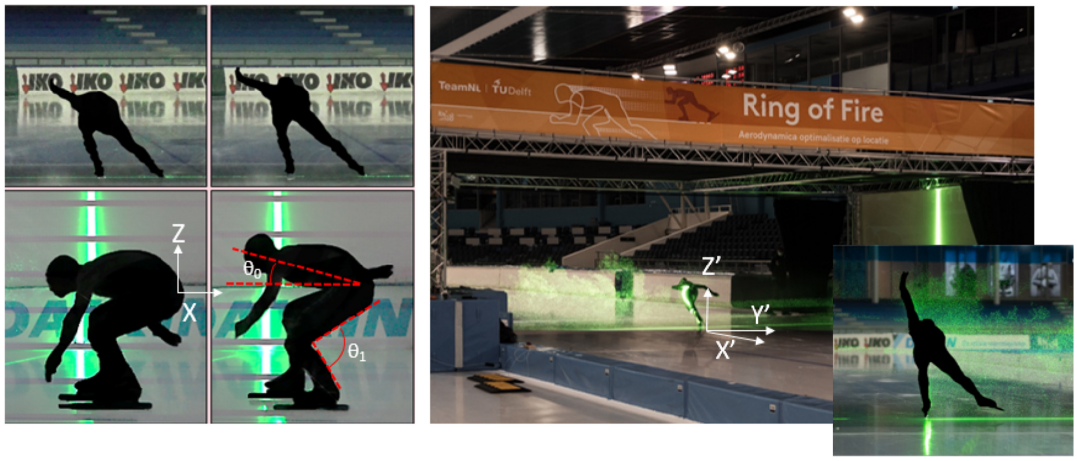

Figure A.4: Represents speed skaters passing through the Ring of fire [Terra et al., 2023]

In the context of automotive aerodynamics, this method can be particularly useful for obtaining data at specific points along a track. However, capturing aerodynamic behavior over an entire circuit would require multiple measurement setups and repeated test runs, significantly increasing both cost and time.

Experimental methods are invaluable for testing the aerodynamic performance of bodies, but they do have limitations. One major constraint is the size of the body being tested, with scaled models typically used for such

experiments. Conducting experiments can be quite costly, particularly when redesigning components or performing a series of tests. Additionally, the experimental setup itself can be expensive, especially when testing large-scale structures or conducting multiple tests. As a result, numerical methods play a crucial role in overcoming these challenges. Computational techniques provide a cost-effective and time-efficient alternative, enabling more detailed analysis without the need for extensive physical testing. Some of the key computational methods used to address these issues are discussed in subsection A.1.2.

A.1.2. Numerical Methods in Straight Line Testing

For simulating translational experiments, multiple approaches can be employed, each with its own advantages and limitations. Some of the most widely used methods are discussed below.

A.1.2.1. Stationary Frame Method

In the Stationary Frame Method, the target body remains fixed while the surrounding flow is set to move at the required translational velocity. This setup closely resembles wind tunnel experiments (subsubsection A.1.1.1), where the test object is stationary, and air is directed toward it to simulate movement as shown in Figure A.5a.

While widely used due to its simplicity and ease of implementation, this method has certain drawbacks. In accelerating flows, the added mass effects are not inherently accounted for and must be introduced separately in simulations. If not applied correctly, this can lead to inaccuracies in the results. Additionally, because the method does not replicate the real-world motion of a moving body, it may not always provide the most precise aerodynamic insights, particularly in transient or highly dynamic flow conditions.

A.1.2.2. Moving Frame Method

In the Moving Frame Method, the target body along with the free moves transitionally along with the airflow, effectively replicating real-world conditions as shown in Figure A.5b. This approach inherently accounts for additional terms associated with accelerating flows, making it advantageous for simulations. Unlike the Stationary Frame Method, where certain dynamic effects must be introduced separately, the Moving Frame Method ensures a more comprehensive analysis by naturally incorporating all relevant parameters.

Despite its complexity in setup this method remains widely used due to its ability to accurately simulate real-world scenarios. It is particularly beneficial for studying transient aerodynamic effects, such as those investigated in water tank experiments (subsubsection A.1.1.2), where the test body moves through the fluid medium rather than remaining stationary.

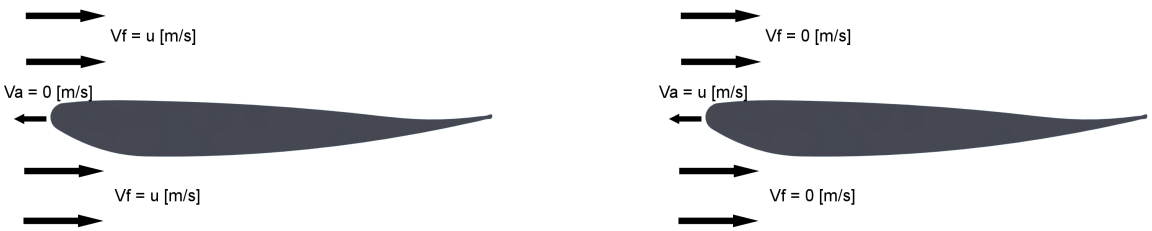

(a) **(b)**

Figure A.5: Illustration of an airfoil in motion, where Va represents the velocity of the airfoil, Vf denotes the velocity of the incoming flow, and u signifies any arbitrary velocity of the fluid or the body. (a) Stationary frame method of an airfoil undergoing translational motion (b) Moving frame method of an airfoil undergoing translational motion.

A.1.2.3. Overset Method

In the Overset Method, two distinct mesh settings are utilized: a stationary mesh and a moving mesh that overlays the stationary one. Figure A.6 illustrates a simulation involving an Ahmed body (denoted as A) moving near a stationary wall (denoted as W) to analyze the aerodynamic effects when the Ahmed body is in proximity to a vertical surface [Bounds et al., 2019].

This method is a relatively recent approach that offers several advantages, including the ability to simulate complex motion paths and curved trajectories with greater flexibility. However, it also has significant computational drawbacks. The method requires a large computational domain leading to high computational costs and increased processing power requirements.

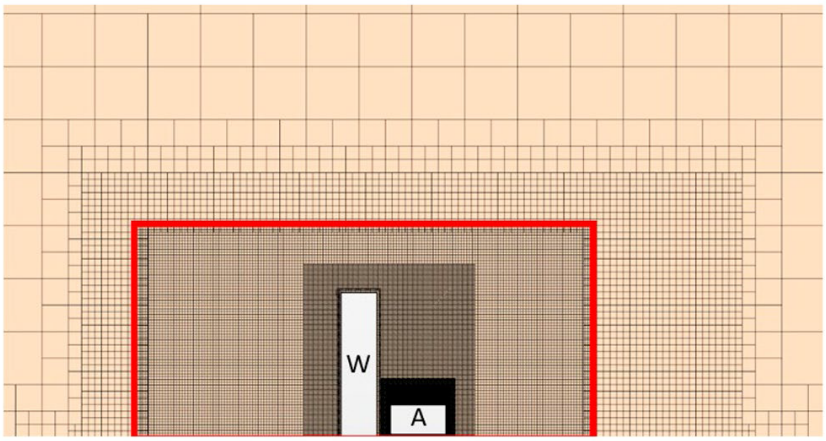

Figure A.6: Front view of the mesh showing the side-wall, marked as "W," and Ahmed body, marked as "A"; the overset region is marked by the thick-lined red border [Bounds et al., 2019]

A.2. Experimental and Numerical Methods of Cornering Testing

The methodology is presented in two parts: the experimental procedures are outlined first, followed by a detailed description of the numerical simulation techniques:

A.2.1. Experimental Methods in Straight Line Testing

Numerous previous studies have shown that there is no single perfect or definitive method for analyzing cornering aerodynamics in a controlled environment. Research in this field has spanned several decades, with significant advancements in onsite aerodynamics. However, accurately replicating real-world conditions and obtaining comprehensive data remains a challenge. Various experimental approaches have been explored to address these limitations, including the whirling arm, rotary rig, and bent model, each offering unique insights into cornering aerodynamics. These methods are discussed in detail below.

A.2.1.1. Whirling Arm

The whirling arm operates by moving the model around a pivot point, as illustrated in Figure A.7a. The first whirling arm was developed in 1746 by mathematician Benjamin Robins and was later refined by notable aerodynamicists such as Sir George Cayley, Otto Lilienthal, and Samuel Langley [Hunt et al., 2005].

This method offers certain advantages in the field of automotive aerodynamics. Unlike a wind tunnel testing, it simulates vehicle motion with a stationary ground, eliminating the need for rolling road setups. However, a major drawback is that the model travels through its own wake, resulting in high levels of turbulence and flow disturbances, which can lead to inaccurate results.

To address these limitations, a new whirling arm facility was constructed at the National Physical Laboratory (NPL) in the UK, with modifications implemented between 1908 and 1942 [Mulkens and Ormerod, 1990]. The facility was later relocated to Cranfield University, where improvements were made to enhance result accuracy. However, despite these advancements, issues related to flow quality persisted, preventing the method from fully achieving its intended purpose.

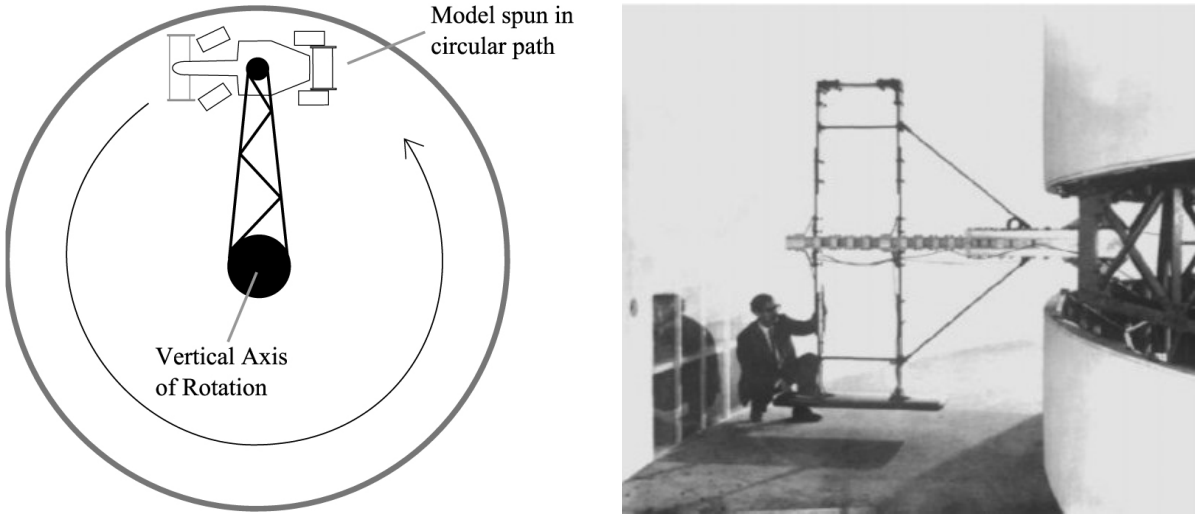

(a) (b)

Figure A.7: Whirling Arm Facility [Keogh, 2016; Keogh, Barber, et al., 2015] (a) Motion of a car in a whirling arm facility (b) Setup of a model in the Cranfield Whirling Arm Facility

A.2.1.2. Rotary Rig

Advancements in the field of the rotary rig have significantly improved its application in wind tunnels by offering multiple degrees of freedom [Pattinson et al., 2013]. This solves the issue encountered in whirling arm setups, where the model travels through its own wake, allowing for a more accurate replication of cornering motion Figure A.8.

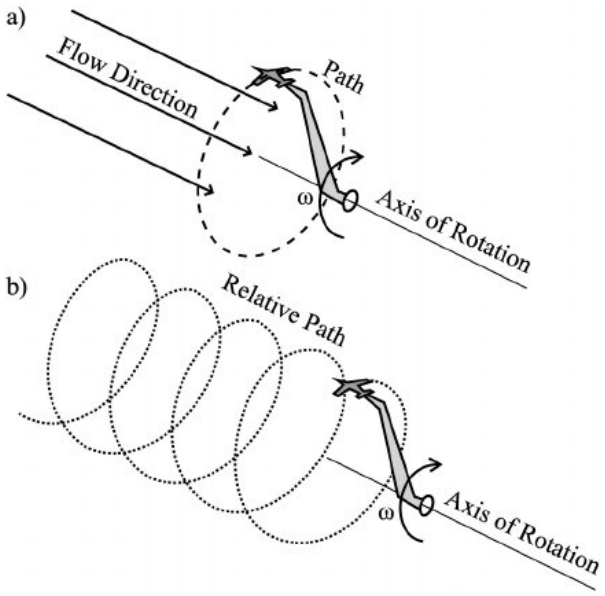

Figure A.8: Steady-State Coning Motion of a Wind Tunnel Model Induced by a Rotary Rig [Keogh, 2016; Keogh, Barber, et al., 2015] (a) Representation in the absolute reference frame (b) Representation in the model's reference frame

However, this method also presents several challenges. The arm supporting the model behaves like a bluff body, which can disrupt the flow and introduce unwanted interference. Additionally, testing with a rotary rig often requires large and open test sections to mitigate the blockage effects caused by the bluff body. Designing an appropriate ground plane to simulate ground effects, as required for many automotive studies, is also complex and difficult to implement effectively in such setups.

A.2.1.3. Curved Test Section Wind Tunnel

Using a curved test section in wind tunnel, instead of a conventional straight section, is another method for assessing curved flows over a model. In 1939, the Langley Research Center constructed a wind tunnel designed to test the rolling, pitching, and yawing motions of an aircraft. The tunnel was curved, and the flow was forced to follow the curved shape, which ultimately reduced flow quality, as shown in Figure A.9 [NASA, 2024b].

In such curved sections, the outer radius experiences a higher velocity, while the inner radius has a lower velocity. This curvature creates a suction surface on the outer radius and a pressure surface on the inner radius. The outer curve, being concave, causes the flow to decelerate, while the inner curve, being convex, accelerates the flow. The resulting velocity profile is therefore not as expected, but rather the opposite of what would ideally occur [Berger et al., 1983].

Figure A.9: Inside View of the Langley Stability Tunnel Curved Test Section [Keogh, 2016; Keogh, Barber, et al., 2015]

A.2.1.4. Bent Model

In this approach, the body is bent to simulate the required cornering motion, making it relative to the straight free-stream flow rather than a curved flow with a straight model as shown in Figure A.10. However, several challenges arise, particularly in the construction of the model or car. Both the wheel and the body must be curved accordingly, which increases complexity and requires redesigning for each new type of corner.

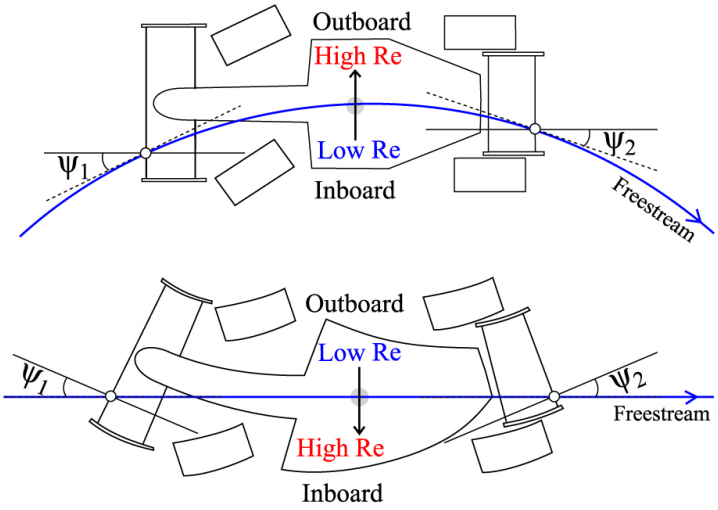

Figure A.10: Example of a Model Deformed to Simulate Cornering Motion in a Left-Hand Turn Compared to a Standard Cornering Case. The upper half illustration represents curved flow around the model, while the lower depiction shows a bent model subjected to a straight flow [Keogh, Barber, et al., 2015]

Furthermore, due to the bending, the inner and outer lengths of the car differ. This creates the same issues encountered in the case of curved test sections in a wind tunnel, where the flow behavior is altered due to the variation in the path lengths along the curved surface.

Due to these challenges with experimental methods and the difficulty in obtaining precise results, computational approaches have become increasingly essential and the methods are discussed in subsection A.2.2.

A.2.2. Numerical Methods in Corner Testing

Numerical methods play a crucial role in analyzing flow characteristics during cornering and turning, as experimental techniques often do not fully meet the required conditions, as discussed in subsection A.2.1. Various approaches are considered when modeling the aerodynamic behavior of automobiles in cornering conditions, and these are discussed below:

A.2.2.1. Computational Domain

The choice of computational domain is a critical factor in ensuring accurate and efficient simulations, as it directly influences the reliability of the results and the feasibility of running the simulations effectively.

For cornering flows, selecting an appropriate computational domain becomes even more crucial. Unlike straight-line flow simulations, where the domain setup is relatively straightforward, cornering introduces additional complexities. Neither the curved nor the rectangular domain (Figure A.11) is inherently superior, as both have their own advantages and limitations.

The curved domain is tailored to match the radius of the cornering motion, making it well-suited for cases where a fixed turning radius is being analyzed. However, if simulations need to be conducted for multiple radii, the domain must be redefined for each case, increasing setup time and computational effort.

On the other hand, the rectangular domain provides greater flexibility, as the inlet and outlet boundaries can be adjusted to accommodate different cornering radii without requiring an entirely new domain setup. This can lead to significant computational savings. However, accurately defining the inlet and outlet positions becomes critical to prevent unwanted flow mixing and ensure the results are meaningful.

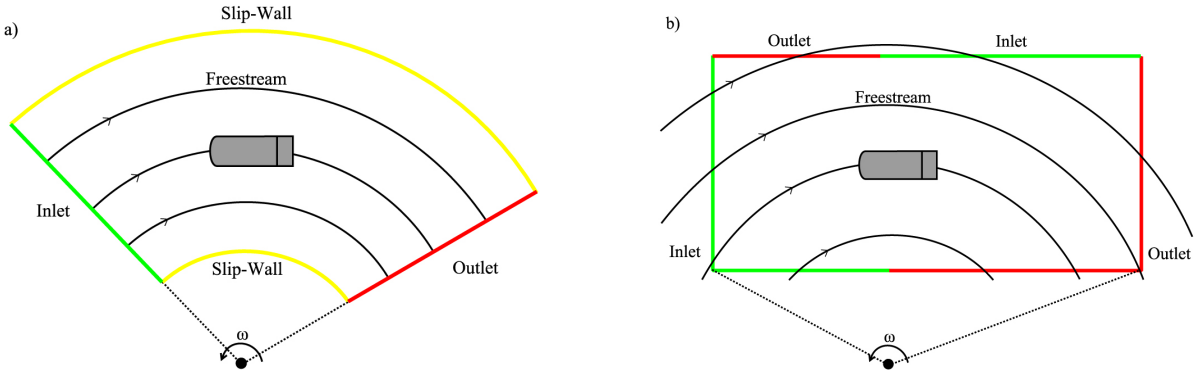

Figure A.11: Different computational domain for cornering analysis of an Ahmed body (a) Curved computational domain (b) Rectangular computational domain [Keogh, Barber, et al., 2015]

A.2.2.2. Stationary Frame Method

The stationary frame method, as discussed in subsubsection A.1.2.1 (Figure A.5a), involves keeping the object fixed while allowing the airflow to pass around it. This approach allows for flexibility in choosing the computational domain, as any type of domain can be used depending on the specific requirements of the simulation.

One key limitation of the stationary frame method is that additional forces, such as Coriolis and centripetal forces, are not inherently accounted for in the simulation. Since the object remains fixed rather than moving through the flow, these forces must be explicitly included in the computational setup to ensure accurate results. Neglecting these forces can lead to discrepancies between the simulation and real-world behavior, particularly in cases involving rotational or accelerating flows.

A.2.2.3. Moving Frame Method / Moving Boundary Method

Like discussed in subsubsection A.1.2.2 (Figure A.5b), the body along the frame moves, unlike a stationary frame where the fluid region moves within the domain.

Figure A.12a represents the complete computational domain rotating along a circular path. This approach effectively recreates cornering or angular flow analysis, simulating real-world road conditions. Figure A.12b illustrates how the Arbitrary Lagrangian-Eulerian (ALE) method can be applied within a non-inertial frame, capturing the dynamics of a vehicle undergoing cornering. The figure demonstrates how the computational domain moves to replicate the turning motion of the vehicle. The ALE method offers the advantage of simulating flows through multiple corners and complex cornering paths, rather than being limited to a simple circular trajectory. This flexibility makes it particularly useful for analyzing real-world driving scenarios where vehicles navigate intricate curves and varying radii of curvature.

This method is advantageous as it inherently accounts for Coriolis and centrifugal forces, which are not included in the stationary frame method.

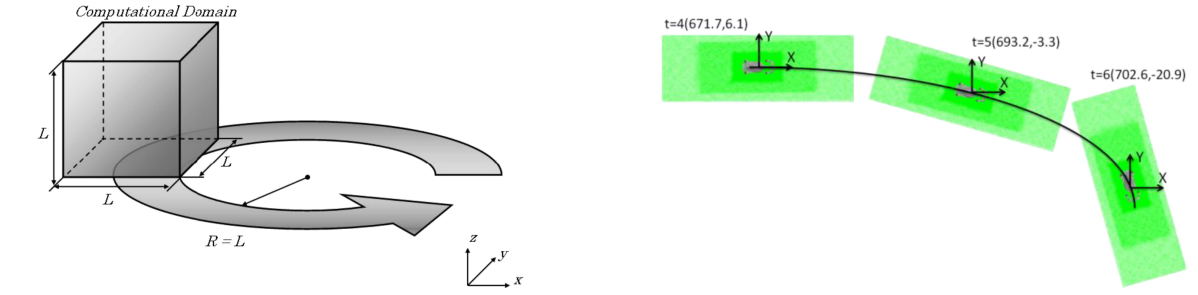

(a) **(b)**

Figure A.12: (a) Rotation of a cubic computational domain in a stationary fluid [Watanabe and Matsuno, 2009] (b) Arbitrary Lagrangian-Eulerian (ALE) method with a non-inertial frame [Nara et al., 2014]

B

Overview of Research Approaches and findings for Straight-Line and Cornering Flows

The latest studies on the aerodynamic effects in both straight-line motion and cornering are reviewed to understand recent advancements in the field. A detailed discussion of these cases is provided in section B.1 and section B.2.

B.1. Aerodynamic Effects on a Straight-Line Track

In straight-line motion, the object moves in a single direction, and any acceleration or deceleration occurs along the same axis as the velocity. Therefore, the critical aerodynamic parameters to analyze in such conditions include:

1. **Drag and Lift Forces** – Understanding how these forces evolve during acceleration and deceleration.
2. **Drag and Lift Coefficients ($C_{D,std}$, $C_{L,std}$)** – Studying the coefficients in Steady State.
3. **Instantaneous Drag and Lift Coefficients ($C_{D,ins}$ (Equation 1.1), $C_{L,ins}$ (Equation 1.2))** – Observing real-time fluctuations in aerodynamic forces due to acceleration and deceleration transient effects.
4. **Pressure Coefficient (C_p)** – Analyzing changes in pressure distribution on the surface to determine how acceleration affects flow characteristics.
5. **Wall Shear Stress (T_w)** – Examining how boundary layer separation changes with acceleration and deceleration.

For the analysis of aerodynamic effects in a straight line, both experimental and computational approaches have been employed. Computational methods offer several advantages over experimental testing due to their flexibility in analyzing different conditions, as well as their comparatively lower cost, since there is no need to repeatedly manufacture and modify physical components. A detailed discussion of the experimental and computational methods are provided in subsection A.1.1 and subsection A.1.2, while the key results obtained are presented and analyzed in the following section:

B.1.1. Previous Research Results on Straight-Line Testing

In the field of aerodynamic flow analysis for straight-line testing, extensive research has been conducted both experimentally and computationally. The following sections discuss critical aerodynamic characteristics observed in different airfoils, providing insights into their performance under varying conditions.

The Angle of Incidence (AOI) of the airfoil is a critical aspect to study. Figure B.1 illustrates how drag and lift forces change with varying AOI of a T026 airfoil over an acceleration profile, with peak acceleration occurring at 3.6 seconds. It can be observed that as the AOI increases, the negative lift force values rise, along with an increase in drag force. The peak forces are observed at an AOI of 10.95 degrees, while the lowest values occur at 3.45 degrees.

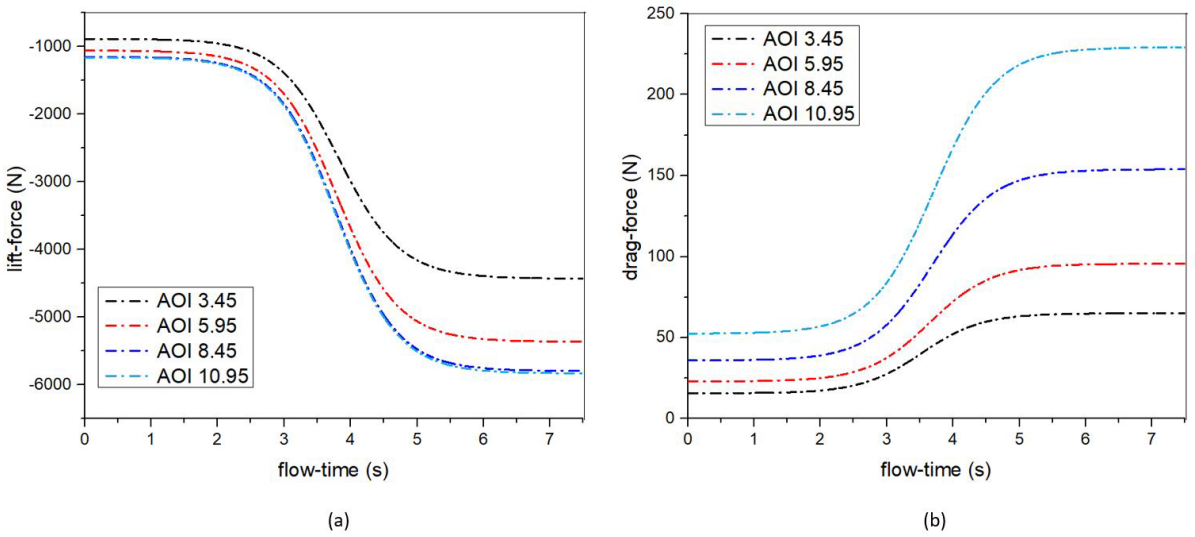

Figure B.1: Changes in Forces with the Change in Angle of Incidence (AOI) of a T026 airfoil (a) Downforce Generated by the Airfoil at Different AOI (b) Drag Force generated by the Airfoil at Different AOI [Pathanadka, 2022]

Traditionally, for an accelerating flat plate that resembles Hiemenz flow as shown in Figure B.2, it has been assumed that the non-circulatory added mass force scales linearly with acceleration, i.e., $F_a \propto a$. However, recent experimental studies have shown that, for high Reynolds number flows, the unsteady (or history) drag force instead scales with the square root of acceleration, i.e., $F_a \propto \sqrt{a}$ [Reijtenbagh et al., 2023]

This suggests that the classical added mass approximation may not be sufficient for capturing the true unsteady force behavior across different geometries and flow regimes. Therefore, a more accurate determination of the scaling relationship is necessary, tailored to the specific flow conditions and body shape, rather than relying on simplified or generalized assumptions.

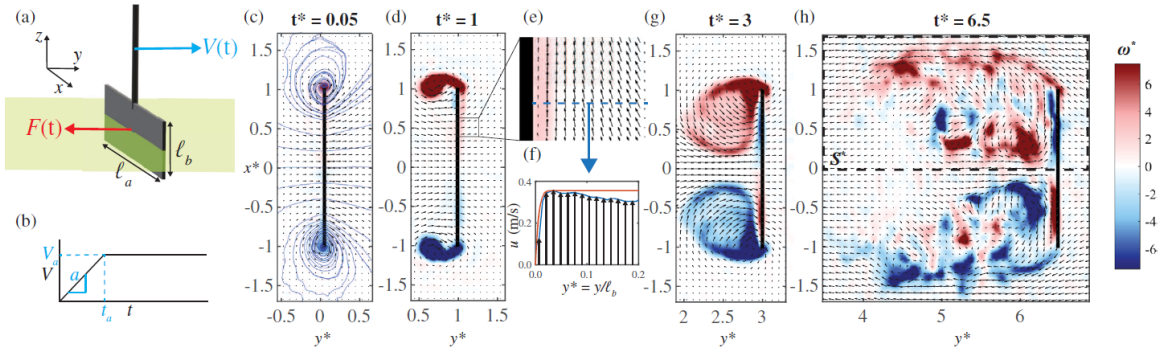

Figure B.2: (a) A plate with dimensions $l_a l_b$ moves through a viscous fluid at velocity $V(t)$ and experiences a force $F(t)$. PIV measurement plane (green) at the plate midplane. (b) Imposed velocity $V(t)$ of the plate: $V = at$ (with constant acceleration a) for $0 < t < t_a$ and constant V_a for $t > t_a$. (c),(d),(g),(h) Measured velocity fields and vorticity * for $a^* = 0.5$ ($t_a^* = 1.0$) at $t^* = 0.05$ (with streamlines), 1.0, 3.0, 6.5, respectively. (e) Detail near upstream plate surface. (f) Velocity profile along blue dashed line in (e); red line represents the velocity profile. The plate velocity is subtracted for (e) and (h). All dimensions are normalized by l_b [Reijtenbagh et al., 2023]

Extensive research has been conducted on the aerodynamic effects of acceleration and deceleration for various bodies, including the Ahmed body, flat plates, and different airfoil profiles. These studies have provided valuable insights into transient aerodynamic forces and their impact on vehicle performance. Now, we shift our focus to cornering motion, examining the critical features to enhance our understanding of aerodynamics in turning conditions.

B.2. Aerodynamic Effects During Cornering Motion

In cornering motion, an object does not travel in a single direction; instead, its velocity has components along the curvature of the turn. Any acceleration or deceleration experienced during this motion is referred to as centripetal acceleration, which is responsible for maintaining the curved trajectory. Therefore, the critical aerodynamic parameters to analyze under these conditions include:

1. **Drag and Lift Forces** – Understanding how these forces evolve during cornering and cornering acceleration/deceleration.
2. **Drag and Lift Coefficients** ($C_{D,std}$, $C_{L,std}$) – Studying the coefficients in Steady State.
3. **Instantaneous Drag and Lift Coefficients** ($C_{D,ins}$**(Equation 1.1),** $C_{L,ins}$**(Equation 1.2))** – Observing real-time fluctuations in aerodynamic forces due to acceleration and deceleration transient effects.
4. **Pressure Coefficient** (C_p) – Analyzing changes in pressure distribution on the surface to determine how acceleration affects flow characteristics.
5. **Wall Shear Stress** (T_w) – Examining how boundary layer separation changes with acceleration and deceleration.
6. **Yaw, Pitch and Rolling Moment** - Analyzing the changes in the moments during transient cornering acceleration and decelerations.

The effects are analyzed using both experimental and simulation methods. The experimental and numerical methods are discussed in subsection A.2.1 and subsection A.2.2, while the key results obtained are presented and analyzed in the following section.

B.2.1. Previous Research Results on Cornering Flow Testing

Cornering simulations are crucial in the field of automobiles, as vehicles do not solely travel in a straight line. Understanding the aerodynamic effects during cornering is essential for optimizing performance, stability, and control. As previously discussed, achieving the right balance between drag and downforce is vital to maximize speed while maintaining vehicle stability.

Various cornering simulations have been conducted on different bodies, revealing critical insights into drag, lift, moment coefficients, and the corresponding forces. Some of the key findings from these simulations are discussed below.

Detailed analysis of the Ahmed body in cornering simulations has provided valuable insights. As shown in Figure B.3a, the coefficient of drag, along with its pressure and viscous components, increases as the cornering radius decreases, indicating higher aerodynamic resistance as more of the body is exposed to the air flow. Meanwhile, Figure B.3b demonstrates that the coefficient of lift remains relatively unaffected by changes in cornering radius. However, as the radius decreases, both the coefficient of side force and the yawing moment exhibit a reduction.

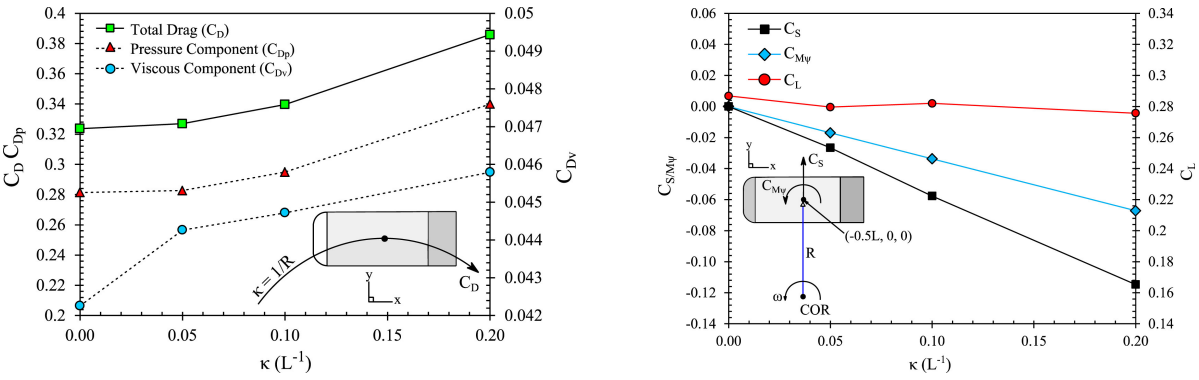

(a) (b)

Figure B.3: Aerodynamic coefficients of the Ahmed body at different cornering radii (a) Coefficient of total drag, pressure component, and viscous component (b) Coefficient of side force, yawing moment, and lift [Keogh et al., 2016]

Due to the curved flow in cornering conditions, one side of the Ahmed body is more directly exposed to the oncoming airflow. As shown in Figure B.4, the boundary layer near the inboard side where the flow first interacts with the body is thinner compared to the outboard side. This results in an increase in pressure along the outboard surface, leading to the formation of a larger vortex near the rear end of the Ahmed body on the outboard side.

This vortex, known as the C-pillar vortex, is more pronounced on the outboard than on the inboard surface.

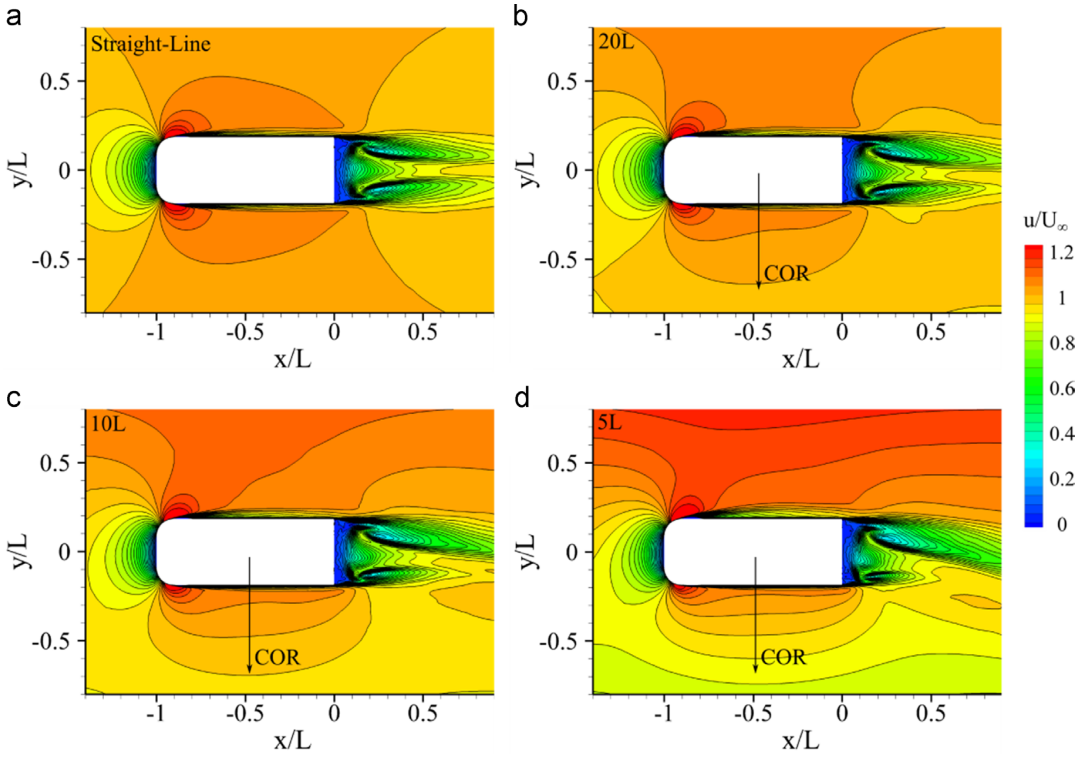

Figure B.4: X-velocity contours at $z/L = 0.18$ for (a) the straight-line case, (b) 20L radius corner, (c) 10L radius corner, and (d) 5L radius corner [Keogh et al., 2016]

C

Tyrell Wing Profile (T026)

C.1. Wing Profile

The coordinates used for generating the 2D and 3D Tyrrell profile are presented.

Table C.1: Coordinates of the 2D and 3D Tyrrell 026 Airfoil [Pathanadka, 2022; Zerihan and Zhang, 2001a]

Suction Surface		**Pressure Surface**	
x/c	y/c	x/c	y/c
0	0	0	0
0.001	-0.0076	0.001	0.0079
0.002	-0.0107	0.002	0.0109
0.0049	-0.0168	0.0051	0.0173
0.0099	-0.0228	0.0101	0.0232
0.0149	-0.0266	0.0151	0.0271
0.0199	-0.0294	0.0201	0.03
0.0249	-0.032	0.0251	0.0313
0.0298	-0.0345	0.0301	0.0322
0.0348	-0.0369	0.0351	0.033
0.0398	-0.0393	0.0401	0.0338
0.0448	-0.0416	0.0451	0.0346
0.0498	-0.0438	0.0501	0.0354
0.0548	-0.046	0.0551	0.0361
0.0598	-0.0481	0.0601	0.0369
0.0698	-0.052	0.0701	0.0382
0.0797	-0.0557	0.0801	0.0395
0.0897	-0.0591	0.0902	0.0407
0.0997	-0.0622	0.1002	0.0417
0.1197	-0.0676	0.1202	0.0436
0.1396	-0.0718	0.1402	0.0451
0.1596	-0.075	0.1602	0.0463
0.1796	-0.0769	0.1802	0.0472
0.1996	-0.0778	0.2002	0.048
0.2496	-0.0762	0.2501	0.0498
0.2996	-0.0732	0.3001	0.0515
0.3496	-0.0692	0.3501	0.0527
0.3996	-0.0645	0.4001	0.0534
0.4496	-0.059	0.4501	0.0537
0.4996	-0.0526	0.5001	0.0535
0.5497	-0.0454	0.5501	0.0529

Continued on next page

Table C.1 – continued from previous page

Suction Surface		Pressure Surface	
x/c	y/c	x/c	y/c
0.5997	-0.0373	0.6001	0.0518
0.6497	-0.0285	0.65	0.0503
0.6997	-0.0188	0.7	0.0482
0.7498	-0.0083	0.75	0.0456
0.7998	0.0031	0.8	0.0438
0.8498	0.0152	0.85	0.0443
0.8999	0.0282	0.9	0.0479
0.9199	0.0336	0.92	0.0502
0.9399	0.0392	0.94	0.053
0.9599	0.0449	0.96	0.0562
0.9799	0.0507	0.98	0.0599
0.99	0.0537	0.99	0.0619
1	0.0567	1	0.064

The aerofoil is selected to have a chord length, c = 223.4 mm with the endplate dimensions as shown in Figure C.1 and has a thickness of 4 mm.

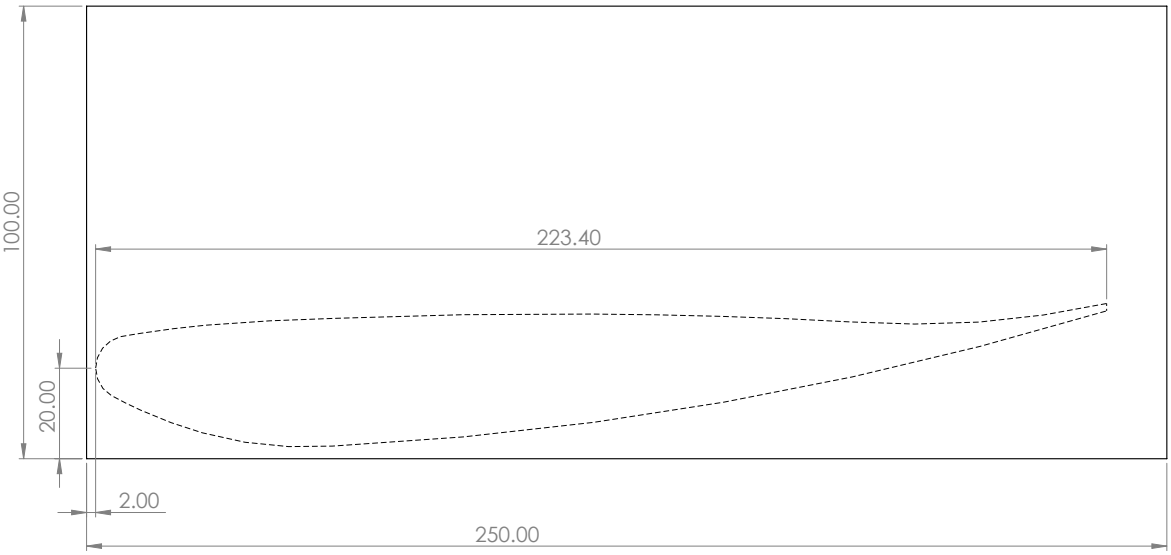

Figure C.1: Dimensions of the side view of the front wing showing the endplate along with the airfoil (all dimensions in mm) [Pathanadka, 2022; Zerihan and Zhang, 2001a]

References

AeroTools. (n.d.). *Wing in ground proximity (wig)* [Accessed: 2025-06-17]. https://mh-aerotools.de/airfoils/jf_wig.htm

Analytics. (n.d.). *Coupled vs segregated cfd flow solvers* [Accessed: 2025-06-09]. https://www.resolvedanalytics.com/cfd/coupled-vs-segregated-cfd-flow-solvers

ANSYS Inc. (2021, July). *ANSYS Fluent Theory Guide, Release 2021 R2* [Version 2021 R2; sourced from CFD Experts mirror]. ANSYS, Inc. Canonsburg, PA, USA. https://dl.cfdexperts.net/cfd_resources/Ansys_Documentation/Fluent/Ansys_Fluent_Theory_Guide.pdf

ANSYS Inc. (2024). *Ansys fluent user's guide, release 2024 r1* [Accessed: 2025-01-09]. ANSYS Inc. Canonsburg, PA, USA.

Aultman, M. (2017). Investigation into geometric parameters of an inverted airfoil in ground effect with the utilization of classic optimization techniques. *Undergraduate Research Thesis, Dept. of Mechanical and Aerospace Engineering, Ohio State Univ., Columbus, OH*.

Autodromo. (2024). *Ferrari 312b* [Accessed: 2024-12-30]. http://autodromo.co.uk/automotive/the-autodromo-archive/ferrari-312b/#1681-ferrari-312b/1703

Barretto, L. (2020). The 2021 f1 cost cap explained – what has changed, and why? [Accessed: 2024-12-27]. *Formula 1®*. https://www.formula1.com/en/latest/article/the-2021-f1-cost-cap-explained-what-has-changed-and-why.5O1Te8udKLmkUl4PyVZtUJ

Berger, S., Talbot, a. L., & Yao, L.-S. (1983). Flow in curved pipes. *Annual review of fluid mechanics*, *15*, 461–512.

Bonhams. (2024). *The ex-graham hill, richard attwood, joakim bonnier, dave charlton 1968-69 lotus-cosworth ford type 49b formula 1 and tasman racing single-seater, chassis no. 49b/r8* [Accessed: 2024-12-30]. https://cars.bonhams.com/auction/21906/lot/342/the-ex-graham-hill-richard-attwood-joakim-bonnier-dave-charlton1968-69-lotus-cosworth-ford-type-49b-formula-1-and-tasman-racing-single-seater-chassis-no-49b-r8/

Bounds, C. P., Mallapragada, S., & Uddin, M. (2019). Overset mesh-based computational investigations on the aerodynamics of a generic car model in proximity to a side-wall. *SAE International Journal of Passenger Cars-Mechanical Systems*, *12*(06-12-03-0015), 211–223.

BrambleCFD. (2022). *Time to rethink cornering flow* [Accessed: 2025-06-08]. https://bramblecfd.com/time-to-rethink-cornering-flow/

Cadence CFD. (2022). *Hexahedral mesh vs. tetrahedral: Comparing high-quality meshing* [Accessed: 2025-07-15]. https://resources.system-analysis.cadence.com/blog/msa2022-hexahedral-mesh-vs-tetrahedral-comparing-high-quality-meshing

CURTISS, H., JR, Putman, W., & Traybar, J. (1964). The princeton dynamic model track. *Aerodynamic Testing Conference*, 1104.

DMS. (2025). *Practical cfd modeling: Turbulence* [Accessed: 2025-07-26]. https://www.dmsonline.us/practical-cfd-modeling-turbulence/

F1 Chronicle. (2023). *Formula 1 circuit maps* [Accessed: 2024-12-30]. https://f1chronicle.com/formula-1-circuit-maps/

FindBlueprints. (2024). *Tyrrell 026 f1 gp ow 1998 — blueprint* [Accessed: 2024-12-30]. https://findblueprints.com/catalog/cars/tyrrell/tyrrell-026-f1-gp-ow-1998

Flight Study. (2024). *Wingtip vortices* [Accessed: 2024-12-30]. https://flight-study.com/wingtip-vortices/

Formula 1. (2024a). *2024 canadian grand prix qualifying results* [Accessed: 2024-12-30]. https://www.formula1.com/en/results/2024/races/1237/canada/qualifying

Formula 1. (2024b). *How f1's new sliding scale aero testing rules work – and what impact they will have* [Accessed: 2024-12-30]. https://www.formula1.com/en/latest/article/how-f1s-new-sliding-scale-aero-testing-rules-work-and-what-impact-they-will.pn0sG8N4A0cjbNRbdYx8a

Formula 1. (2024c). *Watch: The origins of ground effect* [Accessed: 2024-12-30]. https://www.formula1.com/en/latest/article/watch-the-origins-of-ground-effect.6i1MZBs5xe6cjO2deb57hV

Francis, A. (2024). *In numbers: How 2024 came to be one of the most thrilling f1 seasons yet*. Retrieved December 30, 2024, from https://www.formula1.com/en/latest/article/in-numbers-how-2024-came-to-be-one-of-the-most-thrilling-f1-seasons-yet.6nlrEsGGuIRTqA5TeFQHJ6.html

Google Earth Pro. (2025, June). Image of fairmont monaco hairpin from google earth pro. https://earth.google.com/web/

Grift, E., Vijayaragavan, N., Tummers, M., & Westerweel, J. (2019). Drag force on an accelerating submerged plate. *Journal of Fluid Mechanics*, *866*, 369–398.

GroundEffect, M. E. (2024). *Understanding ground effect: How the effect impacts formula 1* [Accessed: 2024-12-30]. https://motorsportengineer.net/understanding-ground-effect-how-the-effect-impacts-formula-1/

Hemmati, A., Wood, D. H., & Martinuzzi, R. J. (2016). Characteristics of distinct flow regimes in the wake of an infinite span normal thin flat plate. *International Journal of Heat and Fluid Flow*, *62*, 423–436.

Hunt, R., Hornby, G. S., & Lohn, J. D. (2005). Toward evolved flight. *Proceedings of the 7th annual conference on Genetic and evolutionary computation*, 957–964.

IdealSimulations. (2024). *Courant number in cfd simulations* [Accessed: 2025-07-17]. https://www.idealsimulations.com/resources/courant-number-cfd/

Katopodes, N. D. (2019). Chapter 5 - viscous fluid flow. In N. D. Katopodes (Ed.), *Free-surface flow* (pp. 324–426). Butterworth-Heinemann. https://doi.org/https://doi.org/10.1016/B978-0-12-815489-2.00005-8

Katz, J. (2006). Aerodynamics of race cars. *Annu. Rev. Fluid Mech.*, *38*(1), 27–63.

Keogh, J. (2016). *The aerodynamic effects of the cornering flow conditions* [Doctoral dissertation, UNSW Sydney].

Keogh, J., Barber, T., Diasinos, S., & Doig, G. (2016). The aerodynamic effects on a cornering ahmed body. *Journal of Wind Engineering and Industrial Aerodynamics*, *154*, 34–46.

Keogh, J., Barber, T. J., Diasinos, S., & Doig, G. (2015). Techniques for aerodynamic analysis of cornering vehicles. *18th Asia Pacific Automotive Engineering Conference Proceedings: Melbourne, Australia*.

Keogh, J., Doig, G., Barber, T. J., & Diasinos, S. (2014). The aerodynamics of a cornering inverted wing in ground effect. *Applied Mechanics and Materials*, *553*, 205–210.

Keogh, J., Doig, G., Diasinos, S., & Barber, T. (2015). The influence of cornering on the vortical wake structures of an inverted wing. *Proceedings of the Institution of Mechanical Engineers, Part D: Journal of Automobile Engineering*, *229*(13), 1817–1829.

Kumar, R. (2022). What are the budgets for f1 teams including mercedes, red bull & ferrari? [Accessed: 2024-12-27]. *EssentiallySports*. https://www.essentiallysports.com/f1-news-what-are-the-budgets-for-f1-teams-including-mercedes-red-bull-ferrari/

Lee, S. (2025, June). *The ultimate guide to potential flow theory* [Accessed: 2025-06-14]. https://www.numberanalytics.com/blog/ultimate-guide-potential-flow-theory

Lux, B. (2024). *F1 98 - technical details of the 1998 formula 1 car* [Accessed: 2024-12-30]. https://www.boris-lux.de/04_types/11_f1/f1_98/f198.php#ARR

Massachusetts Institute of Technology. (2005). *2005 reading 6 - hydrodynamics (2.016/13.012), fall 2005* [Accessed: 2025-06-09]. https://ocw.mit.edu/courses/2-016-hydrodynamics-13-012-fall-2005/resources/2005reading6/

McLaren Racing. (2022). *The secrets of a formula 1 simulator*. https://www.mclaren.com/racing/latest-news/mclarenracing/article/secrets-formula-1-simulator/

Mercedes-AMG Petronas Formula One Team. (2021). *Feature: Downforce in formula one, explained* [Accessed: 2024-12-30]. https://www.mercedesamgf1.com/news/feature-downforce-in-formula-one-explained

Mulkens, M., & Ormerod, A. (1990). *Steady-state experiments for measurements of aerodynamic stability derivatives of a high incidence research model using the college of aeronautics whirling ann* (tech. rep.). Citeseer.

Nara, K., Tsubokura, M., & Ikeda, J. (2014). A numerical analysis of unsteady aerodynamics of formula car during dynamic cornering motion. *32nd AIAA applied aerodynamics conference*, 3138.

NASA. (2024a). *Aerodynamic coefficients* [Accessed: 2024-12-30]. https://www.grc.nasa.gov/www/k-12/VirtualAero/BottleRocket/airplane/ac.html

NASA. (2024b). *Langley history* [Accessed: 2024-12-30]. https://www.nasa.gov/langley/history/

NASA. (2025). *Menter shear stress transport (sst) turbulence model* [Last updated October 04, 2024; accessed April 10, 2025]. http://turbmodels.larc.nasa.gov/sst.html

Nedić, J., Ganapathisubramani, B., & Vassilicos, J. C. (2013). Drag and near wake characteristics of flat plates normal to the flow with fractal edge geometries. *Fluid Dynamics Research*, *45*(6), 061406.

Newman, J. N. (2018). *Marine hydrodynamics*. The MIT press.

Noble, J. (2023). *Why ferrari can run the front wing design that mercedes could not* [Accessed: 2024-12-30]. https://www.autosport.com/f1/news/why-ferrari-can-run-the-front-wing-design-that-mercedes-could-not/10432027/

Pathanadka, C. (2022). *Translationally accelerating wings in ground effect: A numerical study* [Master's thesis, Delft University of Technology] [Accessed: 2024-12-27]. http://resolver.tudelft.nl/uuid:76b2fb99-0cf9-4fa2-8a1a-441326193fb9

Pattinson, J., Lowenberg, M. H., & Goman, M. (2013). Multi-degree-of-freedom wind-tunnel maneuver rig for dynamic simulation and aerodynamic model identification. *Journal of Aircraft*, *50*(2), 551–566.

Reijtenbagh, J., Tummers, M., & Westerweel, J. (2023). Drag force on a starting plate scales with the square root of acceleration. *Physical review letters*, *130*(17), 174001.

Reijtenbagh, J., Tummers, M. J., & Westerweel, J. (2022). Investigation on the drag force and flow field of an accelerating plate. *12th International Symposium on Turbulence and Shear Flow Phenomena, TSFP 2022*.

Severholt, J. (2017). Generic 6-dof added mass formulation for arbitrary underwater vehicles based on existing semi-empirical methods.

Shaalan, A., Assanis, D., Raman, A., Wijeyakulasuriya, S., & Senecal, K. (2024). *Formula 1 race car aerodynamics: Understanding floor flow structures and why it is a key component in modern racing* (tech. rep.). SAE Technical Paper.

SimScale. (2023). *Compressible flow vs incompressible flow* [Accessed: 2025-06-09]. https://www.simscale.com/docs/simwiki/cfd-computational-fluid-dynamics/compressible-flow-vs-incompressible-flow/

Smedley, R. (2019). *Testing explained: Rob smedley on correlation and why it's so important* [Accessed: 2024-12-30]. https://www.formula1.com/en/latest/article/smedley-what-is-correlation.3gcOwCLuQ7rxk4bNeBKf1p.html

Spoelstra, A., Sciacchitano, A., Scarano, F., & Mahalingesh, N. (2021). On-site drag analysis of drafting cyclists. *Journal of Wind Engineering and Industrial Aerodynamics*, *219*, 104797.

Terra, W., Spoelstra, A., & Sciacchitano, A. (2023). Aerodynamic benefits of drafting in speed skating: Estimates from in-field skater's wakes and wind tunnel measurements. *Journal of Wind Engineering and Industrial Aerodynamics*, *233*, 105329.

Toet, W. (2013). Aerodynamics and aerodynamic research in formula 1. *The Aeronautical Journal*, *117*(1187), 1–26.

TU Delft - Aerodynamics Group. (2024). *Sports aerodynamics research* [Accessed: 2024-12-30]. https://www.tudelft.nl/lr/organisatie/afdelingen/flow-physics-and-technology/aerodynamics/research/sports-aerodynamics

University of Central Florida. (2021). *Chapter 3: Potential flow theory* [Accessed: 2025-06-09]. https://pressbooks.online.ucf.edu/aerodynamicstext/chapter/chapter-3-potential-flow-theory/

Veena - Cadence. (2025). *From sketch to speedway: Mclaren formula 1 team's aerodynamics tale*. https://community.cadence.com/cadence_blogs_8/b/cfd/posts/from-sketch-to-speedway-mclaren-formula-1-team-s-aerodynamics-tale

Warwick, M. (2024). Is f1's cost cap leading to better racing? [Accessed: 2024-12-27]. *BBC Sport*. https://www.bbc.com/sport/formula1/articles/ckgn5rmeke4o

Watanabe, K., & Matsuno, K. (2009). Moving computational domain method and its application to flow around a high-speed car passing through a hairpin curve. *Journal of computational Science and Technology*, *3*(2), 449–459.

Wikipedia. (2025). *Chaparral 2f* [Online; accessed 5-February-2025, licensed under CC BY-SA 4.0]. https://en.wikipedia.org/wiki/Chaparral_2F

Zerihan, J., & Zhang, X. (2001a). A single element wing in ground effect-comparisons of experiments and computation. *39th Aerospace Sciences Meeting and Exhibit*, 423.

Zerihan, J., & Zhang, X. (2001b). A single element wing in ground effect-comparisons of experiments and computation. *39th Aerospace Sciences Meeting and Exhibit*, 423.

Zhou, S. (2023). *Lift coefficient of an accelerating wing with ground effect* [Master's thesis, Delft University of Technology] [Accessed: 2024-12-27]. http://resolver.tudelft.nl/uuid:b7301745-e503-4a76-83d9-aea7d2c19437